FY2011 YEAR END TECHNICAL REPORT
May 18, 2011 to May 17, 2012

Chemical Process Alternatives for Radioactive Waste

Submitted on June 18, 2012

Principal Investigators:

Leonel E. Lagos, Ph.D., PMP[®]

Dave Roelant, Ph.D.

Florida International University Collaborators:

Dwayne McDaniel, Ph.D., P.E.

Jose Varona, M.S.

Amer Awwad, M.S., P.E.

Seckin Gokaltun, Ph.D.

Romani Patel, M.S.

Tomas Pribanic, M.S.

Jario Crespo

DOE Fellows

FIU | **Applied Research Center**
FLORIDA INTERNATIONAL UNIVERSITY

Addendum:

This document represents one (1) of five (5) reports that comprise the Year End Reports for the period of May 18, 2011 to May 17, 2012 prepared by the Applied Research Center at Florida International University for the U.S. Department of Energy Office of Environmental Management under Cooperative Agreement No. DE-EM0000598.

The complete set of FIU's Year End Reports for this reporting period includes the following documents:

1. Chemical Process Alternatives for Radioactive Waste
   Document number: FIU-ARC-2012-800000393-04b-211

2. Rapid Deployment of Engineered Solutions for Environmental Problems at Hanford
   Document number: FIU-ARC-2012-800000438-04b-208

3. Remediation and Treatment Technology Development and Support
   Document number: FIU-ARC-2012-800000439-04b-210

4. Waste and D&D Engineering and Technology Development
   Document number: FIU-ARC-2012-800000440-04b-212

5. DOE-FIU Science & Technology Workforce Development Initiative
   Document number: FIU-ARC-2012-800000394-04b-059

Each document has been submitted to OSTI separately under the respective project title and document number as shown above.

TABLE OF CONTENTS

LIST OF FIGURES

LIST OF TABLES

PROJECT 1 OVERVIEW

The Department of Energy's (DOE's) Office of Environmental Management (EM) has a mission to clean up the contaminated soils, groundwater, buildings and wastes generated over the past 60 years by the R&D and production of nuclear weapons. The nation's nuclear weapons complex generated complex radioactive and chemical wastes. This project is focused on tasks to support the safe and effective storage, retrieval and treatment of high-level waste (HLW) from tanks at Hanford and Savannah River sites. The objective of this project is to provide the sites with modeling, pilot-scale studies on simulated wastes, technology assessment and testing, and technology development to support critical issues related to HLW retrieval and processing. Florida International University (FIU) engineers work directly with site engineers to plan, execute and analyze results of applied research and development.

During FY11 Project 1, titled "Chemical Process Alternatives for Radioactive Waste", focused on three tasks related to HLW research at FIU. These tasks are listed below and this report contains a detailed summary of the work accomplished for FY11.

Task 2 - Waste Slurry Transport Characterization: The objective of this task is to qualify (test & evaluate) pipeline unplugging technologies for deployment at the DOE sites. Additionally, FIU has worked closely with engineers from Hanford's Tank Farms and Waste Treatment and Immobilization Plant on developing alternative pipeline unplugging technologies. After extensive evaluation of available commercial unplugging technologies in the previous years, two novel approaches are being developed at FIU including a peristaltic crawler and an asynchronous pulsing method.

Task 12 - Multiple-Relaxation-Time Lattice Boltzmann Model for Multiphase Flows: The objective of this task is to develop stable computational models based on the multiple-relaxation-time lattice Boltzmann method. The computational modeling will assist site engineers with critical issues related to HLW retrieval and processing that involves the analysis of gas-fluid interactions in tank waste.

Task 15 - Evaluation of Advanced Instrumentation Needs for HLW Retrieval: This task will evaluate the maturity and effectiveness of commercial and emerging technologies capable of addressing several instrumentation needs for HLW feed mixing and retrieval. Promising candidate technologies will be evaluated for their functional and operational capabilities and the technologies that show sufficient feasibility for deployment will be subjected to additional tests to determine their effectiveness in the harsh chemical and nuclear radiation tank environments.

TASK 2 FY11 YEAR END TECHNICAL REPORT
Waste Slurry Transport Characterization

EXECUTIVE SUMMARY

In previous years, Florida International University (FIU) has tested and evaluated a number of commercially available pipeline unplugging technologies. Based on the lessons learned from the evaluation of the technologies, two alternative approaches have been developed by FIU. These are an asynchronous pulsing system (APS) and a peristaltic crawler. The APS is based on the principle of creating pressure waves in the pipeline filled with water from both ends of the blocked section in order to break the bonds of the blocking material with the pipe wall via forces created by the pressure waves. The waves are created asynchronously in order to shake the blockage as a result of the unsteady forces created by the waves. The peristaltic crawler is a pneumatically operated crawler that propels itself by a sequence of pressurization/depressurization of cavities (inner tubes). The changes in pressure result in the translation of the vessel by peristaltic movements.

For this performance period, experiments were conducted to validate the asynchronous pulsing system's ability to unplug a small-scale pipeline testbed and to compare the performance of the APS to the data obtained from a CFD model developed for the system.

The unplugging experiments consisted of placement of K-mag based plugs within a test pipeline loop and using the system to unplug the pipeline. The results obtained during the experimental phase of the project are presented which include pressures and vibration measurements that capture the propagation of the pulses generated by the system.

The pulse-loop response verification testing phase compared the performance of the APS to the data obtained from a CFD model developed for the system. The model predicts resulting pressure amplification as a response to a single step pulse input, with the amplification contingent on the pipeline length and geometry. These tests evaluated a single-cycle pulse amplification caused by various piston pump drive pressures, drive times, and drive profiles.

During this performance period, effort also focused on the design, assembly and testing of the third generation peristaltic crawler (TGPC). Design improvements were performed to overcome the limitations observed in the experimental testing of the second generation crawler that was performed in FY10. Improvements on the TGPC include the reduction of the crawler's outer diameter and the use of an edge-welded bellow in the body assembly. The crawler was manufactured, and tested to determine its navigational capability and pipeline unplugging effectiveness. Other improvements included the design and testing of a 500-ft multi-line tether assembly, design and procurement of a tether-reel system and evaluation of an on-board control valve system.

The experimental testing of the TGPC consisted on two speed tests, one using a 15-foot tether and the other using a 500-ft tether. The speed test for the crawler unit showed a maximum speed of 21 ft/hour for the 15-foot tether and 1 ft/hour for the 500-foot tether. The maneuverability test indicated that the crawler is able to navigate through a 90° elbow in a time lapse of 11 minutes and 23 seconds. The maximum pulling force achieved by the crawler was 133 lbs of force when

providing 60 psi of pressure to the bellow assembly. Two high pressure water nozzles were used to test the crawler's unplugging ability: 1) a rotating nozzle and 2) a 15° nozzle. Results showed that the rotating nozzle provided was the most successful on K-mag based plugs.

INTRODUCTION

Pumping high-level waste (HLW) between storage tanks or treatment facilities is a common practice performed at Department of Energy (DOE) sites. Changes in the chemical and/or physical properties of the HLW slurry during the transfer process may lead to the formation of blockages inside the pipelines. Current commercially available pipeline unplugging technologies do not provide results that are cost-effective and reliable. As part of the research objectives at FIU, novel pipeline unplugging technologies that have the potential to efficiently remediate cross-site and transfer line plugging incidents are being developed. These are an asynchronous pulsing system (APS) and a peristaltic crawler. Both technologies been developed over the past few performance periods and details of the operational principles and history of the project can be obtained in Reference [1]. This report presents details of the devices and procedures used for the experimental testing of the two technologies for FY11. The first section pertains to the experimental testing of the APS followed by the experimental testing of the peristaltic crawler.

Initially, a brief background on the principles on which the APS technology is based is provided. Previous studies have demonstrated on a lab scale testbed how operational process parameters can be optimized [1]. During FY11, additional parameterization was conducted as well as testing on plugged lines. An engineering scale testbed was subsequently designed with modifications that provided a more realistic test bed. The next phase of testing also included using a computational fluid dynamics (CFD) code to simulate the pulses and pipeline response. Once validated, the code can be used to extrapolate the responses to significantly longer pipelines. It will also aid in determining the effects various pipeline configurations and effects of air entrained in the system.

In addition, this report presents the improvements implemented in the TGPC. These Improvements are based on shortfalls observed in the previous performance period that include changes in the design of the crawler unit and the implementation of a tether-reel assembly. Experimental testing of the TGPC encompasses testing its navigational performance and unplugging capabilities. Conclusions derived from the experimental testing are presented and recommendations for further improvements are provided.

Finally, preliminary conclusions from the results obtained for each technology are presented. Based on the results and conclusions, recommendations of the path forward are provided.

EXPERIMENTAL TESTING OF THE ASYNCHRONOCUS PULSING SYSTEM

Background

In order to clear plugged radioactive waste transfer lines, non-invasive techniques can have significant advantages since problems such as contamination clean-up and exposure to radioactive waste of invasive devices can be avoided. During previous work, FIU evaluated two technologies that fall into this category, namely, NuVision's wave erosion method and AIMM Technologies' Hydrokinetics method. These technologies fill the plugged pipeline with water up to an operating pressure level and induce a pressure variation at the inlet of the pipeline to dislodge the plug. Using the experience obtained during experimental evaluations of both technologies, FIU has developed a non-invasive unplugging technology called the Asynchronous Pulsing System (APS) that combines the attributes of previously tested technologies. A pipeline unplugging technology using similar principles for generating pressure pulses in pipelines has previously been tested at the Idaho National Laboratory (INL) by Zollinger and Carney [2]. The most relevant difference of the current technology from the unplugging method developed at INL is that both sides of the pipeline are used to create the asynchronous pulsing in the current technology. Figure 1 shows a sketch of how this technology can be utilized for a typical plugging scenario. During last year's work, the pulse generation unit for the APS was optimized to maximize the effect of the pressure differential at the plug faces. Part of this year's work concentrated on applying the information obtained from last year's work to validate the asynchronous pulsing system's ability to unplug a pipeline on a small-scale testbed. The experiments consisted of placement of potassium 2-foot potassium magnesium sulfate (K-mag) based plugs within a test pipeline loop and using the system to unplug the pipeline.

Figure 1. Pipeline unplugging scenario in a horizontal pipe.

The APS is based on the idea of creating pressure waves in the pipeline filled with water from both ends of the blocked section in order to dislodge the blocking material via forces created by the pressure waves. The waves are generated asynchronously in order to break the mechanical bonds between the blockage and the pipe walls as a result of the vibration caused by the unsteady forces created by the waves.

General Description

The asynchronous pulsing system uses a hydraulic pulse generator to create pressure disturbance that dislodge blockages within the pipeline. The test pipeline loop contains two identical pipeline sections with a plug between them (See Figure 2). This test loop allows for control of the individual pipeline section pulse characteristics to determine how each pulse influences the total plug dynamic loading. The experimental test loop was assembled using four straight sections and two 90° elbows. The pipes used for the loop are 3-inch diameter schedule-10 carbon-steel pipes. Each side of the symmetric loop has a 9-foot and an 8-foot pipe with an elbow between them. A blockage was placed at the center of the loop to emulate a plug in the pipeline. The heart of the asynchronous pulsing system are two hydraulic piston pumps that are powered by the

pulse generation unit which is comprised of hydraulic power unit and two electronically controlled high-speed valves. The pipeline is instrumented with accelerometers, pressure transducers and thermocouples located at strategic locations to capture the changes of the induced disturbances inside the pipeline.
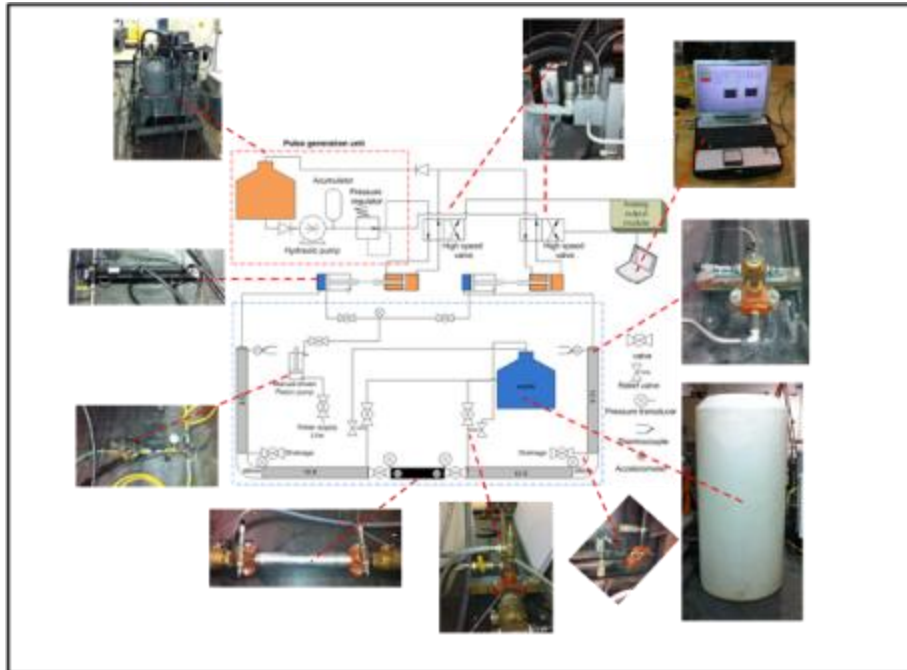
Figure 2. Experimental set-up used for validating APS.

RESULTS - ASYNCHRONOCUS PULSING SYSTEM

Hydraulic pressurization tests

The prior year's evaluation of commercially available methods involved the use of clay and salt based plugs. During these tests, it was observed that clay-based plugs were often removed as a result of the internal plug stresses, as opposed to a reduction in the plug/wall interaction forces. This type of removal typically resulted in a thin layer of material remaining on the pipe wall, which indicated that the plug failed [internally] in shear near the wall. For the APS experiments, the plugs were pressurized from both sides, essentially compressing the plug and increasing the friction created between the plug and pipe wall. This compression also increased the plug extrusion pressure, making it more difficult to remove. The higher pressure, however, provided an avenue to create larger pressure differences that varied on both sides of the plug. The pressure variations affected the pipe wall/plug interaction forces on both sides of the plug, simultaneously. To provide a better understanding of the strength of the plugs being tested, hydraulic pressurization tests were conducted on three randomly selected plug samples. These tests also ensured that the plugs would not fail by simply applying low static pressures and to verify the plugs were manufactured consistently. Each of the three plugs tested failed at approximately 300 psi, above the maximum pressures applied. A photo of one of the hydraulic tests is shown in Figure 3 below. Note that although the plugs were not completely removed, they were considered unplugged if flow was passed through the blockage.

Figure 3. Hydraulic pressurization tests.

Asynchronous pulsing unplugging trials

Prior to initiating the asynchronous pulsing unplugging trials, several parametric tests were conducted on the system to determine the system's response to various input parameters. A solid aluminum cylinder was placed within the pipeline to emulate a plug and the system was run under various pipeline static pressures, oil hydraulic pressure and pulse frequencies. After analyzing the data from the parametric tests, a test matrix was developed for the unplugging trials. However, it was determined that under certain conditions, the system was capable of generating pressures that exceeded a preset limit of 300 psi in the pipeline. Additionally, the plugs also altered the response of the system, requiring further changes to the original test matrix.

Asynchronous pulsing unplugging trials were conducted using K-mag plugs with pulse frequencies of 1, 2 and 4 Hz and static pressures within the pipeline of 60 and 200 psi. These experiments were done with the pipeline 100% filled with water and then repeated with the pipeline filled with 87.5% with water. The pipeline was considered unplugged when the pressures equalized on both sides of the plug. The general unplugging procedure for using the asynchronous pulsing system is as follows:

1.   Flush the liquid in the pipes and evacuate the air using a vacuum pump on both sides of the blockage, if possible.

2.   Fill the pipeline from both ends with water, to a specified pressure.

3.   Start asynchronous pulsing by creating positive pressure waves at both ends of the pipeline by adjusting the frequency and phase shift between two pulse generators.

60 psi trials

Typical pressures at each plug faces using a static pressure of 60 psi and a pulse frequency of 1 Hz are shown in Figure 4. The maximum pressure differential was approximately 160 psi on the plug. During this trial, the system was run for over 20 minutes and was unable to unplug the pipeline.
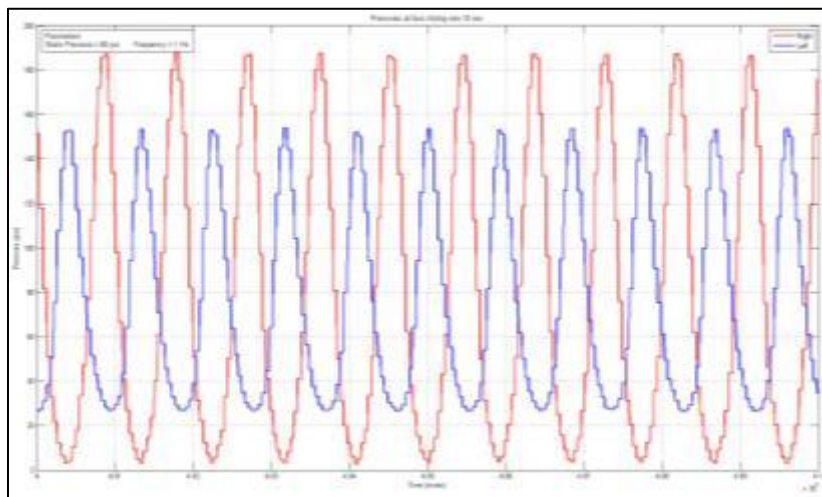
Figure 4. Pressure Pulse profile with 60 psi static pressure and a frequency of 1 Hz.

Figure 5 below shows the results from a trial at a static pressure of 60 psi and a pulse frequency of 2 Hz. During this test the system was unplugged in less than 7 minutes. Figure 6 shows an extended time history of the pressure profiles and the point at which flow broke through the plug. It is interesting to note that the differential pressure was approximately 120 psi. This differential is less than the 1Hz test, suggesting that resonation may have played a role in the unplugging. This was the only pressure-frequency combination in which the pipeline was unplugged. This experiment was repeated two more times with similar results.
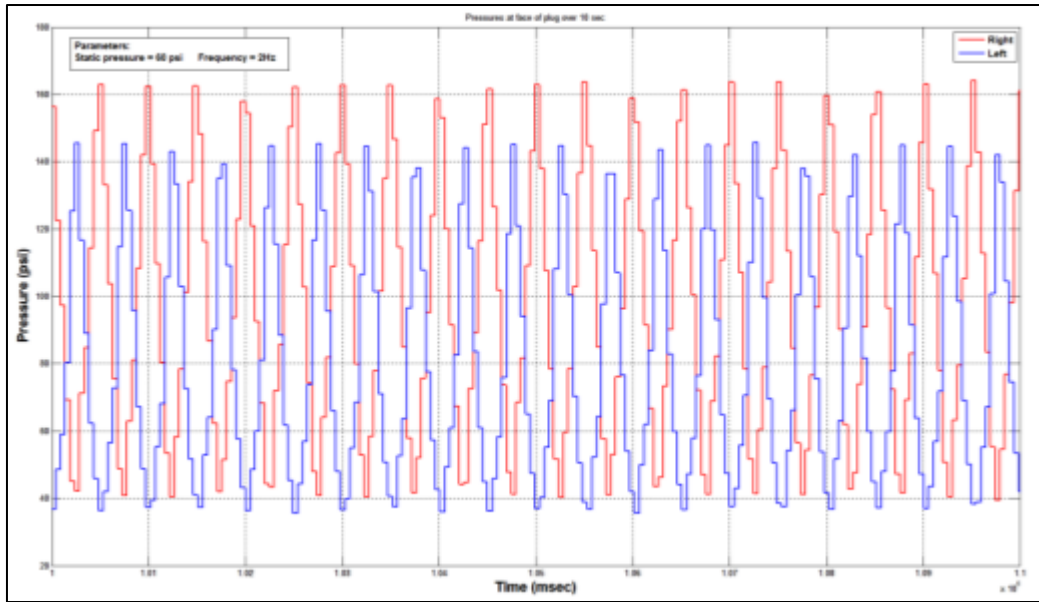
Figure 5. Pressure pulse profile with a 60 psi static pressure and a frequency of 2Hz.
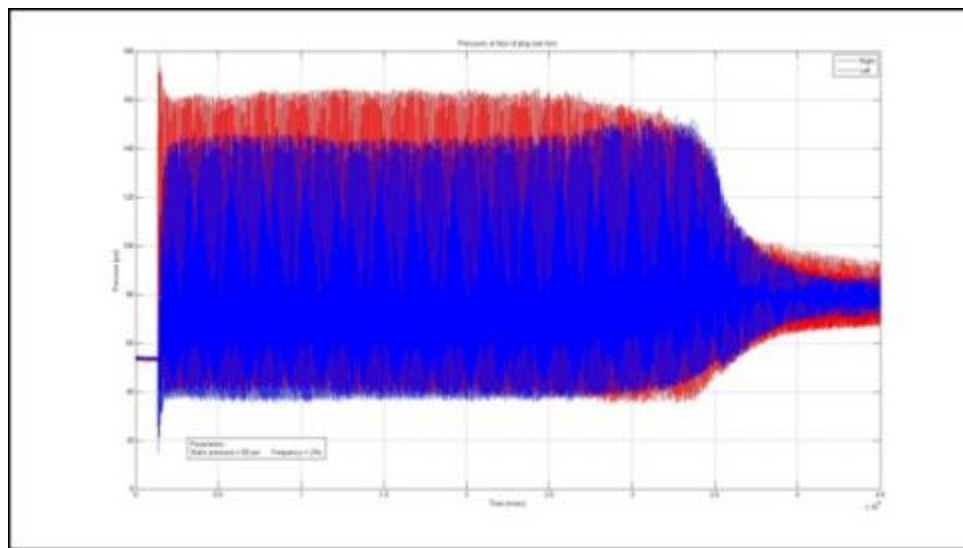
Figure 6. Extended time history of plug face pressures showing unplugging event.

200 psi trials

Figure 7 shows an extended time history of the pressure profiles from a trial using a static pressure of 200 psi and a pulse frequency of 2 Hz. The red shows the pressure envelope on one face of the plug and the blue shows the pressure envelope on the other side. The magnitude difference is likely due to the variation in the water absorbed at each of the plug faces. During this trial the system was run for over 16 minutes and was unable to unplug the pipeline. As can be seen from the figure, the static pressure dropped from the initial value of 200 psi to approximately 140 psi before the system was started. This pressure drop was likely due to the plug absorbing the water. This phenomenon was observed in all trials but was most prevalent in the high static pressure tests. Another issue observed during the trial was the drifting of the

pressures. This is believed to be due to the combination of both water loss due to absorption into the plug and the drifting of the water pump's pistons. Since the piston's position is controlled by hydraulic oil pressure, under high static pressures, the piston will drift as a result of the inherent lag in the oil pressure control valve.
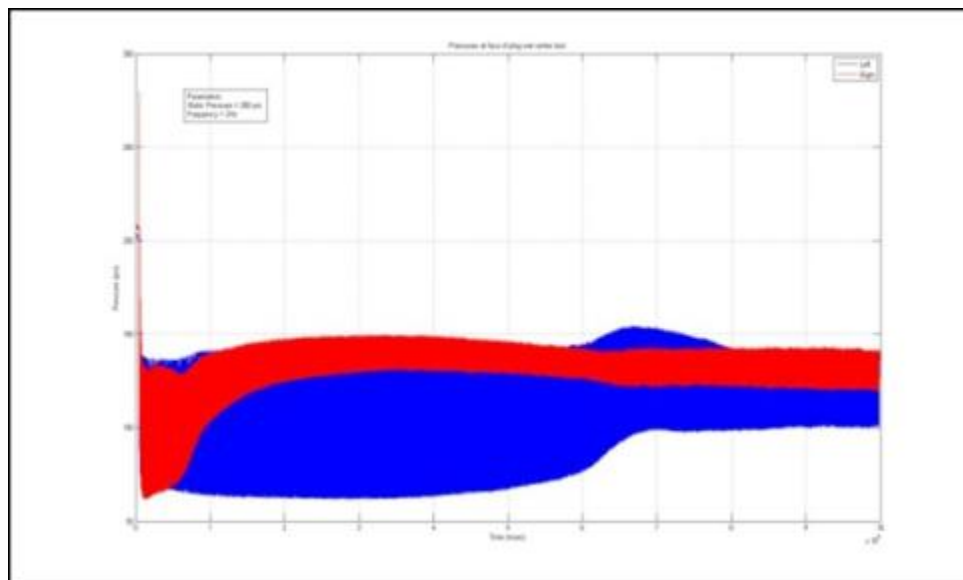
Figure 7. Pressure pulse profile with a 200 psi static pressure and a frequency of 2Hz.

Results from the trial with a static pressure of 200 psi and a pulse frequency of 4 Hz yielded similar results. During this test, the system was run for over 8 minutes and was unable to unplug the pipeline. As in the previous trial, the static pressure dropped before the system was started. Drifting of the face pressures was also observed.

87.5% filled pipeline trials

In the trials with 87.5% water in the pipeline, the pipeline was filled with water and all the air was purged out. The pressure in the fully flooded line was then vented to equalize the pressure to atmospheric pressure. 12.5% of the calculated volume of the pipeline was then pumped out using a peristaltic pump with a vent open which allows air to replace the water that was being removed. All the vents were closed and the pipeline was pressurized to the desired static pressure by adding additional water. No other modifications were done to the system.

Figure 8 shows a typical pressure profile at the two plug faces for a 2 Hz test with the pipeline filled with 87.5% of water. As can be seen in the figure, the pump could only generate a pressure rise of less than 10 psi. This was due to a low water to pipeline-volume ratio and a piston pump system. Additionally, significant piston drift was observed.
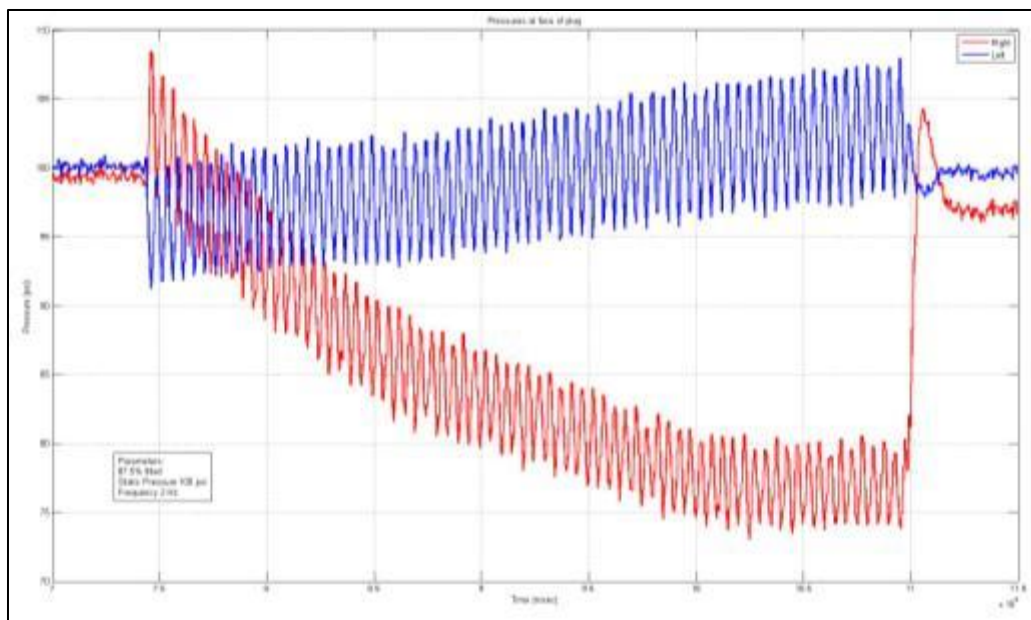
Figure 8. Pressure pulse profile with a 100 psi static pressure and a frequency of 2 Hz.

Similar results were obtained for the 4 Hz test with the pipeline filled with 87.5% of water. The pump was able to generate a 35 psi increase on the left side which was a greater pressure rise than the 2 Hz test. However there was a significant amount of piston drift as well. None of the trials for the pipeline filled with 87.5% water resulted in an unplugging.

Pulse-Loop Response Verification Phase

During the unplugging phase of experiments, excessive deflection was observed in the pipeline loop. This is believed to be due to the type of connectors used to connect the various components of the pipeline. Therefore, the pipeline loop was redesigned using 3" SCH-40 threaded pipes. Threaded pipe was utilized to minimize pipeline deflection that would affect the pressure pulse propagation. An additional focus of this phase is to be able to predict the system performance at various lengths and configurations. Thus, a computational fluid dynamics model derived from the method of characteristics was utilized to simulate pressure variation in the pipeline. During this phase, only one side of a pipeline is utilized for validation of the model and experimental testing.

The model predicts resulting pressure amplification/degradation response to a single step pulse input for a given pipeline length and geometry. These tests evaluated a single-cycle pulse caused by various piston pump drive pressures, drive times, and drive profiles. Initial testing was conducted using a fully flooded system.

A single piston water pump attached to one end of the pipeline was used to create the pressure waves in the system. Six pressure transducers located throughout the pipeline measured the pressure pulse as it propagates through the pipeline. Figure 9 shows a schematic of the initial and shortest test loop (96 ft). Longer pipeline lengths will be utilized in the future to assist in model verification and extrapolation of results. Figure 10 shows the input (P1) pressure profile for an experimental test and corresponding simulation. Figure 11 shows the experimental and simulated pressures at the end of the pipeline (P6) as a result of a 500 millisecond pulse. Both the experimental and the simulated results are in agreement and show that there is a 10 psi pressure

amplification between the inlet and the end of the pipeline with an 8 millisecond pulse travel time. The amplification is a result of the energy transfer to the plug face from the kinetic energy of the column of water imposed by the pressure pulse. Pressure oscillation predicted in the simulation at the end of the pipeline is a result from fluid transients and is not detected by the transducers in the experimental tests. This is likely due to the response time of the pressure transducers.
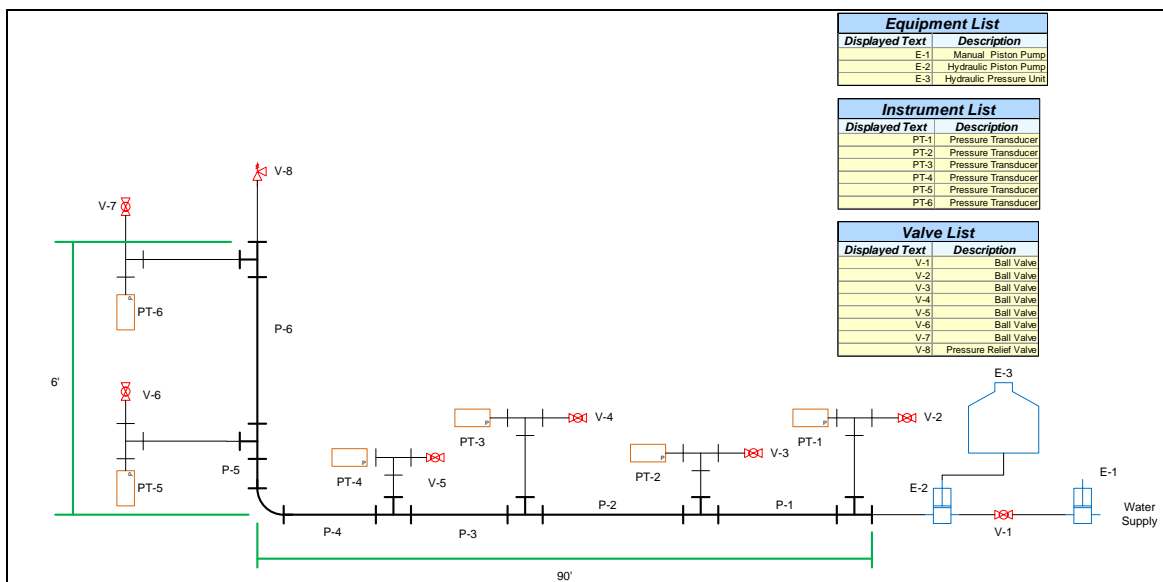
Figure 9. Intial pulse response loop (not to scale).
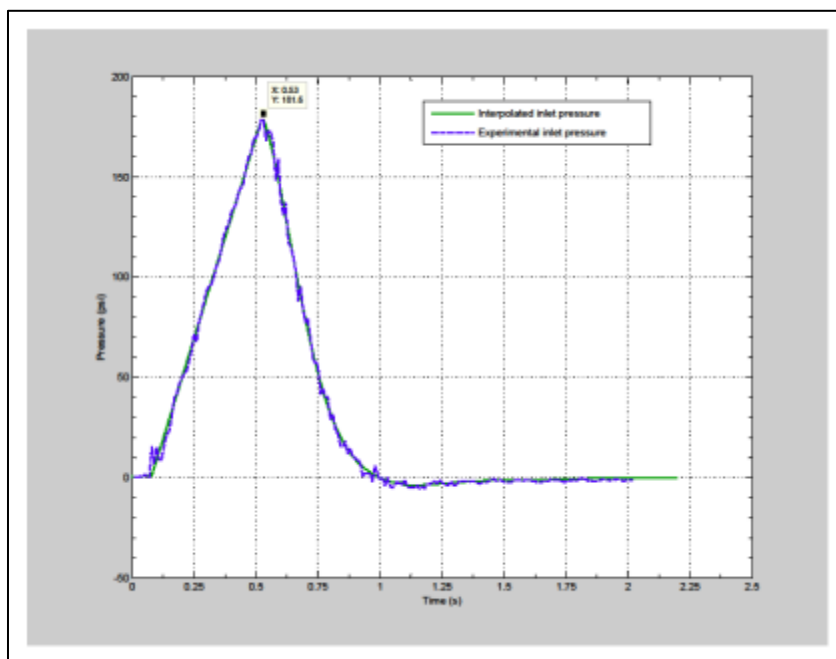
Figure 10. Experimental and simulated inlet pressure for a 500 millisecond pulse.
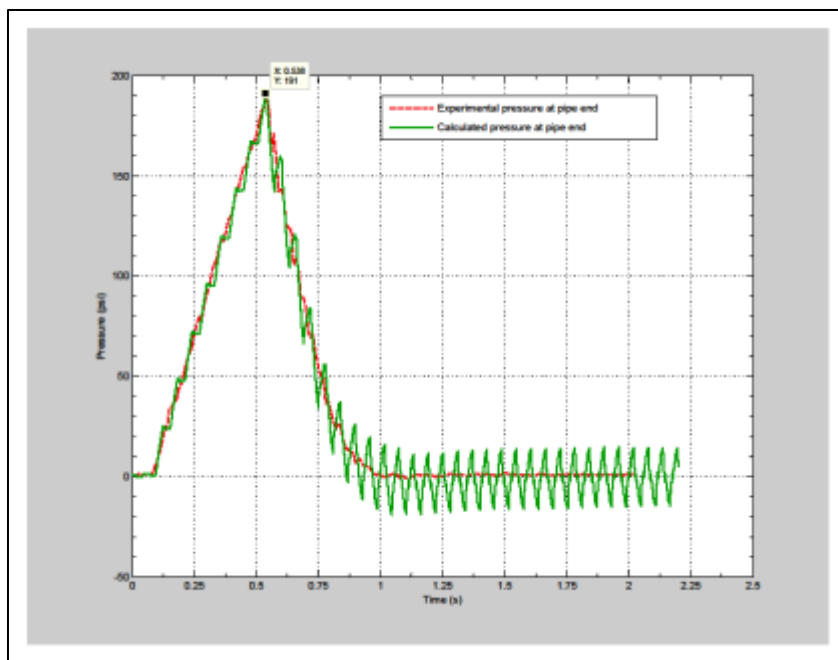
Figure 11. Experimental and simulated pipe end pressure results for a 500 millisecond pulse.

Discussion

After analyzing the data of all the unplugging test runs, several observations were made. The first is that some of the results from the initial parametric tests conducted on the aluminum plug were unable to be repeated in trials with the K-mag plugs. This was likely due to the reduction of the water volume in the system from the plug absorbing the water as well as the dissolution of the plug which resulted in a reduction of the water to pipeline-volume ratio. A second observation from the 87.5% water tests was that a piston type pump system with a fixed water volume is very sensitive to the water to pipeline-volume ratio. This is because the piston pumps have a fixed discharge volume per stroke and are limited to the pressure they can produce with replenishment of any lost water. In future work, different pump designs will be considered that are less affected by the water to pipeline-volume ratio. Finally, for the fully flooded system, the lower static pressures and a frequency of 2 Hz were optimal operational parameters for the system. This suggests that the removal of the plug is dependent on the resonation of the system.

After analyzing the data from the initial pulse loop response verification phase, the CFD model results show close agreement with the experimental results for a fully flooded pipeline system. As expected, both sets of data show a pulse pressure amplification at the end of the pipeline.

DESIGN AND EXPERIMENTAL TESTING OF THE THIRD GENERATION PERISTALTIC CRAWLER

Background

For this performance period, FIU performed the design, assembly and experimental testing of the TGPC. Design improvements were performed to overcome the limitations observed in the second generation crawler. They include the reduction of the crawler's outer diameter and the use of an edge-welded bellow in the body assembly. The crawler was manufactured, and tested to determine its navigational capability and pipeline unplugging effectiveness. Other improvements included the design and testing of a 500 ft multi-line tether assembly, design and procurement of a tether-reel system and evaluation of an on-board control valve system.

As presented in the previous performance period, the peristaltic crawler is a pneumatically powered crawler that propels itself by a sequence of pressurization/depressurization of cavities. The changes in pressure result in the translation of the vessel by peristaltic movements. The unit consists of a flexible skeleton which allows it to turn around elbows. The advantage of using a device that can successfully navigate inside pipelines is the ability to bring unplugging technologies closer to the blockage. Figure 12 shows a side view of the TGPC unit. More information regarding the crawler's principles of motion and unplugging capabilities can be found in FIU's FY10 Year End Technical Report [1].
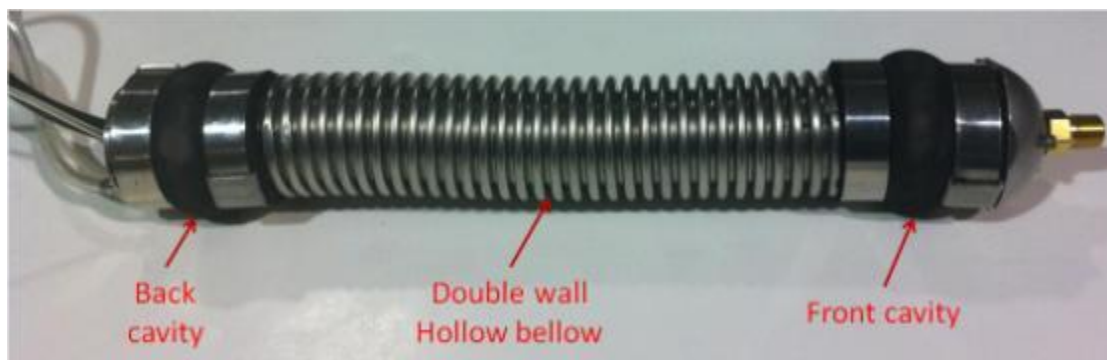
Figure 12. Side view of the peristaltic crawler.

Previous Versions of the Peristaltic Crawler

First Generation Peristaltic Crawler

The first generation peristaltic crawler was designed, assembled, and tested to provide experimental data to support the principles of motions described during the proof-of-concept phase of the project. The unit consisted of two concentric wire-reinforced rubber bellows attached to aluminum cylindrical rims. One rubber sleeve slides over each of the rims to define the front and back cavity. All the parts are held together by metal clamps. Figure 13 shows a side view of the first generation peristaltic crawler.

Figure 13. Side view of first generation crawler.

Results from the first generation PC experimental phase, proved that he crawler could navigate through a 90° elbow. The maximum pulling force achieved by the prototype was 27.3 lb by providing the system with 30 psi of air. The unplugging ability of the first generation crawler was evaluated by assembling a testbed containing a 3-foot bentonite clay plug. Unplugging tests demonstrated the crawler's high potential to unplug HLW pipelines.

Second Generation Peristaltic Crawler

Applying the lessons learned from the first generation peristaltic crawler, an improved design was created and a new unit was assembled and tested. The improvements were focused on three primary objectives: 1) increase the maximum allowable pressure inside the bellow, 2) increase the durability of the unit and 3) automate the motion controls of the crawler.

The maximum allowable pressure of the bellow assembly was increased by replacing the rubber bellows with stainless steel hydroformed bellows. The bellow assembly was welded together to make the unit more durable. It was found that the hydroformed bellow assembly can withstand a maximum pressure of 150 psi. Other design improvements included a rim design that prevented the flexible cavities from coming loose at the front and back cavities and the automation of the sequence of inflation/deflation of the cavities. Figure 14 shows a side view of the second generation crawler.

Figure 14. Second generation crawler.

The automation of the sequence of inflation/deflation of the cavities and bellow assembly was achieved by connecting the pneumatic valves to a programmable logic controller OMRON ZEN-10C1AR-A-V2. By programming an appropriate sequence and timing of the opening and closing of the valves, the desired motion was achieved. Figure 15A) shows a screen shot of the software

during forward motion. The programmable controller is incased in an air-tight fiberglass box that provides control of the unit by the use of switches and a joystick. As shown in Figure 15B), the control station contains the regulator, electronics, and pneumatic controls that direct the pressure or vacuum of air into the unit.
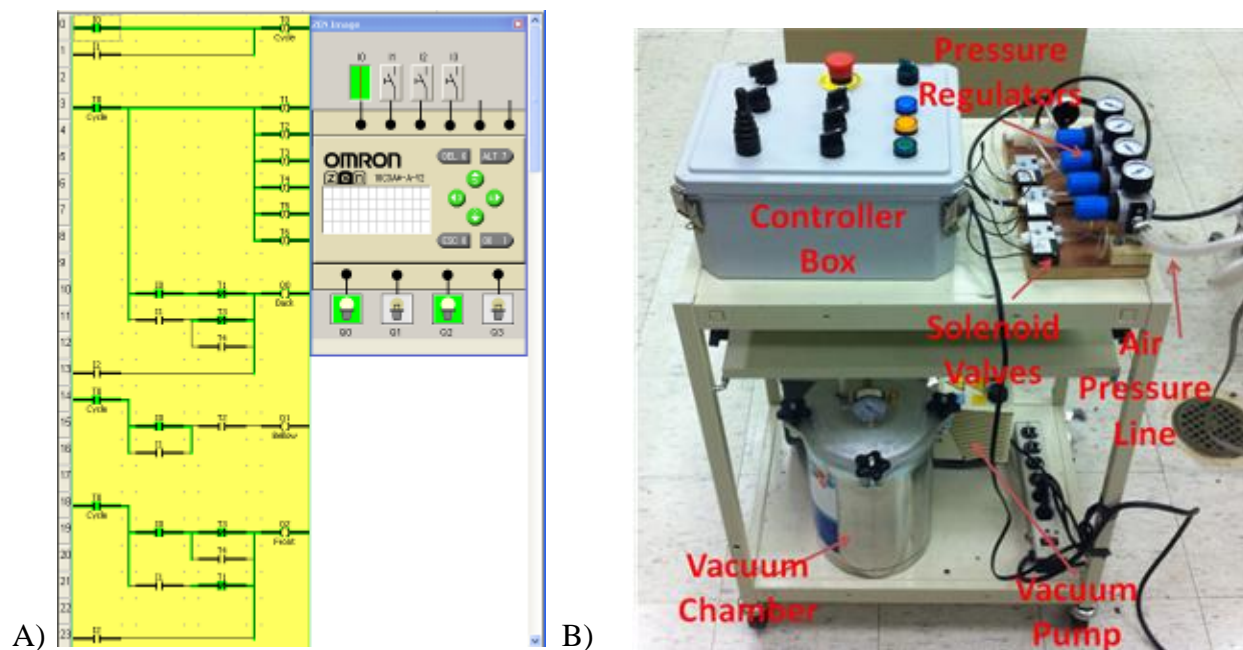
Figure 15. A) Screenshot of OMRON software, B) contol unit and pneumatic system to control SGPC.

Result obtained during the experimental testing of the second generation peristaltic crawler included:

- The optimal cycle time for pressurization/depressurization was 16 seconds.

- The maximum speed of the crawler in straight pipe was 0.5 ft/min.

- It was found that the crawler could not navigate through a Victaulic elbow (4.25 inches in radius) but was able to turn through a PVC elbow having a radius of 5.56 inches.

- The maximum pulling force recorded was 110 pounds at 90 psi of pressure inside the bellow assembly.

- The crawler successfully performed an unplugging operation of a 3-ft bentonite plug and on also on a 4.5 inch sodium aluminum silicate plug.

Design improvements for the Third Generation Peristaltic Crawler

Improvement of the bellow assembly

As mentioned previously, one the improvements of the TGPC was the reduction of the outside diameter. The reduction in the outside diameter allows the crawler to navigate through tighter elbows. The challenge from reducing the outside diameter of the bellow assembly was overcoming the resulting increase in stiffness of the assembly. High assembly stiffness reduces the crawler speed due to higher pressurization/depressurization requirements for each cycle. The outer bellow used on the second generation peristaltic crawler had a spring rate of 1.9 lb/in and

an outside diameter of 2.75 inches. The TGPC requirement to navigate through a 90° elbow is to have an outside diameter of 2.25 inches or less. A solution to the increase in stiffness due to the reduction in diameter was found by 1) replacing the inner hydroformed bellow with an edge welded below and 2) performing a finite element analysis of the bellow assembly to determine force/displacement parameters.

There are two types of commercially available stainless steel bellows which are edge welded bellows and hydroformed bellows. An edge welded bellow is assembled by welding thin stainless steel leafs to created each convolution. This process requires a welding process that is expensive and requires custom made molds and fixtures. Figure 16A) shows a general view of an edge welded bellow and Figure 16B) shows a cross section detail view of the welded leafs for an edge welded bellow. Hydroformed bellows are manufactured by welding a stainless steel thin plate to create a hollow cylinder that is then deformed plastically using an internal mandrill and an external cavity. These deformations define the convolutions of the bellow. Figure 16C) shows a typical hydroformed bellow.

Each of the manufacturing techniques produces a stainless steel bellow with different mechanical properties. The edge welded bellow provides superior flexibility and an expansion/contraction ratio but it does not allow for internal pressurization. The hydroformed bellow has a spring ratio which increases exponentially with a decrease in the bellow diameter, making it harder for it to turn in a 90° elbow but can be internally pressurized to relative high pressures. The bellow assembly configuration chosen for the TGPC is to have an outer hydroformed bellow and an edge-welded inner bellow.

A)   B)   C)
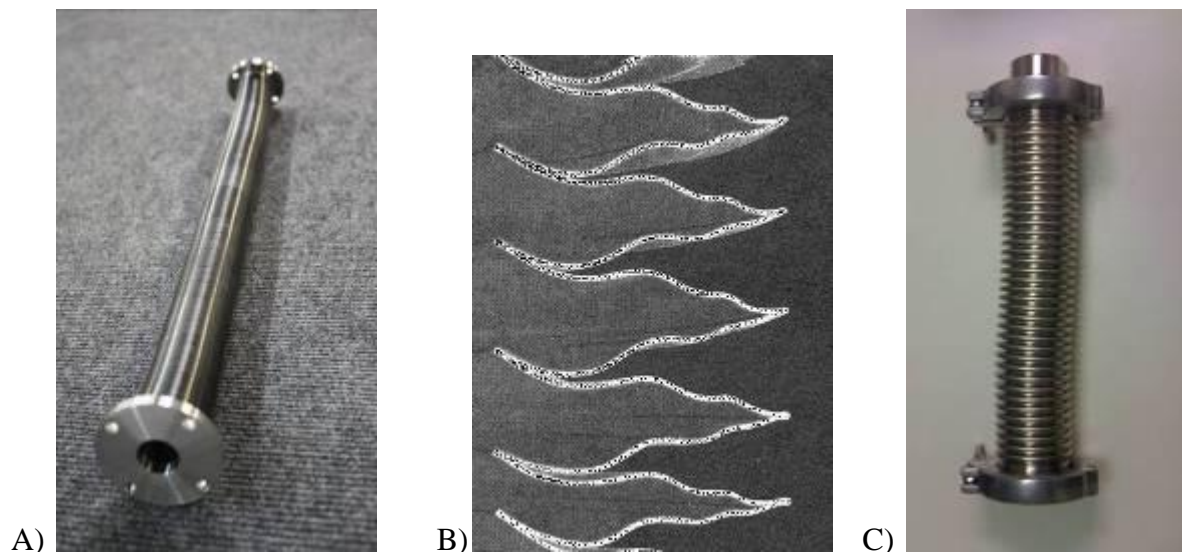
Figure 16. A) Edge welded bellow, B) detail cross section of edge welded below, C) hydroformed bellow.

To make an accurate projection of the stiffness of a hydrofomed bellow with an outside diameter of 2.25 inches, a finite element analysis (FEA) coupled with experimental validations was conducted. To first validate the analysis procedure, an FEA of the outer bellow used on the second generation crawler was performed. The analysis, conducted using ABAQUS, was carried out utilizing the build-in solver and was modeled as a static case. The bellow was modeled using shell elements and meshed using 4-node quad elements. Figure 17A) shows the outer bellow model and mesh and Figure 17B) shows the convergence data of the element size used during the meshing procedure.

Mesh Size	No. of Elements	Displacement (inches)
0.250	12050.000	0.692
0.200	14836.000	0.644
0.150	20605.000	0.654
0.125	26055.000	0.659
0.120	27128.000	0.660
0.115	28611.000	0.659
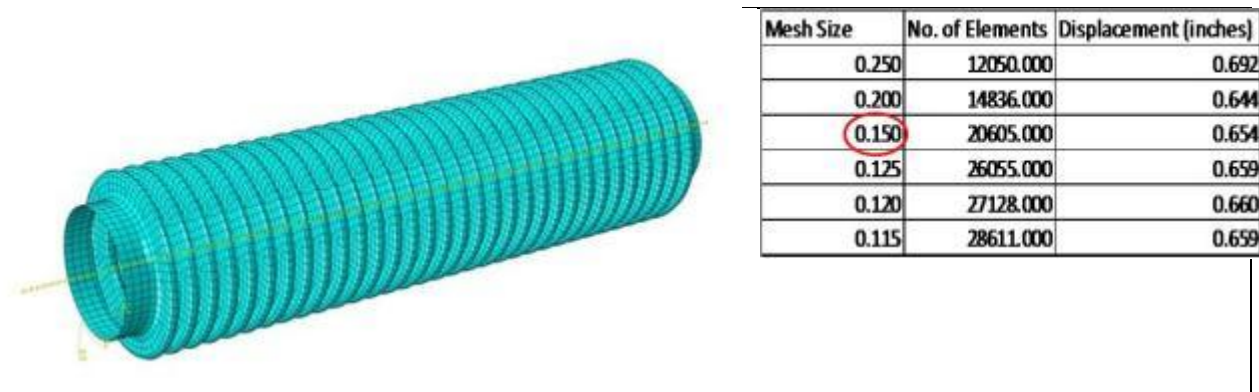
Figure 17. A) Mesh of hydroformed bellow, B) Mesh optimization data.

Following the meshing procedure, the model of the bellow was loaded to 10, 20, and 30 lb in the axial direction. The displacement for each case was recorded. Figure 18 shows the FEA of the hydroformed bellow loaded axially with a compressive force of 30 lbs and 1.979 inches of maximum displacement.
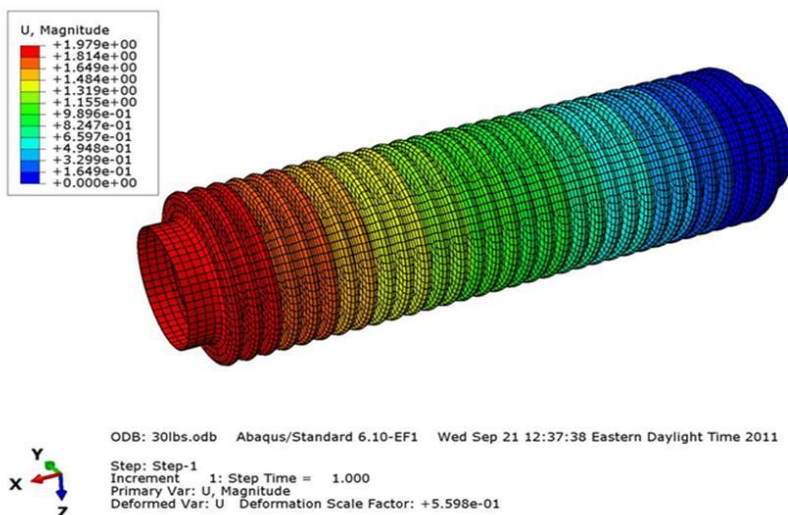
Figure 18. FEA model of hydroformed bellow loaded with 30lb of axial force.

Experimental tests were then conducted to validate that the procedure used for modeling the bellow yielded accurate results. A small fixture was fabricated and the bellow was axially loaded in compression using a spring scale. Figure 19 shows the test set-up used to measure the bellow axial displacement at different loads.
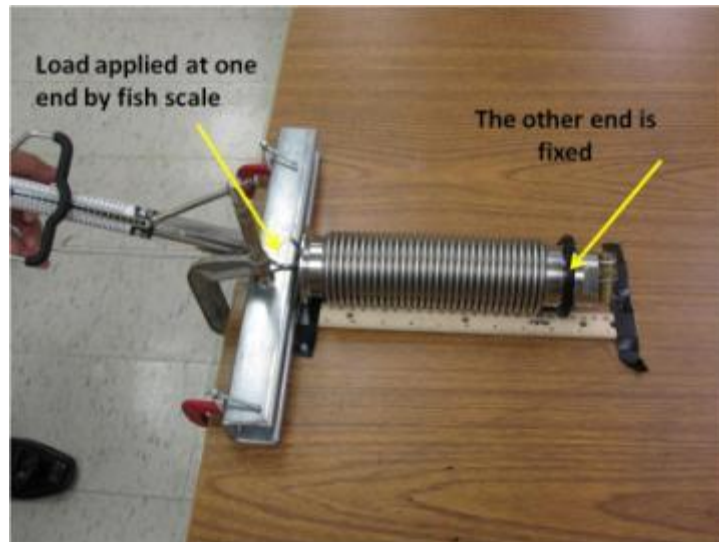
Figure 19. Test set-up used to measure the bellow axial displacement.

Once the results for the axial deformation were validated, a similar procedure was conducted to determine the deformation of the bellow due to bending. Figure 20A) shows the FEA of the bellow loaded in bending to 90° and Figure 20B) shows the experimental set-up used to validate the FEA data.
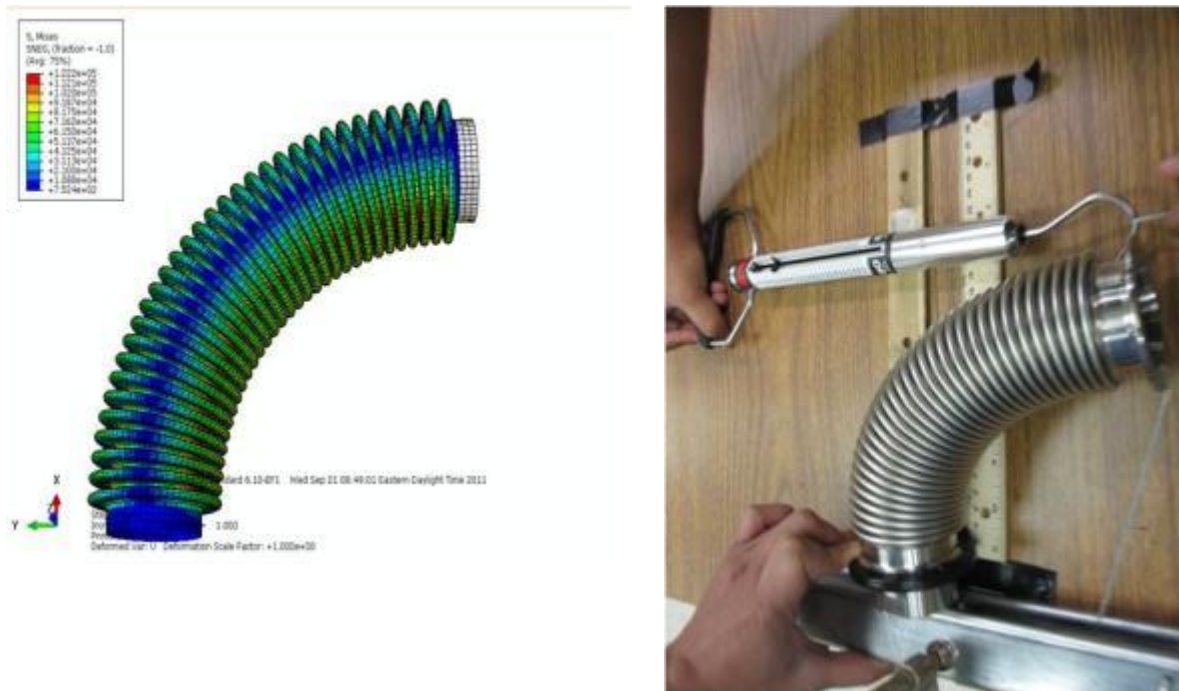
Figure 20. A) FEA model of the bellow bent to 90°, B) experimental set-up for validation of results.

Comparison of the experimental data with the FEA results for the 90° bend analysis demonstrated that the two data sets were in good agreement (Figure 21).
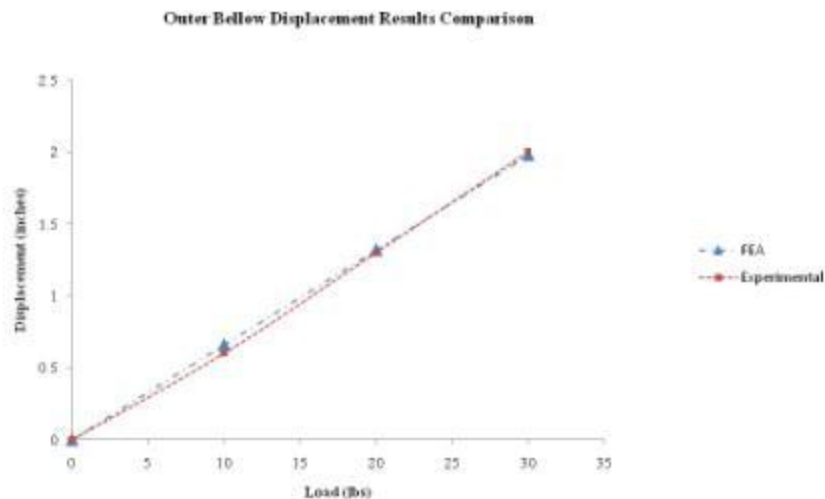
Figure 21. Comparison of FEA data to experimental results.

Next, an FEA model of a hydroformed bellow having an outside diameter of 2.25 inches was generated. The FEA yielded an axial deformation of 1.132 inches when loaded with 30 lbs of compressive force (37% increase in stiffness when compared to the 2.75 in outside diameter bellow). It was determined that the increase in stiffness was within acceptable range.

Design and manufacturing of the crawler unit design

Using the information from the FEA, the design of the unit was conducted in Solidworks. The overall design consisted of one outer hydroformed bellow, one edge-welded bellow, and two rims. The primary design requirement was to create a durable unit with a maximum outside diameter of 2 inches. Figure 22 shows the CAD design of crawler unit.

Figure 22. 3-D design of the crawler unit.

Parts were then manufactured with 316 stainless steel based on the 3-D drawings. Figure 23A) shows the back rim of the crawler prior to assembly and Figure 23 B) shows the outer bellow with the flanges modified to allow welding of the assembly.

Figure 23. A) Back rim, B) Outer bellow flange.

As mentioned previously, the crawler unit consists of an inner edge-welded bellow and a hydroformed outer bellow. The custom design allows for sequential welding of the bellows and rims. Figure 24 A) shows the inner bellow positioned with the rim prior to welding and Figure 24 B) shows the outer bellow positioned with the rim prior to welding.

Figure 24. A) Inner bellow and rim, B) Outer bellow and rim.

Design and assembly of the tether-reel system

The motion of the crawler is powered by pressurization/depressurization cavities. The TGPC design includes a 500 ft tether-reel assembly system. The tether assembly consists of three pneumatic lines, one hydraulic line, and one multi-conductor cable jacketed together. Figure 25A) shows the crawler attached to the tether. The reel system was designed to accommodate the tether and provides rotating connections to the pneumatic, hydraulic, and electrical lines (Figure 25B).

Figure 25. A) Tether attached to the crawler unit, B) Reel system.

RESULTS - THIRD GENERATION PERISTALTIC CRAWLER

Experimental testing

Anchoring force test

Pulling force tests were conducted to determine the anchoring force of the unit. These tests were performed using a single rim assembly and the setup shown in Figure 26. The setup consisted of a 3 ft, 3 in diameter Victaulic pipe, a spring scale (rated to 325 lb), and a manual winch. For each test, the rim cavity was first pressurized to the set pressure and then the cable was tensioned using the winch. The spring scale provided the pulling force reading for each set pressure. One of the challenges of reducing the outer diameter of the crawler from 2.75 inches to 2 inches is that the expansion requirements of the flexible cavities to anchor the unit to the pipeline needs to be increased by 100% in radius change. Since flexible PVC used on the 2nd generation crawler does not provide the elasticity required, two new materials were tested: gum and rubber. Gum provided a maximum anchoring force of 175 lb at 50 psi but ruptured after three minutes. Rubber provided a maximum anchoring force of 200 lb at 100 psi and did not burst during 5 minutes of testing.
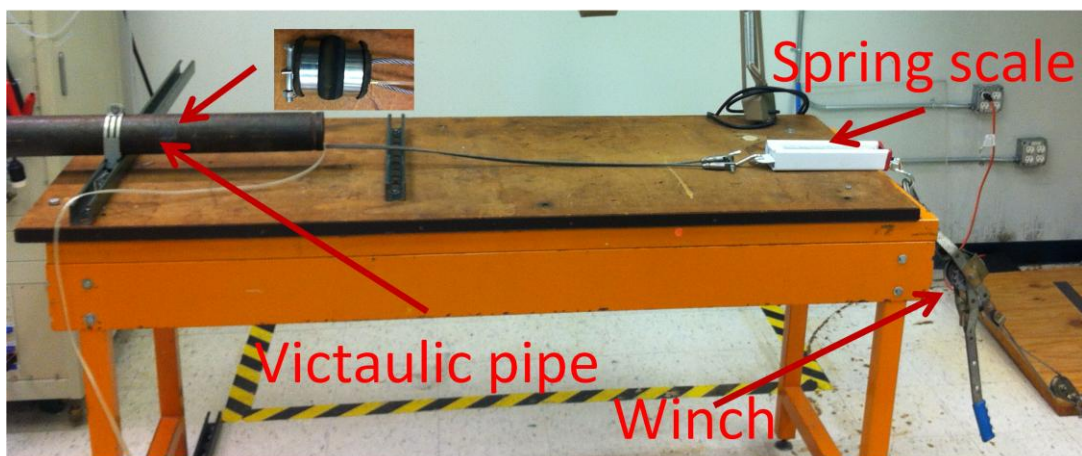
Figure 26. Experimental testbed to measure pulling force.

Bellow response test

The tests were conducted by inflating/deflating the bellow assembly at various pressure values to determine the optimal response time. To prevent permanent plastic deformation of the bellow assembly, the test matrix was limited to pressures ranging between 30 to 80 psi. The test sequence consisted of two cycles: (1) inflation cycle, during which - time was recorded to determine the time it took for the below to reach the preset pressure and (2) deflation cycle, during which - time was recorded for the bellow to go from preset pressure to the pressure in the vacuum. The final cycle time consisted of adding the deflation and inflation times. The inflation tests were done in increments of 10 psi. The bellow was placed in a 1 foot clear polyvinyl chloride (PVC) pipe and clamped on one end. A clearance of 1 inch was maintained between the other end of the bellow and the pipe by clamping a limiting end plate to the pipe. This was done to prevent overextension of the bellow. The largest cycle time recorded was 32.16 sec for a

maximum pressure of 60 psi inside the bellow assembly. The force recorded at this pressure was 133 lb. Figure 27 shows the setup used to perform the bellow response tests.

Figure 27. Setup used for bellow response tests.

Table 1 shows the experimental results recorded form the force tests performed.

Table 1. Experimental Results of the Bellow Force Tests

Inflation Pressure (psi)	Spring Displacement (in)	Force Exerted (lbs)
10	3/8	49.9
20	1/2	66.5
30	5/8	83.1
40	3/4	99.8
50	7/8	116.4
60	1	133.0

Tether response test

Cycle time tests for the bellow assembly were performed using two different tether lengths to investigate the effect of tether length on time require for pressurization and depressurization of the cavities. In order to pressurize/depressurize the bellow assembly using the current control valve configuration, it is required to first pressurize/depressurize the full tether length. As the length of the tether increases, the volume inside the lines of the tether increases, resulting in an increase of the cycle time to reach a pre-set pressure sequence. In addition, since air is a compressible fluid, the time required to reach higher pressures results in a further increase of cycle time. The largest cycle time recorded was 228 seconds using a 500-foot tether reaching 60 psi of pressure. The shortest cycle time, reaching the same pressure, was 11 seconds using a 23-foot tether. Table 2 and Table 3 show the experimental results for the 23-foot and 500-foot tether, respectively.

Table 2. Bellow Assembly Response Time Using a 23 ft Tether

Pressure (psi)	Compression time (sec)	Expansion time (sec)	Final time (sec)
10	5.50	3.11	8.60
10	5.26	2.98	8.24

10	5.34	3.16	8.50
20	6.14	3.21	9.35
20	5.59	3.18	8.77
20	5.98	3.21	9.19
30	6.70	3.29	9.98
30	6.84	3.26	10.10
30	6.81	3.34	10.15
40	6.80	3.51	10.31
40	6.66	3.59	10.25
40	6.59	3.61	10.20
50	6.91	3.77	10.68
50	6.94	3.66	10.60
50	7.06	3.69	10.75
60	7.10	3.76	10.86
60	6.86	3.70	10.56
60	7.15	3.81	10.96
70	7.92	3.96	11.88
70	7.90	3.88	11.78
70	8.07	3.91	11.98

Table 3.Bellow Assembly Response Time Using a 500 ft Tether

Pressure (psi)	Compression time (sec)	Expansion time (sec)	Final time (sec)	Total time (sec)
10	129.95	24.77	154.72	154.72
10	130.43	24.89	155.32	155.32
20	175.73	24.93	200.66	200.66
20	174.91	25.00	199.91	199.91
30	180.09	25.11	205.20	205.20
30	180.36	25.16	205.51	205.51
40	192.36	25.26	217.62	217.62
40	191.78	25.39	217.17	217.17
50	197.04	25.62	222.66	222.66
50	196.11	25.80	221.90	221.90
60	201.53	26.84	228.38	228.38
60	201.15	26.98	228.13	228.13

Speed test

Two speed tests were performed; one using a 15-foot tether and another using a 500-foot tether. Both tests were carried out inside a 3-inch diameter straight clear PVC pipe. For each length of tether, the PLC that controls the pneumatic valves was adjusted for the corresponding cycle time required. The 15-foot tether speed test was programmed for a 16 second cycle time and the 500-

foot tether test was programmed to have a 240 second (4 min) cycle time. For both tests the maximum pressure of the flexible cavities was set to 80 psi and the bellow maximum pressure was set to 20 psi. Figure 28 shows the crawler/pipeline configuration used to perform the speed test. The crawler recorded speed was 21 ft/ hr (0.35 ft/min) for the 15-foot tether and 1 ft/hr for the 500-foot tether.

Figure 28. Crawler speed test setup.

When compared to the 2nd generation crawler, the TGPC had a decrease in navigational speed from 0.5 ft/min to 0.35 ft/min. This reduction of speed is a consequence of the increase in stiffness of the bellow assembly resulting from the reduction of the outer diameter of the crawler. Evenhough an edge-welded bellow was used for the inner bellow, the increase in the axial stiffness of the outer bellow (decreased diameter), increases the cycle time of the unit.

Maneuverability Test

The crawler's ability to negotiate through elbows was tested in a testbed consisting of two straight 3" pipes and one 90° elbow. The improvements on the TGPC allowed the unit to turn in a Victaulic elbow (4.25 inches in radius). The time recorded for the crawler to clear the elbow was 11 minutes and 23 seconds. Figure 29 shows the sequence of the crawler turning through the 90° elbow.

Figure 29. Sequence of crawler turning through a 90° elbow.

Unplugging tests

The unplugging tests were performed using the experimental test set-up shown in Figure 30. One clear PVC pipe section was coupled with a 2 foot Victaulic carbon steel pipe. Prior to this testing phase, the Victaulic pipe was filled with a K-mag based plug. Two unplugging tests were performed, each one using a different type of high pressure water nozzle. The nozzles used were

a 3 inch rotating nozzle and a fixed 0.75 inch 15° nozzle. Figure 31A) shows the crawler with the rotating nozzle attachment and Figure 31B) shows the crawler with the 15° nozzle attachment. Each unplugging test was conducted for 2 hours. The rotating nozzle provide an unplugging rate of 9 in/hr and the 15° angle nozzle provided an unplugging rate of 5.75 in/hr.
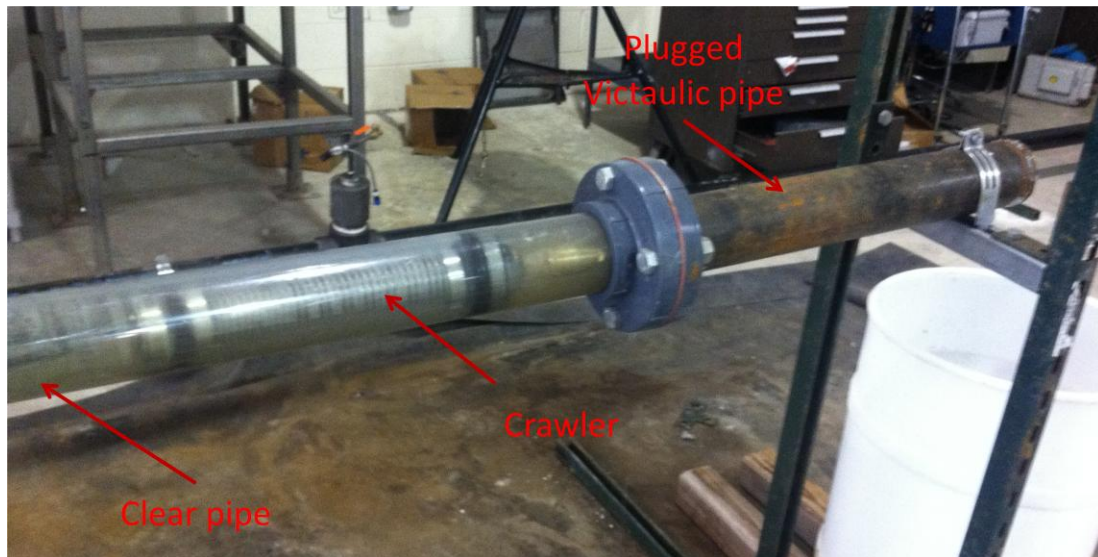
Figure 30. Experimental setup used for the unplugging tests.

Figure 31. A) Rotating nozzle B) 15° angle degree nozzle.

CONCLUSIONS AND FUTURE WORK

Two technologies, APS and a peristaltic crawler, have continued to be developed and evaluated during FY2011.

The APS was used on a lab scale testbed consisting of a symmetric configuration using approximately 18 ft of pipe with one 90° elbow on each side of a plug. A 2 foot K-mag plug was placed in the middle of the testbed and different operational parameters were used to determine the optimal configuration for loops that were fully flooded and loops with air entrained. For the fully flooded trials, only trials with a static pressure of 60 psi and a frequency of 2 Hz resulted in successful unplugging operations. Other trials at 60 psi with different frequencies resulted in unsuccessful unplugging operations. This suggests that resonance of the system played a role in the unplugging. Trials at 200 psi also did not yield successful results. For trials with water entrained in the pipeline (87.5% water by volume), the pump could only generate small pressure rises (less than 10 psi). This was due to a low water to pipeline-volume ratio and a piston pump system. Additionally, significant piston drift was observed. None of the air entrained trials resulted in an unplugging.

During the unplugging trials, excessive deflection was observed in the pipeline loop. Due to the flexibility in the connectors, the pipeline loop was redesigned using 3" SCH-40 threaded pipes. Threaded pipe was utilized to minimize pipeline deflection that would affect the pressure pulse propagation. During this follow up phase of testing, the pulse-response pipeline loop utilized only one side of a pipeline, however, the loop was extended to 135 ft. An additional focus of this phase is to be able to predict the system performance at longer pipe lengths and various configurations. Thus, a computational fluid dynamics model was utilized to simulate pressure variation in the pipeline and was validated with the experimental testing.

Future tests will add pipes and fittings to the pulse-response pipeline loop in order to analyze how the changes in pipeline geometry influence transient pulse propagation and reflection. In addition, the effects of air entrained within the pipeline will also be determined. Various amounts of air will be added to the system to determine the overall damping on the pulse. The data from all these tests will be used to extrapolate performance at longer lengths through the use of an improved CFD model that can accurately estimate the performance.

Based on results for the air entrained trials, alternative pressure sources for the asynchronous pulsing method will be investigated. Additionally, a vacuum source will be integrated into the design to minimize air entrainment. Future testing will include validation of the improved APS on a bench scale testbed as well as validation of its unplugging ability on engineering scale testbeds.

Results from the experimental testing of the TGPC demonstrated the effectiveness of the improvements to the 2nd generation crawler. The results include its navigational speed, capability to negotiate through a 90° elbow, anchoring force, and unplugging ability. Reduction of the outer diameter of the unit from 2.75 inches to 2.00 inches makes it feasible for the unit to navigate through a small Victaulic 3 inch elbow. The inner hydroformed bellow of the bellow assembly in the 2nd generation unit was successfully replaced with an edge-welded bellow. It was expected that this change would decrease the stiffness of the unit thus increasing the navigational speed of

the crawler. However, the decrease in the diameter of the unit resulted in a stiffer outer hydroformed bellow lowering the speed of the unit by 30%.

Test conducted using different tether lengths demonstrated that there is a significant reduction on speed of the crawler with increasing length of the tether. This decrease in speed is the result of the increase of volume required to be pressurized/depressurized inside the tether before the set pressure can be reached at the cavity in the crawler unit for each cycle. The speed of 1 ft/hr recorded using a 500-foot tether shows that the technology using the current configuration could not be effective for longer tethers. FIU is currently developing a system that will position the pneumatic valves in close proximity to the crawler unit as opposed to their existing location at the control unit. By positioning the valves close to the crawler, it will allow the tether to be set to a constant air pressure/vacuum making the cycle time independent of the tether length. Figure 32 shows the tested prototype for the valve/manifold configuration.

Figure 32. Solenoid/manifold prototype.

Anchoring force tests demonstrated that using the ¼ in thick rubber material custom made to the rim's outer diameter provides reliable performance to the tested 100 psi pressure, providing 200 lbs of pulling force. The pressure exerted by the clamps to hold the rubber material in place was controlled by measuring the torque applied during assembly. The torque required to prevent slippage of the rubber was 9 in-lbs.

The unplugging test showed that the rotating nozzle provides a 36% faster unplugging rate than the 15° nozzle. However, the rotating nozzle has a length of 3 inches which could make it difficult for the crawler to turn through a 90° elbow. The 15° nozzle is 0.75 inches long which makes it a better choice for maneuverability inside the pipeline. On both unplugging tests, the eroded K-mag material did not constrict flow through the crawler.

REFERENCES

1. Roelant, D., (2012). FY2011 Year End Technical Report. Chemical Process Alternatives for Radioactive Waste. U.S. Department of Energy, Office of Environmental Management.

2. Zollinger, W., & Carney, F. (2004). Pipeline blockage unplugging and locating equipment. *Conference on Robotics and Remote Systems- Proceedings*, (pp. 80 - 85). Gainesville.

TASK 12 FY11 YEAR END TECHNICAL REPORT
Multiple-Relaxation-Time Lattice Boltzmann Model for Multiphase Flows

EXECUTIVE SUMMARY

The U.S. Department of Energy (DOE) Hanford Site aims to develop computer software that can be used as a tool for understanding the physics of fluid flow in nuclear waste tanks during regular operations and retrieval tasks. Bubble generation due to chemical reactions and sludge mixing via air-bubble-lifters are examples of fluid-dynamics problems that could be investigated using accurate computer simulations to predict performance and avoid possible safety issues. In 2009, a new task was initiated as part of Florida International University's (FIU's) research efforts in order to develop a computational program, which is based on the lattice Boltzmann method (LBM) in order to simulate multiphase flow problems related to high-level waste (HLW) operations. In 2009, a thorough literature review was conducted to identify the most suitable multiphase fluid modeling technique in LBM and a single-phase multi-relaxation-time (MRT) code was developed. In 2010, FIU identified and evaluated a multiphase LBM using a single-relaxation-time (SRT) collision operator and updated the collision process with the computer program with a MRT collision model. During the current performance period, the MRT LBM code was extended into three dimensions and the serial computer code was converted into a parallel code. In this report, the findings of the multiphase LBM computer program obtained with single and multiple processor computers are presented and the verification of the multiphase 3D parallel MRT LBM computer code is shown. For static bubbles, it was found that MRT multiphase LBM were successful in capturing the surface tension force at the interface. In terms of dynamic bubbles, the MRT LBM was found to be capable of simulating various scenarios of bubble rising conditions. Further verification of the 3D simulations will be conducted using the parallel LBM in large domains by comparing the results against experimental conditions.

INTRODUCTION

As a result of atomic weapons production, millions of gallons of radioactive waste was generated and stored in underground tanks at various DOE sites. DOE is currently in the process of transferring the waste from single shell tanks to double shell tanks, during which various waste retrieval and processing methods are being employed. The storage and mixing of the liquid waste requires understanding the hydrological and rheological properties of the fluid inside the waste tanks. The fluid inside the waste tanks is comprised of multiple phases in which bubble dynamics plays an important role. Gas bubbles can exist in the waste entrapped in the liquid phase, inside cracks within the solid waste or on the surface of the tank walls. They can also be generated inside the waste naturally caused by chemical reactions such as hydrogen production or can be externally supplied via mechanical mechanisms such as air-purging, pulsed-air mixing etc.

An understanding of the physical nature of bubble dynamics inside the waste and the effects of the air release process to the tank environment need to be gained by considering various waste conditions. Such an analysis can be made possible by developing a numerical method that can simulate the process of air bubble generation inside tanks and that can accurately track the interactions of the gas phase with the surrounding fluid and solid phases. The final computational program would serve as a tool for Site engineers and scientists to predict waste behavior and improve operational procedures during the storage, handling and transfer of liquid waste.

In this report, a numerical method, the lattice Boltzmann method (LBM), is presented, which can model multiphase flows accurately and efficiently. LBM is advantageous over traditional Navier-Stokes based computational models since surface forces are handled more effectively in LBM. LBM has been mostly employed using the Bhatnagar-Gross-Krook (BGK) collision operator with a single-relaxation-time to simulate multiphase flows. This has brought a limitation when the fluid viscosity is low, which makes the LBM simulations unstable. In order to avoid instability issues, multiple-relaxation-time (MRT) lattice Boltzmann models were proposed that use a collision operator that can adjust the bulk and shear viscosities independently. In addition, two-phase flows with high density ratios brings a computational challenge in terms of numerical instabilities to LBM simulations for multiphase flows with density ratios larger than 10. The instability is considered to be generated as a result of large pressure gradients in the interfacial region between two phases. The performance of MRT LBM for multiphase flow simulations in three dimensions is investigated in this report.

The outline of the report is given as follows: first, the three-dimensional lattice Boltzmann method using the multi-relaxation time collision model is introduced in relation to the multiphase flows. Later, parallelization of the MRT LBM code is discussed. The results obtained are presented in comparison to analytical solutions. Finally, conclusions are drawn and discussions for future work are presented.

Numerical method

The lattice Boltzmann method developed for this task is based on the continuous Boltzmann equation given by

$$\frac{\partial f}{\partial t} + \boldsymbol{\xi} \cdot \nabla f + \boldsymbol{F} \cdot \nabla_\xi f = \Omega. \tag{1}$$

Here f is the single particle density distribution function, $\boldsymbol{\xi}$ is the particle velocity, $\boldsymbol{F}$ is the interfacial force and Ω is the collision term. The term $\nabla_\xi f$ can be approximated as,

$$\nabla_\xi f \approx \nabla_\xi f^{eq} = -\frac{\xi - \mathbf{u}}{\rho c_s^2} f^{eq}, \tag{2}$$

where f^{eq} is the equilibrium density distribution function, $\mathbf{u}$ is the macroscopic velocity, ρ is the density and c_s is the speed of sound. The continuous Boltzmann equation given in Eq. (1) can be discretized in the velocity space by expressing as

$$\frac{\partial f_\alpha}{\partial t} + \boldsymbol{\xi}_\alpha \cdot \nabla f_\alpha = \Omega + S_{f\alpha}, \tag{3}$$

where

$$e_\alpha \equiv \xi_\alpha = \begin{cases} (0,0,0) & , & \alpha = 0, \\ (\pm 1,0,0),(0,\pm 1,0),(0,0,\pm 1), & , & \alpha = 1,2,\cdots,6 \\ & , & \alpha = 7,8,\cdots,18 \end{cases} \tag{4}$$

and

$$S_{f\alpha} = \frac{(e_{\alpha i} - u_i)F_i}{\rho c_s^2} f_\alpha^{eq}. \tag{5}$$

In Eq. (4) α is the discrete particle velocity distribution using the D2Q9 lattice structure shown in Figure 33, e is the particle velocity between lattice points.
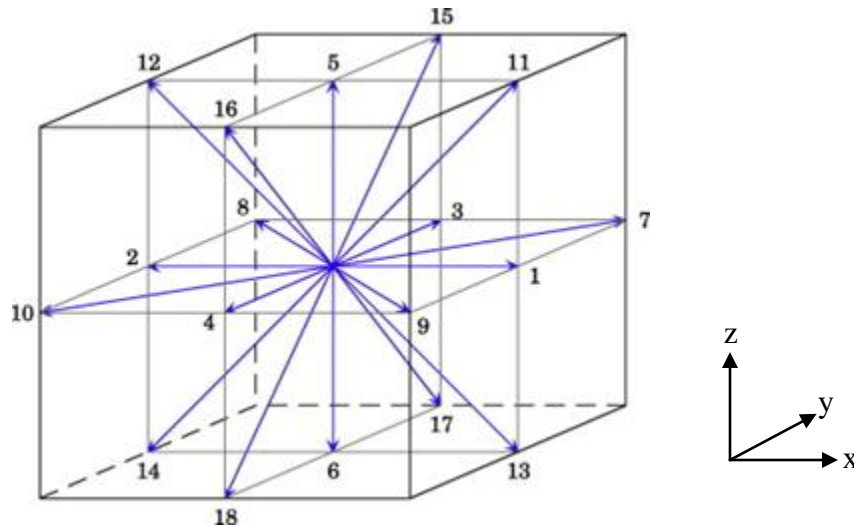
Figure 33. D3Q19 lattice structure.

In single-relaxation-time LBM, the collision term Ω is represented using the BGK model that uses a single relaxation time parameter (λ), $\Omega_c = -\left(\frac{f_\alpha - f_\alpha^{eq}}{\lambda}\right)$. In the MRT LBM, using a collision matrix Λ, the collision term on the right hand side of Eq. (3) is represented by

$$\Omega = -\Lambda_{\alpha\beta}\left(f_\beta - f_\beta^{eq}\right). \tag{6}$$

The equilibrium distribution function, f_α^{eq}, is written as

$$f_\beta^{eq} = w_\alpha \rho \left[1 + \frac{e_{\alpha i}u_i}{c_s^2} + \frac{(e_{\alpha i}e_{\alpha j} - c_s^2\delta_{ij})u_iu_j}{2c_s^4}\right], \tag{7}$$

where w_α is the weight function given by

$$w_\alpha = \begin{cases} /3, & \alpha = 0, \\ 1/18, & \alpha = 1,2,\cdots 6, \\ 1/36, & \alpha = 7,8,\cdots 18. \end{cases} \tag{8}$$

The force F_i in Eq. (5) is responsible for phase separation and is given by

$$F_i = \frac{\partial}{\partial x_j}(\rho c_s^2 - P)\delta_{ij} + \kappa\rho\frac{\partial}{\partial x_i}\frac{\partial^2\rho}{\partial x_j\partial x_j}. \tag{9}$$

Here, P is the pressure and κ is the surface tension parameter which is related to the surface tension σ through the relation

$$\sigma = \kappa\int\left(\frac{\partial\rho}{\partial r}\right)^2 dr, \tag{10}$$

where r is the direction of integration normal to the interface. The force F_i is expressed by Lee and Lin [1] as

$$F_i = \frac{\partial\rho c_s^2}{\partial x_j}\delta_{ij} - \rho\frac{\partial}{\partial x_i}\left(\frac{\partial E_f}{\partial\rho} - \kappa\frac{\partial^2\rho}{\partial x_j\partial x_j}\right). \tag{11}$$

E_f is the excess free energy at the interface over the bulk free energies and is obtained from an equation of state (EOS) expressed as follows:

$$E_f(\rho) \approx \beta\left(\rho - \rho_g^{sat}\right)^2(\rho - \rho_l^{sat})^2, \tag{12}$$

where β is a constant and ρ_g^{sat} and ρ_l^{sat} are densities of gas and liquid phases at saturation, respectively. This EOS results in a density profile given by

$$\rho(z) = \frac{\rho_l^{sat} + \rho_g^{sat}}{2} - \frac{\rho_l^{sat} - \rho_g^{sat}}{2}\tanh\left(\frac{2z}{D}\right), \tag{13}$$

where z is the spatial location normal to the interface and D is the interface thickness.

The constant β along with κ can control D and σ through the relation

$$D = \frac{4}{\left(\rho_l^{sat} - \rho_g^{sat}\right)}\sqrt{\frac{\kappa}{2\beta}}, \tag{14}$$

and

$$\sigma = \frac{\left(\rho_l^{sat} - \rho_g^{sat}\right)^3}{6}\sqrt{2\kappa\beta}. \tag{15}$$

The evolution equations given above for the particle density distribution function is mapped into the moment space by multiplying the terms in Eq. (3) with the transformation matrix $\boldsymbol{T}$

$$\boldsymbol{T}^T = \begin{vmatrix} \langle\rho|, \langle e|, \langle e^2|, \langle j_x|, \langle q_x|, \langle j_y|, \langle q_y|, \langle j_z|, \langle q_z| \\ \langle 3p_{xx}|, \langle 3\pi_{xx}|, \langle p_{ww}|, \langle \pi_{ww}|, \langle p_{xy}|, \langle p_{yz}|, \langle p_{xz}|, \langle m_x|, \langle m_y|, \langle m_z| \end{vmatrix},$$ (16)

where

$$|\rho\rangle = |e_\alpha|^0,$$ (17)

$$|e\rangle_\alpha = 19|e_\alpha|^0 - 30,$$ (18)

$$|e^2\rangle_\alpha = (421|e_\alpha|^{04} - 53|e_\alpha|^2 + 24)/2$$ (19)

$$|j_x\rangle_\alpha = e_{\alpha,x},$$ (20)

$$|q_x\rangle_\alpha = [5|e_\alpha|^2 - 9)]e_{\alpha,x},$$ (21)

$$|j_y\rangle_\alpha = e_{\alpha,y},$$ (22)

$$|q_y\rangle_\alpha = [5|e_\alpha|^2 - 9)]e_{\alpha,y},$$ (23)

$$|j_z\rangle_\alpha = e_{\alpha,z},$$ (24)

$$|q_z\rangle_\alpha = [5|e_\alpha|^2 - 9)]e_{\alpha,z},$$ (25)

$$|3p_{xx}\rangle_\alpha = 3e_{\alpha,x}^2 - |e_\alpha|^2,$$ (26)

$$|3\pi_{xx}\rangle_\alpha = (3|e_\alpha|^2 - 5)(3e_{\alpha,x}^2 - |e_\alpha|^2),$$ (27)

$$|p_{ww}\rangle_\alpha = e_{\alpha,y}^2 - e_{\alpha,z}^2,$$ (28)

$$|\pi_{ww}\rangle_\alpha = (3|e_\alpha|^2 - 5)(e_{\alpha,y}^2 - e_{\alpha,z}^2),$$ (29)

$$|p_{xy}\rangle_\alpha = e_{\alpha,x}e_{\alpha,y},$$ (30)

$$|p_{yz}\rangle_\alpha = e_{\alpha,y}e_{\alpha,z},$$ (31)

$$|p_{xz}\rangle_\alpha = e_{\alpha,x}e_{\alpha,z},$$ (32)

$$|m_x\rangle_\alpha = (e_{\alpha,y}^2 - e_{\alpha,z}^2)e_{\alpha,x},$$ (33)

$$|m_y\rangle_\alpha = (e_{\alpha,z}^2 - e_{\alpha,x}^2)e_{\alpha,y},$$ (34)

$$|m_z\rangle_\alpha = (e_{\alpha,x}^2 - e_{\alpha,y}^2)e_{\alpha,z}.$$ (35)

The resulting evolution equation in moment space takes the form

$$\frac{\partial \hat{f}_\alpha}{\partial t} + \hat{\boldsymbol{\xi}}_\alpha \cdot \nabla \hat{f}_\alpha = -\hat{\Lambda}_{\alpha\beta}\left(\hat{f}_\beta - \hat{f}_\beta^{eq}\right) + \hat{S}_{f\alpha},$$ (36)

where

$$\hat{f}_\alpha = \boldsymbol{T}f_\alpha,$$ (37)

$$\hat{f}_\alpha^{eq} = \boldsymbol{T}f_\alpha^{eq},$$ (38)

$$\hat{S}_{f\alpha} = \mathbf{T} S_{f\alpha}, \tag{39}$$

and

$$\hat{\Lambda} = \boldsymbol{T} \Lambda \boldsymbol{T}^{-1}. \tag{40}$$

The equilibrium distribution function in moment space is written as

$$(\hat{f}^{eq})^T = \begin{vmatrix} \rho, e^{eq}, (e^2)^{eq}, j_x, q_x^{eq}, j_y, q_y^{eq}, j_z, q_z^{eq} \\ 3p_{xx}^{eq}, 3\pi_{xx}^{eq}, p_{ww}^{eq}, \pi_{ww}^{eq}, p_{xy}^{eq}, p_{yz}^{eq}, p_{xz}^{eq}, m_x^{eq}, m_y^{eq}, m_z^{eq} \end{vmatrix}, \tag{41}$$

where the equilibrium distributions of the moments are given by

$$e^{eq} = -11\rho + 19(j_x^2 + j_y^2 + j_z^2)/\rho, \tag{42}$$

$$(e^2)^{eq} = w_\varepsilon \rho + w_{\varepsilon j}(j_x^2 + j_y^2 + j_z^2)/\rho, \tag{43}$$

$$q_x^{eq} = -\frac{2}{3}j_x, \tag{44}$$

$$q_y^{eq} = -\frac{2}{3}j_y, \tag{45}$$

$$q_z^{eq} = -\frac{2}{3}j_z, \tag{46}$$

$$p_{xx}^{eq} = \frac{1}{3}\left(2j_x^2 - (j_y^2 + j_z^2)\right)/\rho, \tag{47}$$

$$\pi_{xx}^{eq} = w_{xx}p_{xx}^{eq}, \tag{48}$$

$$p_{ww}^{eq} = (j_y^2 - j_z^2)/\rho, \tag{49}$$

$$p_{xy}^{eq} = (j_x j_y)/\rho. \tag{50}$$

$$p_{yz}^{eq} = (j_y j_z)/\rho. \tag{51}$$

$$p_{xz}^{eq} = (j_x j_z)/\rho. \tag{52}$$

$$\pi_{ww}^{eq} = w_{xx}p_{ww}^{eq}, \tag{53}$$

$$m_x^{eq} = 0, \tag{54}$$

$$m_y^{eq} = 0, \tag{55}$$

$$m_z^{eq} = 0. \tag{56}$$

In the works of d'Humieres et al. [3], the constants in Eqs. (42-56) are selected as $w_\varepsilon = 0$, $w_{\varepsilon j} = -475/63$ and $w_{xx} = 0$ for single-phase flows; however, in this work we follow the selection of Premnath and Abraham [2] used in their MRT LBM for multiphase flows where $w_\varepsilon = 3$, $w_{\varepsilon j} = -11/2$ and $w_{xx} = -1/2$.

The collision matrix in the moment space, $\hat{\Lambda}$, is given as

$$\hat{\boldsymbol{\Lambda}} = diag[s_1, s_2, s_3, s_4, s_5, s_6, s_7, s_8, s_9, s_{10}, s_{11}, s_{12}, s_{13}, s_{14}, s_{15}, s_{16}, s_{17}, s_{18}]. \tag{57}$$

The diagonal elements are inverses of relaxation times for the distribution functions in the moment space, $\hat{f}_\alpha$, and they are used to relax the equilibrium distribution functions in the

moment space, $\hat{f}_\alpha^{eq}$. In this work, the diagonal elements are selected as a combination of the values reported by d'Humieres [3] and Premnath and Abraham [2] as

$$\hat{\Lambda} = diag\left[1, 1.19, 1.4, 0, 1.2, 0, 1.2, 0, 1.2, \frac{1}{\tau}, 1.4, \frac{1}{\tau}, 1.4, \frac{1}{\tau}, \frac{1}{\tau}, \frac{1}{\tau}, 1.98, 1.98, 1.98\right]. \tag{58}$$

The parameters s_{10}, s_{12} and $s_{14\text{-}16}$ are related to the single relaxation time, τ, in the single-relaxation-time LBM and are used to determine the viscosity, $\nu = \frac{1}{3}\left(\frac{1}{s_{10}}\right)$ and the Reynolds number, $Re = UD/\nu$.

As discussed in Lee and Lin [1], it is possible to compute the hydrodynamic variables of interest such as local density ρ, velocity $\boldsymbol{u}$, and pressure P, from f_α. This approach, however, is prone to numerical instabilities due to the steep density gradients involved in the computation of the source term $S_{\alpha\beta}$. Therefore, a separate distribution function g is introduced to compute pressure and momentum. We denote g in the lattice velocity direction α as g_α. A pressure function p is also defined, which varies smoothly across the interface. It is related to the actual pressure P through

$$p = P - \kappa\rho\frac{\partial^2\rho}{\partial x_k\partial x_k} + \frac{\kappa}{2}\frac{\partial\rho}{\partial x_k}\frac{\partial\rho}{\partial x_k}. \tag{59}$$

In the bulk phase, $p \cong P$ as density gradients are nearly zero. Use of p in the momentum equation increases the stability of the scheme at high density ratios. This definition of P and the choice of D in Eq. (13) are critical to the capability of the model to simulate high density ratios. Based on the definition of p in Eq. (39), Eq. (9) for F_i may be re-arranged as

$$F_i = \frac{\partial}{\partial x_j}(\rho c_s^2 - p)\delta_{ij} + \kappa\frac{\partial}{\partial x_j}\left(\frac{\partial\rho}{\partial x_k}\frac{\partial\rho}{\partial x_k}\delta_{ij} - \frac{\partial\rho}{\partial x_i}\frac{\partial\rho}{\partial x_j}\right). \tag{60}$$

However, within this framework of the MRT model, the pressure evolution equation must now be formulated to have a non-diagonal collision matrix.

To develop an evolution equation for pressure in moment space that is similar to Eq. (26), Lee and Lin proposed

$$\hat{g}_\alpha = \hat{f}_\alpha + \left(\frac{p}{c_s^2} - \rho\right)\hat{\Gamma}_\alpha(0), \tag{61}$$

where

$$\hat{g}_\alpha = \mathrm{T}g_\alpha, \tag{62}$$

$$\Gamma_\alpha(\mathrm{u}) = \frac{f_\alpha^{eq}}{\rho}, \tag{63}$$

and

$$\hat{\Gamma}_\alpha(0) = \mathrm{T}\hat{\Gamma}_\alpha(0). \tag{64}$$

From Eq. (41), the total derivative of $\hat{g}_\alpha$ can be written as

$$\frac{D\hat{g}_\alpha}{Dt} = \frac{D\hat{f}_\alpha}{Dt} + \frac{1}{c_s^2}\frac{Dp}{Dt}\hat{\Gamma}(0) - \frac{D\rho}{Dt}\hat{\Gamma}(0)\,, \tag{65}$$

which can be simplified to

$$\frac{D\hat{g}_\alpha}{Dt} = \widehat{\Omega}_c + \hat{S}_{g\alpha} \tag{66}$$

where

$$\hat{S}_{g\alpha} = \mathrm{T}S_{g\alpha}\,, \tag{67}$$

$$S_{g\alpha} = \frac{(e_{\alpha i} - u_i)\partial_i(\rho c_s^2 - p)}{c_s^2}(\Gamma_\alpha(u) - \Gamma_\alpha(0)) \\ + \frac{(e_{\alpha i} - u_i)\left[\kappa\partial_i(\partial_k\rho\partial_k\rho) - \kappa\partial_j(\partial_i\rho\partial_j\rho)\right]}{c_s^2}\Gamma_\alpha(u)\,, \tag{68}$$

and

$$\widehat{\Omega}_c = -\widehat{\Lambda}_{\alpha\beta}\left(\hat{f}_\beta - \hat{f}_\beta^{eq}\right). \tag{69}$$

To express Eq. (49) as a function of $\hat{g}$ we define

$$\hat{g}_\alpha^{eq} = \hat{f}_\alpha^{eq} + \left(\frac{\rho}{c_s^2} - \rho\right)\hat{\Gamma}_\alpha(0)\,. \tag{70}$$

From this we get the following pressure evolution equation in moment space as

$$\frac{D\hat{g}_\alpha}{Dt} = -\widehat{\Lambda}_{\alpha\beta}\left(\hat{g}_\beta - \hat{g}_\beta^{eq}\right) + \hat{S}_{g\alpha}\,, \tag{71}$$

The macroscopic properties of density, momentum and pressure are obtained from the following relations:

$$\rho = \sum_\alpha f_\alpha\,, \tag{72}$$

$$\rho u_i = \sum_\alpha e_\alpha g_\alpha + \int_t^{t+\delta_t} \kappa\left[\frac{\partial}{\partial x_i}\left(\frac{\partial\rho}{\partial x_k}\frac{\partial\rho}{\partial x_k}\right) - \frac{\partial}{\partial x_j}\left(\frac{\partial\rho}{\partial x_i}\frac{\partial\rho}{\partial x_j}\right)\right]dt\,, \tag{73}$$

$$p = c_s^2\sum_\alpha g_\alpha + \int_t^{t+\delta_t} u_i\frac{\partial\rho c_s^2}{\partial x_i}dt\,. \tag{74}$$

RESULTS

In the first numerical test case presented here, a cubical three-dimensional bubble was generated in a fluid domain by assigning an initial density profile. The fluid domain was 51x51x51 lattice units (lu) in size and the bubble radius was 15 lu. The surface tension was imposed as an input parameter. The density ratio was set to 1.11 and the viscosity ratio between the fluids was 1.11. This test case was performed for demonstration of the effect of surface tension on the bubble shape. As seen in Figure 34, the interfacial tension on the bubble tends to minimize the surface area of the bubble and a spherical bubble shape is obtained as time progresses in the simulation.

(a) T = 0

(b) T = 200

(c) T = 500

(d) T = 1000
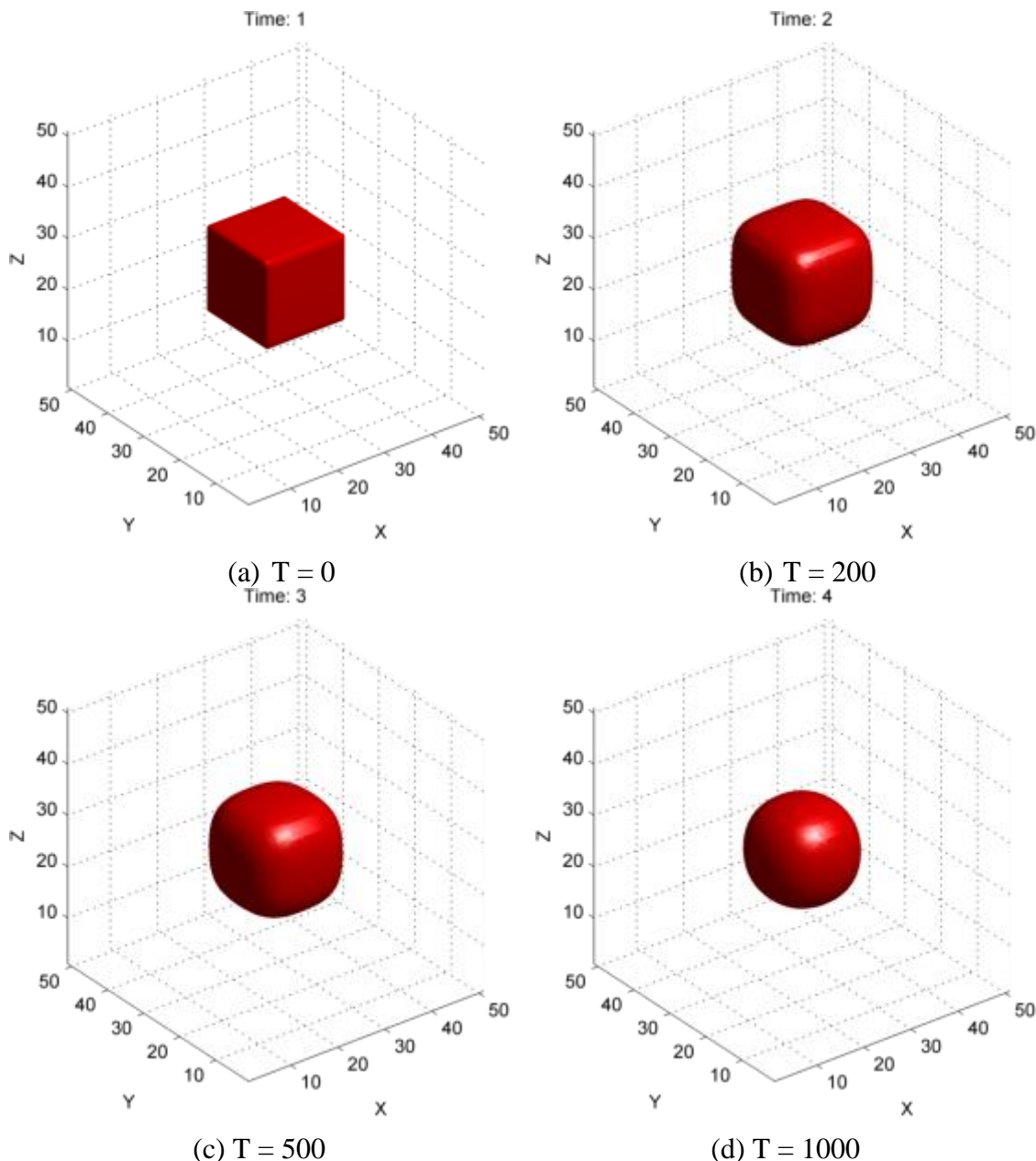
Figure 34. Evolution of a initially cubical bubble during time into a spherical bubble due to the effect of surface tension (T is given in dimensionless lattice time units).

In order to validate the implementation of the surface tension, the initial condition was changed to a spherical bubble at a fixed radius with imposed surface tension and an initial pressure distribution. The initial conditions were set to have density and viscosity ratios of 100 between the two fluids. The initial pressure field in the fluid domain was uniform; however, as the system converged to an equilibrium state, a pressure difference between the fluid domain and the gas domain was created. The relaxation of the interface between the two fluids was tested against the Laplace's law that expresses the pressure difference between the inside and the outside of a bubble as a function of the surface tension and the radius as given in two-dimensions by, $\Delta P = \sigma/R$. The difference of pressure between the inside and the outside of the bubble, P_{diff}, was computed at every time step and the relative error against the exact value is calculated as, $P_{err} = (P_{diff} - \Delta P)/\Delta P$. The convergence of P_{err} was measured at every 10 iterations by $Conv(i) = (P_{err}(i) - P_{err}(i-1))$ and the simulation was assumed to converge to a steady state result when $\varepsilon = 0.1 \sum_{i=1}^{10} Conv(i) < 0.05$.

Figure 35 shows the calculated pressure difference across the fluid interface for various bubble radii. The slope of the linear curve fit to the data provides the obtained surface tension value from the simulations. It was found that an error of 0.5 % - 0.87 % was obtained for the calculated pressure difference as compared to the analytical solution.
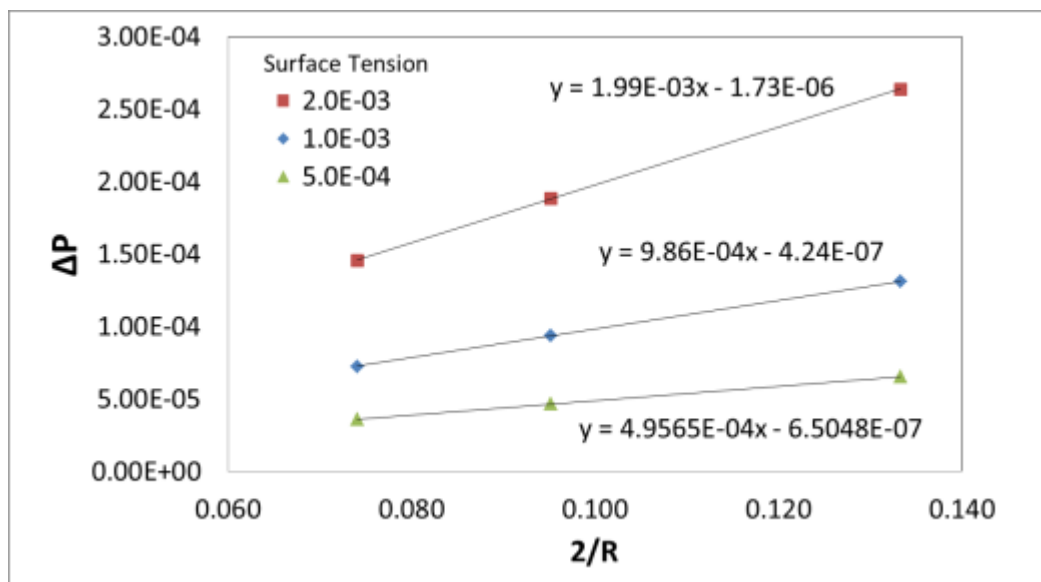
Figure 35. Pressure difference across the bubble as a function of radius for different values of surface tension (given in dimensionless units).

The LBM was verified for static bubble cases where the buoyancy force applied on the bubble was ignored, however, the effect of the gravity should be considered when using computer simulations to solve the engineering problems related to DOE waste handling operations. Therefore, the LBM is expected to be applicable to such cases where the buoyancy force applied on the gas phase should be considered. In order to evaluate whether the LBM used in this study can successfully simulate multiphase flows with external body forces such as gravity applied on one phase of the system, a preliminary test case was simulated for a dynamic bubble moving under the effect of a buoyancy force. The fluid domain was 51x51x201 lattice units (lu) in size and the bubble radius was 20 lu. The surface tension was imposed as an input parameter

(σ=0.0001). The density ratio was set to 4 and the viscosity ratio between the fluids was 4. Periodic boundary conditions were applied at all sides of the computational domain. The gravitational force was applied by modifying the macroscopic velocity and evolution equations with the additional buoyancy force term, $-\rho\Delta g$. Figure 36 shows the shape evolution of the spherical bubble during the rising process. As expected the shape of the bubble changes due to the surrounding fluid as it rises in the vertical direction and an elongated ellipsoidal bubble shape is obtained. In Figure 37 to Figure 39 various scenarios of rising bubble simulations are presented in order to show the capability of the LBM simulations. Although this analysis needs to be verified against benchmark solutions, the preliminary results obtained using LBM for buoyant 3D bubbles are encouraging and suggest that the proposed multiphase LBM presented in this paper can be useful for multiphase systems with moving discrete phases.
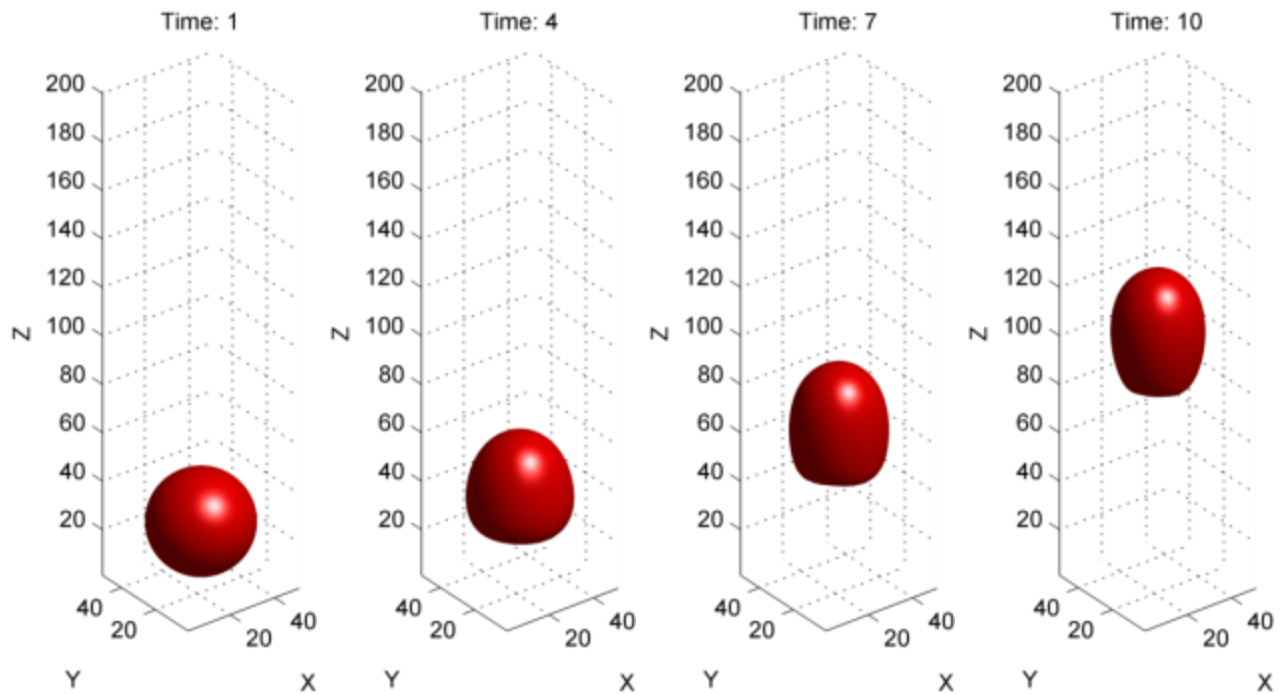
Figure 36. 3D Multiple Relaxation Time LBM simulation for the evolution of a single rising bubble

(Time= dimensionless lattice time units).
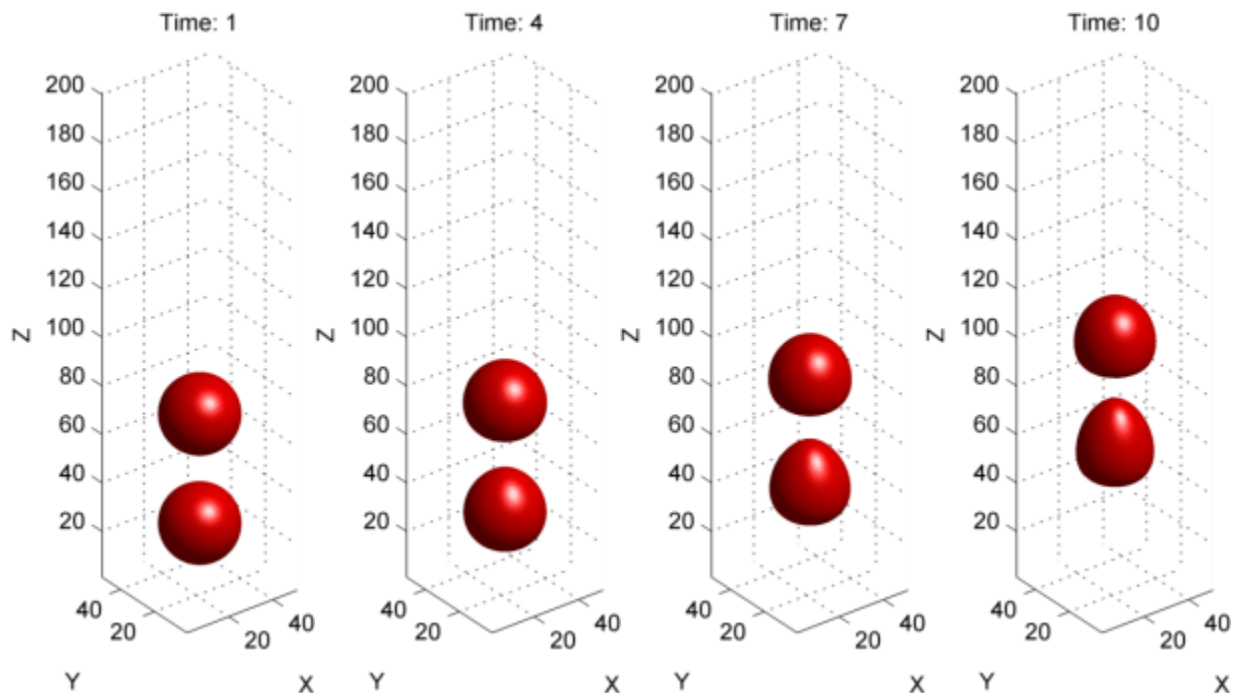
Figure 37. 3D Multiple Relaxation Time LBM simulation for the evolution of two identical rising bubbles (Time= dimensionless lattice time units).
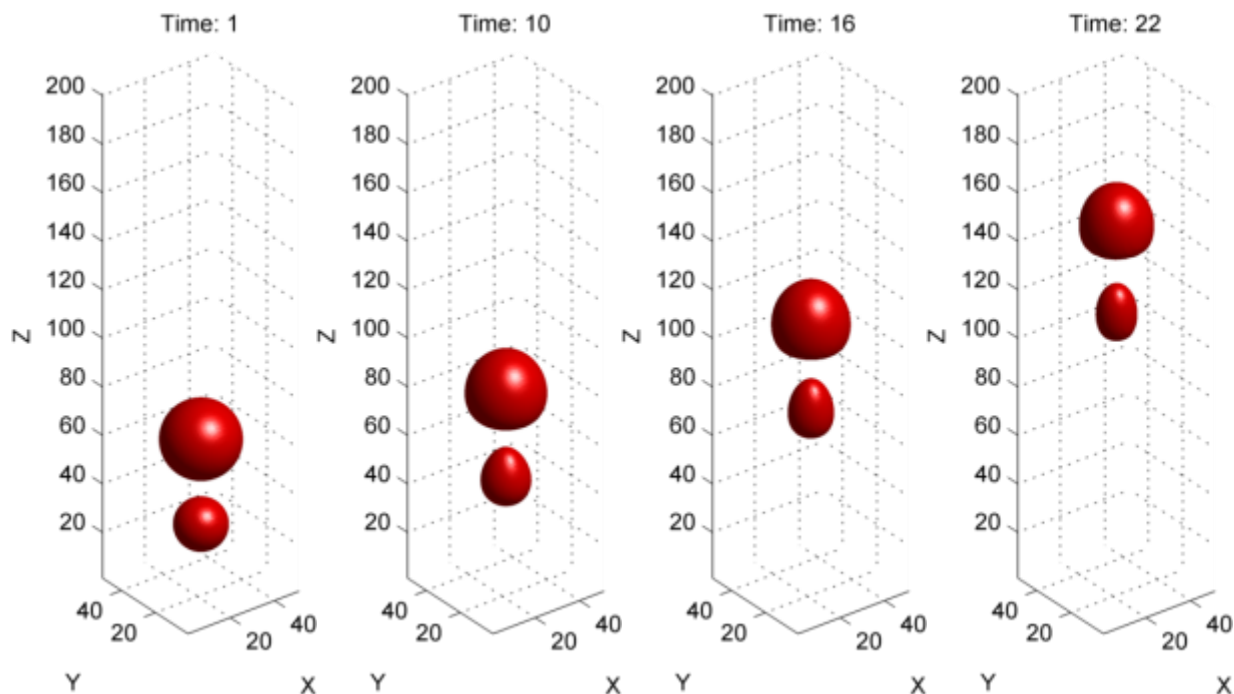
Figure 38. 3D Multiple Relaxation Time LBM simulation for the evolution of two non-identical rising bubbles (Time= dimensionless lattice time units).
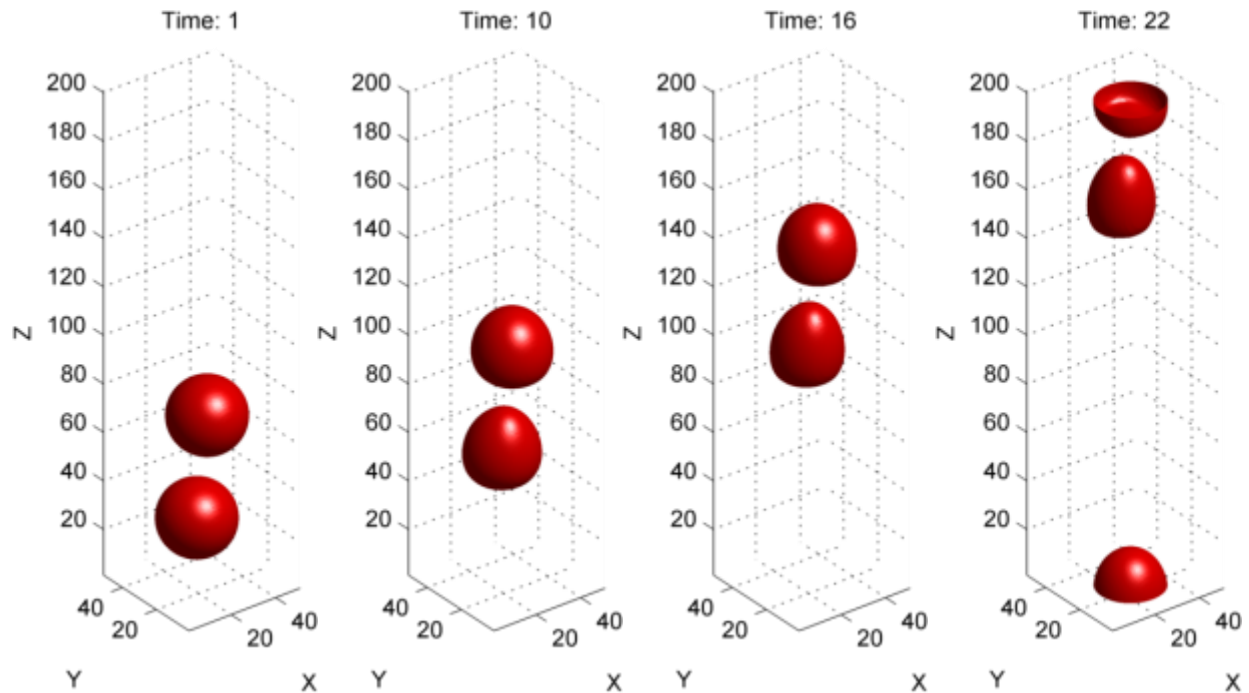
Figure 39. 3D Multiple Relaxation Time LBM simulation for the evolution of initially misaligned rising bubbles (T= dimensionless lattice time units).

Parallelization of the LBM

The parallel LBM code was obtained by combining the serial code written in Fortran 90 with the MPI commands that allow the information exchange between the number of processors that are used. The parallel LBM code splits up the computational domain depending on the number of subdomains in the X, Y and Z directions, and each subdomain is assigned to a separate processor. For a domain of 80x80x80 lattice points, allocation of 8 processors would result in 8 subdomains of 40x40x40 in size, which reduces the total computation time. The output data obtained from each processor is combined at the end of the iterations in order to visualize the full computational domain. This procedure is demonstrated in Figure 40 for a two-dimensional case.
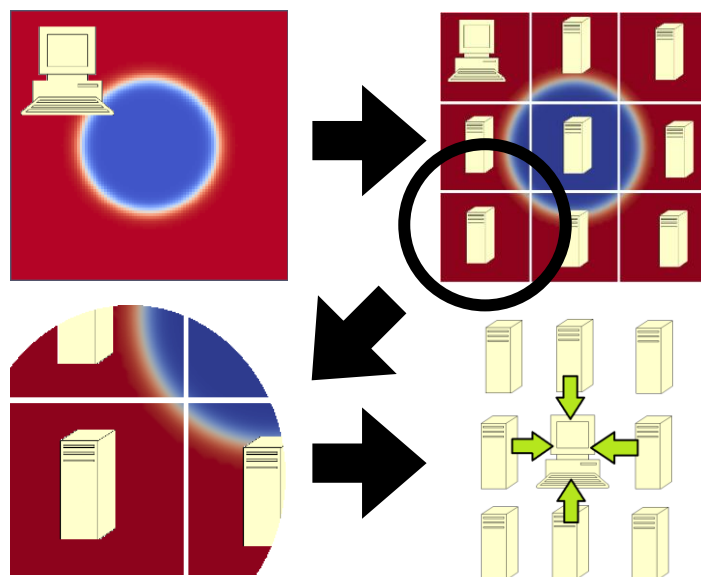
Figure 40. Domain decomposition used in the 2D LBM parallel code.

In order to validate that the message passing in the parallel LBM code, a benchmark problem was simulated for a static spherical bubble with a fixed radius placed initially in a cubical domain filled with a liquid (Figure 41). The surface tension between the two fluids was set and an initial equal pressure distribution was assigned for both phases. The initial conditions were set to have density ratio of 10 and viscosity ratio of 8 between the two fluids. The initial pressure field in the fluid domain was uniform; however, as the system converged to an equilibrium state, a pressure difference between the fluid domain and the gas domain was created. The relaxation of the interface between the two fluids were tested against the Laplace's law that expresses the pressure difference between the inside and the outside of a bubble as a function of the surface tension and the radius as given in three-dimensions by, $\Delta P = 2\sigma/R$. The difference of pressure between the inside and the outside of the bubble, P_{diff}, was computed at every time step and the relative error against the exact value is calculated as, $P_{err} = (P_{diff} - \Delta P)/\Delta P$. The convergence of P_{err} was measured at every 10 iterations by $Conv(i) = (P_{err}(i) - P_{err}(i-1))$ and the simulation was assumed to converge to a steady state result when $\varepsilon = 0.1 \sum_{i=1}^{10} Conv(i) < 0.01$.

Figure 42 shows the calculated pressure difference across the domain centerline for bubble radius of 15 lattice units. The pressure profile obtained using the parallel code matches the serial implementation perfectly which shows that the information passing in the parallel code was achieved successfully. The results of the 3D parallel LBM code are within 1% of the analytical solution.
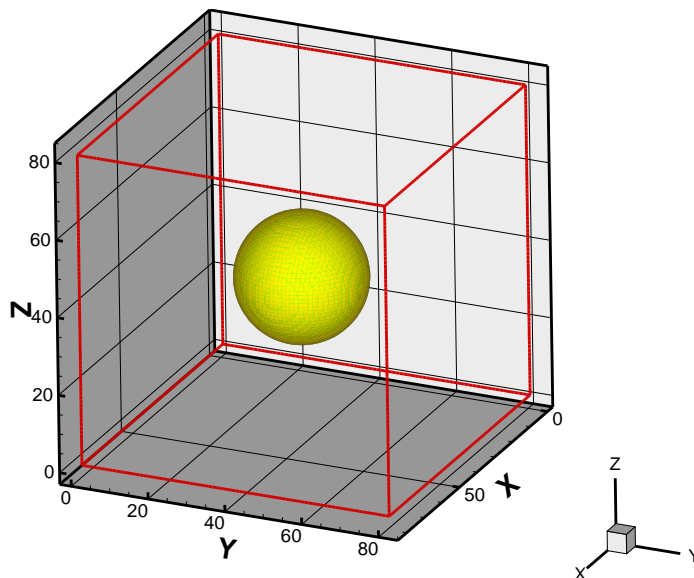
Figure 41. A static bubble in equilibrium within a liquid (not shown).
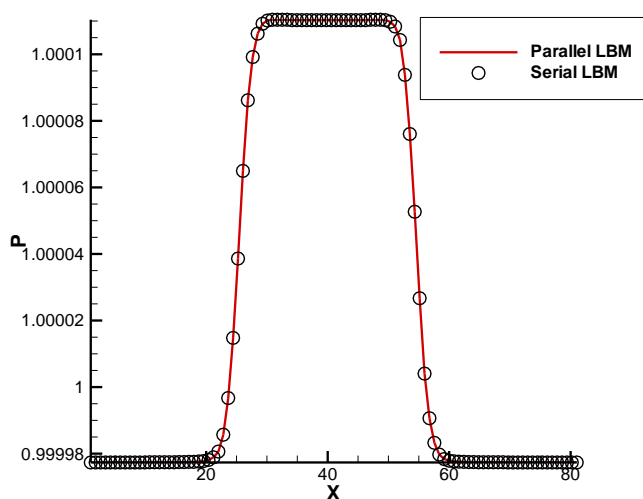
Figure 42. Pressure distribution across the domain centerline calculated using the serial and parallel LBM codes.

In order to investigate the performance of the parallel LBM code, a scale-up analysis has been conducted where the computation times required to finish the three major sections of the code have been analyzed for increasing number of computer processors. The major subroutines in the LBM algorithm that consume computational power are the pre-streaming, hydrodynamics and post-streaming subroutines for which the computation times are shown in Figure 43. It was observed that the time required completing the computations in these subroutines decay exponentially when the number of processors is increased. However, the gain in the computation time is reduced beyond a certain point where message passing between the processors take up a significant amount of time as compared to the time to finish the computations.

(a) Pre-streaming subroutine

(b) Hydrodynamics subroutine

(c) Post-streaming subroutine
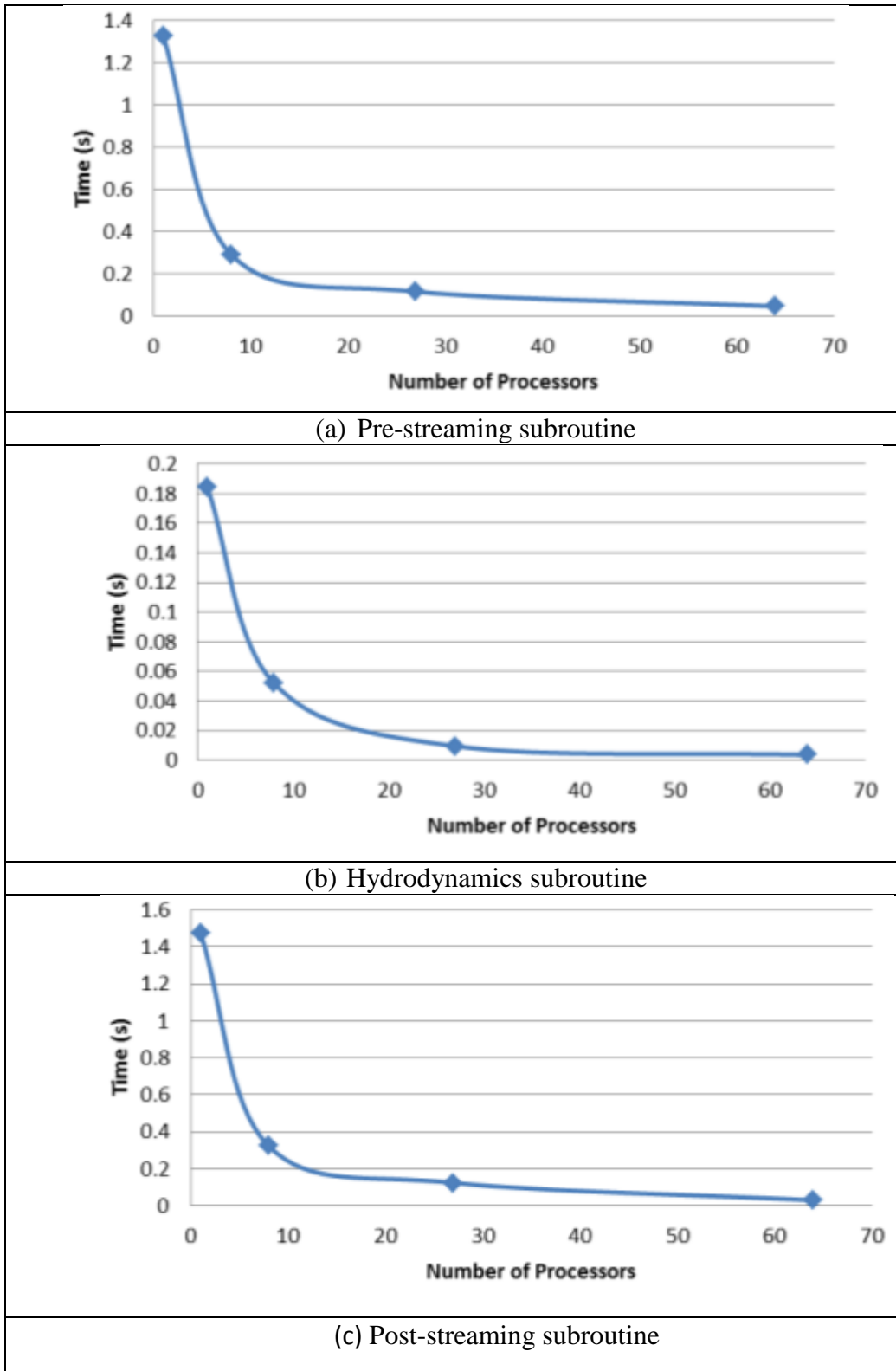
Figure 43. Computational time needed to complete three major parts of the LBM code was reduced by allocating more processors.
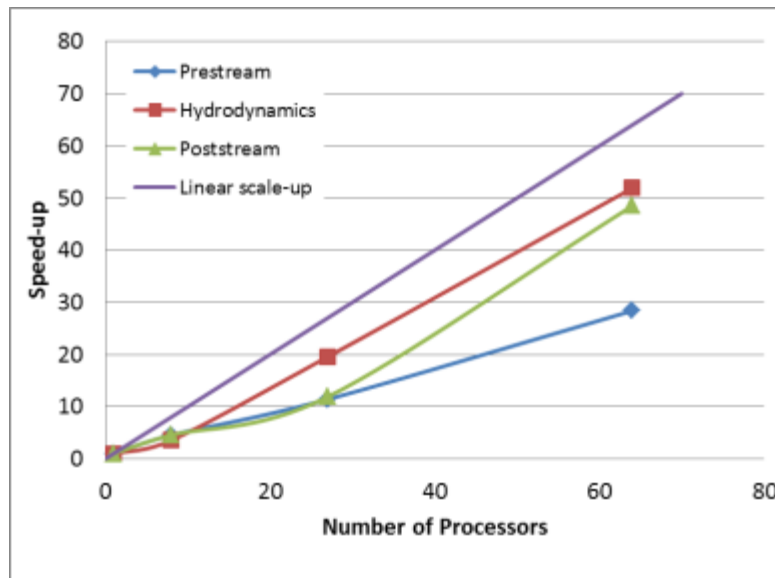
Figure 44. Speed-up performance for three major parts of the 3D LBM compared to linear scale-up.

Figure 44 shows that the scale-up value (Speed-up=$T_{serial}/T_{parallel}$) for these subroutines are not far from a linear behavior which holds for a perfectly ideal parallel code where time to exchange information among processors is negligible.

CONCLUSIONS

In this study, the implementation of a Multiple Relaxation Time LBM based on the Lee and Lin multiphase model was presented for static and dynamic bubbles in three dimensional domains. Validation cases against analytical solutions for static bubble have been presented and the capability of the method to simulate dynamic interface tracking for a buoyant bubble rising problem has been shown. The numerical method based on a multiphase LBM established with this research effort was able to provide promising preliminary results. However, further analysis of the accuracy of the method needs to be performed and the validation of the dynamic bubble simulations with appropriate wall boundary conditions to simulate flows in closed domains will follow as future work.

The implementation of a parallel MRT LBM based on the Lee and Lin multiphase model was also presented for a static bubble in three dimensional domains. Validation cases against analytical solutions for static bubble have been presented and the capability of the parallel LBM code for reducing the computation time has been observed. Computational savings up to 50% was achieved using the parallel LBM as compared to the serial code. Future work will include implementation of a CAD geometry integration algorithm with a mesh generation procedure and appropriate boundary conditions for solid surfaces in order to allow the simulation of complex geometry problems involving multiphase flows in confined domains.

REFERENCES

1.   Lee, T., & Lin, C.-L. (2005). A stable discretization of the lattice Boltzmann equation for simulation of incompressible two-phase flows at high. Journal of Computational Physics, 206, 16-47.

2.   K. N. Premnath and J. Abraham, "Three-dimensional multi-relaxation time (MRT) lattice-Boltzmann models for multiphase flow," Journal of Computational Physics, vol. 224, pp. 539-559, 2007.

3.   D. D'Humières, I. Ginzburg, M. Krafczyk, and P. & Luo, L.-S. Lallemand, "Multiple-relaxation-time lattice Boltzmann models in three dimensions," Royal Society of London Philosophical Transactions Series A, vol. 360, p. 437, 2002.

TASK 15 FY11 YEAR END TECHNICAL REPORT
Evaluation of Advanced Instrumentation Needs for HLW Retrieval

EXECUTIVE SUMMARY

As the DOE's Hanford site begins preparations for the transfer of high-level radioactive waste (HLW) from the double-shell tanks (DST) to the Waste Treatment and Immobilization Plant (WTP), the influence of waste feed consistency on the waste stabilization process – and final stabilized waste form - is currently under analysis. In order to characterize feed consistency prior to transfer, a suite of instrumentation will be required to monitor the waste preparation and mixing process in real time. FIU has focused its instrumentation efforts on identifying improvements to the in-situ, near-real time monitoring of the mixing process. Specifically, this project has identified innovative technologies applicable for in-tank monitoring during the mixing process.

After the current technology baseline plan and previous research efforts were reviewed, FIU began an extensive literature and technology search for applicable systems that could provide waste parameters within the HLW tank environment. The literature search focused on available methodologies for in-situ analysis of slurries, emulsions and suspensions applied in all industries. In particular, the monitoring of bulk density and/or particle concentration/characteristics measurements was the focus of the search. For the technology search, vendors of applicable techniques were identified and contacted. The searches resulted in several academic, commercial and governmental reports/articles applicable to the monitoring needs of the HLW tanks. Instrumentation specifications were collected and reviewed to identify the technology capabilities and limitations. These capabilities were also used for a comparative analysis between technologies. Based on the information, all the technologies were down selected to five applicable systems/methods that could provide useful information if deployed in a HLW tank. The five applicable methods applicable to the in-situ monitoring of the waste feed consistency were focused beam reflectance measurement (FBRM), optical back-reflectance measurement (ORM), ultrasonic spectroscopy (USS), Lamb/Stoneley wave viscosity measurement, and vibration-based densitometers. Based on literature results and commercial options, the ultrasonic and vibration-based techniques showed the most promise for developing a technology that could be used for in-situ measurements within the aggressive environment of a HLW tank. Specifically, the vibration-based and USS systems can provide information on the density and concentrations of the mixed slurry. These techniques can be engineered for monitoring at various depths within the tank.

Once the most promising techniques were selected, an experimental approach was defined. The approach would look at technology monitoring limitations in two phases; phase I would determine how the technologies could measure the slurry parameter, and how that measurement compared to laboratory or baseline techniques. This phase would be used as a go/no-go decision point to determine if further investigation of the technology was warranted. The second phase would focus on which specific factors and interactions would influence the measurement (particle size and shape, solid-fluid density ratio, carrier fluid viscosity, etc). The USS

measurement would be compared to a commercially available density meter that utilizes an accurate and repeatable technique for density measurement. A setup was conceived that allowed the testing of the USS and a commercially-available Coriolis mass flow meter side-by-side. The setup used a 10-gallon tank for agitation of the simulated slurry mixtures, with both systems sampling at the same location; the USS system probe was lowered into the tank, while a pick-up tube was used to transfer mixture to the Coriolis meter. In addition, the USS was subjected to several tests using a benchtop setup for more controlled evaluations of its concentration tracking capabilities. Both these systems were subjected to solutions and suspensions that would simulate some of the physical and rheological properties of the HLW slurry found in AY-102. The simulated slurries consisted of one to three distinct solids suspended in a water or $NaNO_3$ solution as the supernatant.

FIU tested the USS between May and October of the previous year with delays associated with hardware and software issues that plagued the device under evaluation. In August, the system had to be returned to the vendor as a result of a hardware fault. A new system was sent to FIU in October, and was used to complete testing. The results indicate that the technology can provide a measurement of density, but the frequency at which it occurs varies with slurry characteristics. If one frequency is selected for analysis, the density values vary more than 10% when compared to the reference value. One major issue that occurred during testing was that the spectral response profile of the USS system changed between hardware changes, and this was something that the vendor attributed to an issue with the reference file used for the tests.

In order to address issues with system inconsistency, additional bench-scale tests are being prepared for at ITS facilities during the first quarter of the next performance period. The testing will perform similar concentration and solids loading profiles in an attempt to determine the root cause for the inconsistency of results, as well as to compare the results to the FIU data. The USS utilized will have a slightly larger transducer than those tested at FIU. This will be a modification that will be required on any system deployed in the HLW tanks. Additional modifications to the system and hardware testing will be necessary before this technology can move forward for future development and deployment into a HLW tank.

INTRODUCTION

The US Department of Energy's (DOE) Hanford site is completing development of the Waste Treatment and Immobilization Plant (WTP), and preparing for the processing of over 54 million gallons of high-level radioactive waste (HLW). This waste shall be mixed within storage tanks, transferred to staging tanks, and processed by the WTP for final disposal. As the WTP development is completed, the window to integrate additional instrumented systems into the process loop will close. One such area that could benefit from additional instrumentation is the HLW tanks where this waste is currently stored. These +1M gallons of waste must be mixed into slurry that can be retrieved via pipelines to other tanks, or to WTP. The ability to characterize slurry in-tank would greatly optimize the mixing and retrieval processes. After several years of experience in the development of remote monitors for HLW tanks, FIU has undertaken a task to evaluate additional characterization and monitoring technologies that could be scaled-up for deployment inside the HLW tanks at Hanford.

As Hanford and PNNL perform laboratory testing of the slurry mixing phenomenon with various technologies, as well as the effect of slurry rheology on the mixing process, the inability to maintain a homogeneous mixture in a larger scale is evident. The recent analysis of AZ-101 transfer performed in 2001 concluded that less than a third of the particulate required for a homogeneous mixture were actually suspended during mixing [1]. When this is looked at from the perspective of a HLW feed that will be provided to WTP, the potential for variability in the slurry properties as it enters WTP could greatly impact the process throughput, even for waste from the same tank.

The Process Technology hot cells at WTP currently do not hold sufficient instrumentation to perform the types of analysis necessary for feed pre-qualification. Also, no pre-qualification criteria for the feed slurry has been defined as of yet. Several waste slurry characterizations have been recommended for compositional analysis and rheological properties [2]. In order to accomplish these characterizations prior to retrieval, an instrumented flow loop located above the tank will be added to the output from the tank feed pump. This would allow for characterization of several rheological properties as the waste is being mixed, retrieved, and proceeds to staging tanks at WTP. Also, additional sampling and laboratory analysis of samples extracted from the mixed tank shall also be used for compositional and rheological characterization. Technologies such as laser diffraction, ultrasonic doppler velocitometry (UDV), ultrasonics (US) densitometry, Coriolis meters, Raman spectroscopy and XRD will be included in these two sampling scenarios.

The two characterization methods can be supplemented with additional capability for in-tank characterization. The ability to either compare retrieve slurry with in-tank measurements, or provide supplemental information on slurry composition/properties could potentially save time and costs in the WTP process loop by allowing operators to make changes to mixed slurry – or the mixing process itself - prior to staging at WTP. The appropriate technology deployed in the HLW tanks could estimate the amount of mixing that is occurring within the tank in real-time, which can help address issues with solids level suspension, as well as characterization of the mixture as a function of tank height. This supplemental characterization and monitoring scenario is the focus of this project. Based on the discussions with the site representatives from WRPS, several general instrumentation guidelines were established. FIU used these to evaluate

promising in-situ candidate technologies. The guidelines were focused on deployment and operation in the HLW tanks. The guidelines were,

•   Operate in an in-tank configuration within the chemical, physical and radiological-aggressive tank environment

•   Sample and characterize while tank mixers are operating (fluid motion, electrical/acoustic noise, vibration, etc)

•   Work around/with air lift circulators

•   Bench-scale performance can be correlated to real-world scaled-up operation

•   Ability to measure vertical profile of a particular parameter (e.g. solids concentration, bulk density); ability to use data from multiple probe locations to generate parameter maps (interpolation can be used)

•   Ability to measure solids parameters of those being suspended from those stationary (size, composition, density, etc)

This project began with a review of the current state of technology applicable to the monitoring of HLW feed during the mixing and transfer process. The review examined the previous works by PNNL, the site contractors, and academia in identifying and implementing technologies that can monitor critical physical and rheological parameters of the waste. Discussions with site representatives established the current technology implementation plan[1] for the double-shell tanks that will be used to stage waste feed for WTP; these discussions were also a reference to minimize duplicative efforts into areas that had already been evaluated by other parties.

After the current technology baseline plan and previous research efforts were reviewed, FIU began an extensive literature and technology search for applicable systems that could provide waste parameters within the HLW tank environment. The literature search focused on available methodologies for in-situ analysis of slurries, emulsions and suspensions applied in all industries. In particular, the monitoring of bulk density and/or particle concentration/characteristics measurements was the focus of the search. For the technology search, vendors of applicable techniques were identified and contacted. The searches resulted in several academic, commercial and governmental reports/articles applicable to the monitoring needs of the HLW tanks. Instrumentation specifications were collected and reviewed to identify the technology capabilities and limitations. These capabilities were also used for a comparative analysis between technologies. Based on the information, all the technologies were down selected to five applicable systems/methods that could provide useful information if deployed in a HLW tank. The five applicable methods applicable to the in-situ monitoring of the waste feed consistency were focused beam reflectance measurement (FBRM), optical back-reflectance measurement (ORM), ultrasonic spectroscopy (USS), Lamb/Stoneley wave viscosity measurement, and vibration-based densitometers. Based on literature results and commercial options, the ultrasonic and vibration-based techniques showed the most promise for developing a technology that could be used for in-situ measurements within

---

[1] FIU understands the implementation plan as the use of an instrumented flow loop located above the tank. The instrumentation included Coriolis Meters, UDV and PE ultrasonic technology, and FBRM for particle characterization.

the aggressive environment of a HLW tank. Specifically, the vibration-based and USS systems can provide information on the density and concentrations of the mixed slurry. These techniques can be engineered for monitoring at various depths within the tank.

EXPERIMENTAL APPROACH

A test strategy was developed that could assess how a technology could handle the physical characteristics of the slurry media in which it would be deployed, before evaluating the technology readiness aspects of the system. The tests to perform would consist of a first phase that determines how accurate a technology can determine slurry characteristics, followed by a second phase – as necessary - that determines what factors and interactions most influence the measurement principle, as implemented in the technology. The first phase would act as a discrete, go/no-go stage to determine which the technologies could provide the most useful and accurate measurements for slurry characteristics, and how those measurements compare to laboratory-based measurements. The details of this test strategy are summarized below.

Operating Principles

In order to perform additional laboratory-scale qualification of the candidates, a review of the factors that could influence the technology performance was performed. Specifically, the changes in the physical, chemical and rheological properties of the target media that could influence the resulting measurement were investigated. For ultrasonic measurement systems within a suspension, it is critical to understand the media impact of the ultrasonic wave velocity, as well as the factors that influence attenuation of the pressure wave. From a phenomenon perspective [3] ultrasonic wave velocity changes within the media are directly related to changes in the effective bulk density ρ_{eff} and effective compressibility K_{eff} of the medium,

$$V = (\rho_{eff} K_{eff})^{-1/2}$$

where

$$\rho_{eff} = \varphi\rho_s + (1 - \varphi)\rho_l - 2(\rho_s - \rho_l)^2\varphi(1 - \varphi)Q/(Q^2 + U^2)$$

and

$$K_{eff} = \varphi K_s + (1 - \varphi)K_l$$

ρ and K denote the density and compressibility (subscripts s and l denote solid and liquid phases, respectively), φ denotes the volume fraction, Q and U are two values calculated utilizing density, fluid viscosity, angular frequency of ultrasound, and the mean particle size.

Ultrasonic attenuation α can be described by the simplified equation

$$\alpha = \varphi\bar{\sigma}$$

where φ denotes the volume fraction and $\bar{\sigma}$ denotes the total cross section for the scatterer(s). Assuming an average particle size smaller than the ultrasonic wavelength, the total cross section of the scatterer(s) would depend on ratio of particle size to ultrasonic wavelength. Clearly, velocity changes and attenuation of the ultrasonic signal within a suspension of solid particles in a liquid media are influenced by volume fraction of particles, fluid viscosity, particle size and shape, temperature and inter-particle forces. Both these equations are very strongly influenced by particle size, as well as volume concentration. If the particle size starts to get close to the ultrasonic wavelength, or the volume concentration exceeds 10%, the effects of multiple scattering can greatly influence ultrasonic measurement performance. In addition, the measurement of density of a media from a propagation ultrasonic wave is the results of the

reflection that occurs at the interface between the media and the transduction material. This reflection is the results of the impedance (Z) change between the materials. Utilizing the known impedance of the transduction material and the reflected wave characteristics, the impedance of the media under test is determined. This impedance can be coupled with the speed of sound (c) in the media to determine the density utilizing the following equation,

$$\rho = \frac{Z}{c}$$

There have been prior year efforts to develop an in-tank density meter utilizing the ultrasonic reflection principle (PNNL, University of Leeds, Otto-von-Guericke-University Magdeburg). But the effect of a broadband pulse, and resulting spectral response, has not been evaluated as a method to improve accuracy of the density measurement. In particular, this technology provides the attenuation spectral response, which can be utilized as an additional monitoring parameter for particle size distribution profile. This can be useful in addressing possible future waste acceptance criteria issues associated with variations in the PSD profile.

The specific system under evaluation is produced by Industrial Tomography Systems plc of Manchester, United Kingdom (UK). The system consists of an electronics module and an in-tank probe (See Figure 45 and Figure 46 below). The system is lowered into the test media, and allowed to measure echo attenuation, time-of-flight (TOF) and interface reflection. The system software (Figure 47) controls system referencing, data logging and troubleshooting. The software also includes several additional analysis components for estimating concentration and reviewing the attenuation spectral response.

Figure 45. USS System Control Module and In-tank probe

Figure 46. Close-up of probe sensing region.
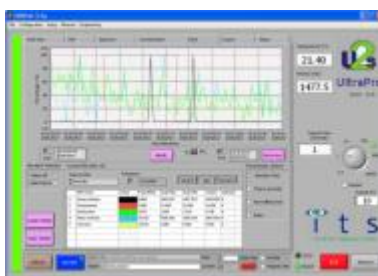
Figure 47. USS Software GUI.

Vibration/Coriolis Density Measurement

For a vibration measurement system, the calculation of density is based on the following simplified equation,

$$\rho = \frac{c}{4\pi^2 V} P^2 - \frac{M}{V}$$

where c is the spring constant of the system, V is the measurement volume, P is the natural period of oscillation, and M is the mass of the vibrating element. This equation assumes a uniform mass and impact force [4]. In reality, the effect of fluid viscosity can lead to a change in flow pattern based on the movement of the vibrating element. This flow pattern change can lead to different inertial forces being exerted on the elements, which can lead to different oscillation frequencies. Also, this will be dependent on the presence of particles in the liquid. Another potential influence is the possibility of deposits forming on the surface of the vibrating element, which can lead to measurement drift based on the change of mass and measurement volume. Any concentration differences within the suspension, trapped bubbles, or stray currents (due to jet flow) can influence the resulting measurement.

Based on the influencing factors on the measurement techniques, the phase I approach is to evaluate the accuracy in measurement, and at what point will volume fraction and the effective bulk density of the suspension influence the range and resolution. In particular, the tests will determine the accuracy of the USS technique in comparison to stable, repeatable techniques for density and concentration measurement using vibration and/or Coriolis force principles. In addition, the tests will determine technique behavior at the upper bounds of solids loading and carrier fluid density.

The two technologies under consideration are under different phases in development. The USS technology is a commercially available unit, but is available in an in-situ package suitable for laboratory applications. The Coriolis-based vibrating densitometers are commercially available units that are designed for a multitude of application environments. The USS maturity limited the current evaluation to verification of measurement capabilities, as well as repeatability of the measurements, within a controlled laboratory environment that did not expose the probe to the rigors of a HLW tank environment. The vibrating densitometer will allow a more real-world cold test to determine utilization under varying conditions. In order to perform a comparison of the technologies, the test regime focused on validating the accuracy and repeatability of the technologies with various slurry simulants at the same scale. FIU set up a single Coriolis meter (Endress-Hauser Promass 63F) arrangement to perform measurements on the simulated slurry under test. This technology was used as the "baseline", or reference, on which to gauge the performance and measurement accuracy of the USS.

Experimental Design

The experiments to be performed in the first phase of testing will consist of two scenarios that will be utilized to determine the capabilities of the USS in its current configuration. As a preliminary step, bench-top evaluations of the USS performance for various carrier fluid densities will be performed to determine the effect on the USS attenuation, ultrasonic group velocity and density measurement. Also, the first phase of testing will include testing in a meso-scale (10 gallon) slurry simulant to collect side-by-side measurements between both technologies under consideration. This included the development of simulant slurry consistent with the physical bounds for density and primary solids particle types encountered in the AY-102 HLW tank (See Table 4). This tank will be used as an initial staging tank for the WTP delivery, so simulants based on the current contents are used as a reference for evaluation of measurement accuracy that can be expected on the tank waste.

Table 4. Hanford Tank Waste Parameters/Ranges Varied for Simulant Slurries

Parameter	AY-102 Range	Test Range	Unit	Comments
Density (carrier fluid)	1 – 1.47	1- 1.30	g/cc	NaNO$_3$ mixture utilized to vary parameter
Density (solid)	2 – 10	2.25 – 8.00	g/cc	
Mean particle size	0.65 – 1000	1 - 100	um	
Volume UDS fraction	1 – 20	1 - 10	%	

The bench-top evaluations evaluated how the technology would perform when the carrier fluid density was the only changed physical factor. This change leads to resulting change in media bulk modulus, which is directly related to ultrasonic group velocity in the media by

$$C = \sqrt{\frac{1}{K\rho}}$$

The bench-top evaluations of concentration ladder looked to determine the relationship between solids loading and attenuation/velocity of the media. It was also used evaluate the concentration estimate provided by the software, which requires solid parameters (density, bulk modulus) to be provided before concentration can be calculated. As the relationship between ultrasonic group velocity and slurry concentrations is a quadratic equation, the software provides two estimates of the concentration.

The lab-scale evaluations provided side-by-side comparison of the bulk density measurements of both the USS and the Coriolis meter system within the same slurry simulant. In addition, this allows additional examination of how well both technologies can track the mixing plume as the mixing is started/stopped, and the resulting fluctuations in bulk density as the mixture becomes consistent.

Experimental Loop

The experimental loop (Figure 48 and Figure 49) consists of a mixing tank with three jets for agitation, and a single intake located near the fluid/air interface. The mixing process is driven by a 1HP centrifugal pump. The mixing vortex is controlled using a main gate valve and ball valves located on each jet. The simulated slurry temperature is controlled through the use of a pipe-in-pipe heat exchanger using chilled water as the thermal sink. In addition to this setup, an additional bench-top system is used for troubleshooting and small scale validation tests. The setup (Figure 50) utilizes a magnetic stirrer/heater plate to agitate the media and control the temperature.
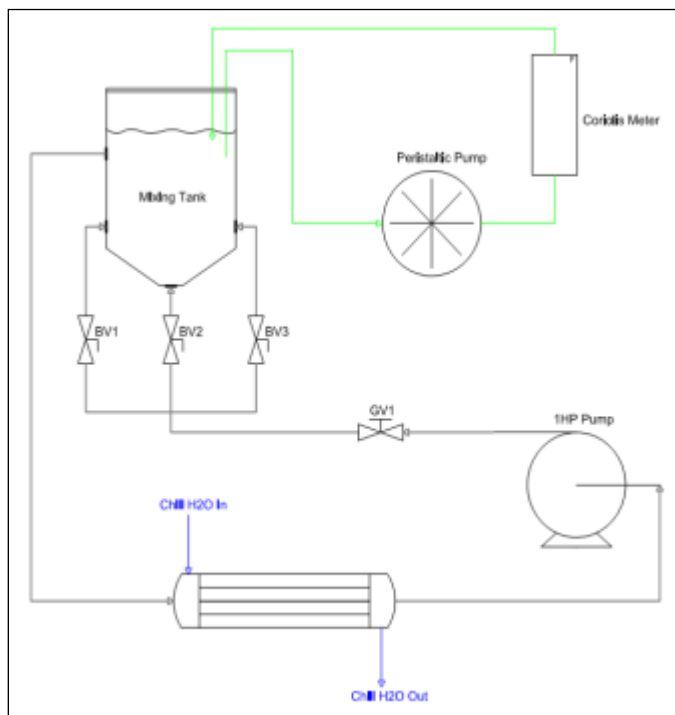
Figure 48. Mixing and sampling loop diagram.

Figure 49. Sampling loop at FIU. The sampling pump and Coriolis meter are visible in the center and top of the image.

Figure 50. Benchtop test setup. Preliminary solids loading tests and troubleshooting were performed in this setup.

Slurry Simulants

Based on the factors that influence the performance of the two candidate technologies, an experimental matrix has been prepared that will evaluate the density measurement accuracy with slurries of varying physical and rheological properties. The slurry simulants use materials based on the Waste Feed Small-Scale Mixing Demonstration (SSMD) Program's simulant selection report [5], which identified simulant materials, and their respective concentrations, to obtain simulant slurry with similar specific gravity and particle bounds as the waste found in AY-102, while being a simple non-cohesive simulant. The slurry simulants will consist primarily of a NaNO$_3$ or H$_2$O supernatant, with the addition of particles of varying specific gravity, mean size and distribution characteristics.

The carrier fluid for all slurries was either ultrapure reverse osmosis/de-ionized (RODI) water (< 0.2 um), or a solution of NaNO$_3$ and ultrapure RO/DI water prepared to adjust the density. Three different solids media were used for the slurries undissolved solids (UDS) content. Al(OH)$_3$ (processed by Huber Materials) was used to simulate the gibbsite found in the AY-102 tank; the tank contains as much as 53% by volume of this material. Zirconium oxide (processed by Fisher Scientific) was used to simulate the iron oxides found in the tank; they represent 40% by volume of waste. The zirconium oxide provides a similar density as the iron oxides. Stainless steel powder (manufactured by 3DS Systems) was used to simulate the larger bounding densities and particle sizes found within the tank. Site representatives recommended that the slurries not include some of the other solids used in the SSMD simulant (such as silicon carbide), as these represent a very small amount of the waste, and could lead to problems with mixing and damage to the mixing and sampling loop. As a base material for preliminary testing, AL(OH)$_3$ was selected for several reasons. With a mean particle size of 9 micron, and a density of 2.42, it was very easy to suspend and maintain a mixed slurry for some time after turning off the mixer. Also, the particle size was smaller than the wavelength of the USS pulse even at high frequencies, which ensured that visco-inertial/thermal absorption and scattering were the only mechanisms

for energy loss. A list of slurry simulants used is provided below. The slurries with the 'B' included in their ID were prepared and used for the bench-top tests to evaluate solids loading and USS performance.

Table 5. Slurries Prepared for Technology Assessment

Slurry ID	Mixture Description	Carrier Fluid (rho)	Al(OH)3 (kg)	ZrO2 (kg)	SS316 (kg)
T15W2	2% AL(OH)3 + RODI	H2O	2.175	-----	-----
T15W4	4% AL(OH)3 + RODI	H2O	4.44	-----	-----
T15W8	8% AL(OH)3 + RODI	H2O	9.27	-----	-----
T15W10	10% AL(OH)3 + RODI	H2O	11.845	-----	-----
T15W14	14% AL(OH)3 + RODI	H2O	17.355	-----	-----
T15W20	20% AL(OH)3 + RODI	H2O	26.655	-----	-----
T15SNBase	Base NaNO3 Solution	NaNO3 + H2O	-----	-----	-----
T15SN2B	2% AL(OH)3 + NaNO3 Solution	NaNO3 + H2O	2.175	-----	-----
T15SN4B	4% AL(OH)3 + NaNO3 Solution	NaNO3 + H2O	4.44	-----	-----
T15SN8B	8% AL(OH)3 + NaNO3 Solution	NaNO3 + H2O	9.27	-----	-----
T15SN10B	10% AL(OH)3 + NaNO3 Solution	NaNO3 + H2O	11.845	-----	-----
T15SNBase2	Base #2 NaNO3 Solution	NaNO3 + H2O	-----	-----	-----
T15SN2B2	2% AL(OH)3 + #2 NaNO3 Solution	NaNO3 + H2O	2.175	-----	-----
T15SN4B2	4% AL(OH)3 + #2 NaNO3 Solution	NaNO3 + H2O	4.44	-----	-----
T15SN8B2	8% AL(OH)3 + #2 NaNO3 Solution	NaNO3 + H2O	9.27	-----	-----
T15SN10B2	10% AL(OH)3 + #2 NaNO3 Solution	NaNO3 + H2O	11.845	-----	-----
T15WBase	RODI Base	H2O	-----	-----	-----
T15W2T2	2% AL(OH)3 + RODI	H2O	2.175	-----	-----
T15W4T2	4% AL(OH)3 + RODI	H2O	4.44	-----	-----
T15W8T2	8% AL(OH)3 + RODI	H2O	9.27	-----	-----
T15W10T2	10% AL(OH)3 + RODI	H2O	11.845	-----	-----
T15W14T2	14% AL(OH)3 + RODI	H2O	17.355	-----	-----
T15W20T2	20% AL(OH)3 + RODI	H2O	26.655	-----	-----
T15SNBase3	Base #3 NaNO3 Solution	NaNO3 + H2O	-----	-----	-----
T15SN2B3	2% AL(OH)3 + #3 NaNO3 Solution	NaNO3 + H2O	2.175	-----	-----
T15SN4B3	4% AL(OH)3 + #3 NaNO3 Solution	NaNO3 + H2O	4.44	-----	-----
T15SN8B3	8% AL(OH)3 + #3 NaNO3 Solution	NaNO3 + H2O	9.27	-----	-----
T15SN10B3	10% AL(OH)3 + #3 NaNO3 Solution	NaNO3 + H2O	11.845	-----	-----
T15WCMPLXBase	RODI Base	H2O	-----	-----	-----
T15W2CMPLX	2% MIXTURE + RODI	H2O	1.13	1.9	0.79
T15W4CMPLX	4% MIXTURE + RODI	H2O	2.31	3.875	1.615
T15W8CMPLX	8% MIXTURE + RODI	H2O	4.82	8.085	3.365
T15W10CMPLX	10% MIXTURE + RODI	H2O	6.16	10.33	4.305
T15SNBase4	Base #4 NaNO3 Solution	NaNO3 + H2O	-----	-----	-----
T15SN2CMPLXBase4	2% MIXTURE + #4 NaNO3 Solution	NaNO3 + H2O	1.13	1.9	0.79
T15SN4CMPLXBase4	4% MIXTURE + #4 NaNO3 Solution	NaNO3 + H2O	2.31	3.875	1.615
T15SN8CMPLXBase4	8% MIXTURE + #4 NaNO3 Solution	NaNO3 + H2O	4.82	8.085	3.365
T15SN10CMPLXBase4	10% MIXTURE + #4 NaNO3 Solution	NaNO3 + H2O	6.16	10.33	4.305

Technical Limitations & Assumptions

The tests performed were limited in scope due to technical and/or operational limitations. The limitations were:

1.   Tests maintained the temperature at approximately 20 degree Celsius. No tests were performed outside this temperature value.

2.   The stainless steel powder particle size was limited to 100 um maximum.

3.   The effect of solid particle shape was not evaluated in this phase.

4.   No modifications were made to the USS system to improve signal strength/return echo, although the system has the capability for path length adjustment.

5.   Due to a hardware failure some tests were performed with one USS, while another round of tests were performed with another system. It was assumed that the same performance would be observed.

RESULTS & DISCUSSION

Due to several hardware and software issues related to the USS, many of the required experiments were completed over a period of 6 months. Experiments performed through August included one set of hardware, and those run in October utilized another hardware set. The hardware changes led to some unexpected spectral response profiles. These are addressed in the following sections.

USS System and Installation Setup

The USS system was set up by Industrial Tomography Systems plc (the vendor) during April of 2011. The System controller connects to the host computer using the USB interface for serial communication. The probe connects directly to the controller through a custom quick-coupling connector. The system runs off 120 VAC electrical supply, and provides built-in noise filtering and surge protection. The probe used in these experiments came with a 1 m cable that is permanently affixed to the probe; the company representative stated that this could be modified to provide longer cabling and a quick connection option at the probe. The software platform was developed using Labview®, so the Labview runtime engine is needed to install and run the system (comes packaged with the system software). The necessary drivers for the controller hardware cards (DAQ, function generator) were installed with separate installation packages prior to the USS software. During the initial testing period, the system software was updated by the vendor to add the capability for density measurement, and to address false triggering issues. These updates caused issues with the system performance, and required that the vendor return to FIU to correct the problems.
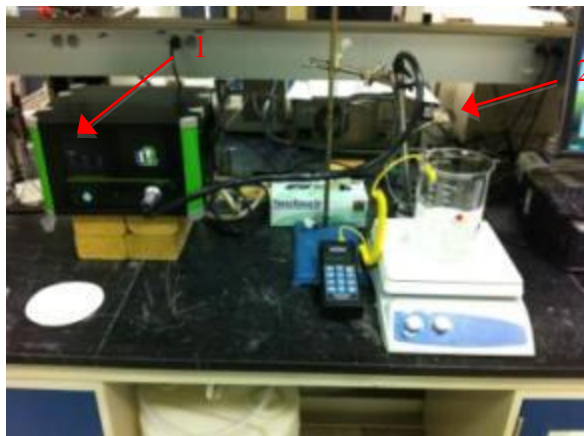
Figure 51. USS System installed in laboratory. The hardware components are shown: (1) controller, (2) in-tank probe. The interface cable between probe and controller was 1 meter long for this test.

The probe included various spacers to adjust the separation between the excitation element and the reflector plate. The rationale behind selection and installation of a spacer over another length is driven by the solids loading and viscosity of the media under test. If significant attenuation occurs utilizing a spacer, the separation distance can be decreased to improve echo strength. For all preliminary tests, a 40 mm spacer (Figure 52) was recommended by the company representative. After several troubleshooting issues to address several configuration problems, the spacers were replaced by 36 mm versions (Figure 53); the issues will be discussed below.

Figure 52. 40 mm spacers provided a 7.83 mm propagation path for the ultrasonic pulse.

Figure 53. 36 mm spacers reduced the propagation path to 3.83 mm, allowing for higher solids concentration in the media under test.

Speed of Sound Verification

In order to validate the performance of the USS system, several sodium nitrate ($NaNO_3$) solutions were prepared and used to verify that the USS measurement of acoustic/ultrasonic velocity matches literature measured values. A solution was prepared using industrial sodium nitrate pellets. The liquid solvent was RODI Water. Three solutions were prepared with varying $NaNO_3$ concentrations: 3.6 Mol/kg, 5.0 Mol/kg, and 10.8 Mol/kg. The solute was added to the solvent while agitated with a magnetic stirrer, and allowed to completely dissolve for 8 hrs. The final solution was filtered to remove any residual solids. Data was collected for 30 minutes per test. In addition, attenuation was observed to ensure that no loss of signal/scattering occurred during tests. The solution results were compared to results with RO DI water.

Results & Literature Comparison

The acoustic velocity data collected for the $NaNO_3$ solutions were used to determine a population mean and standard deviation as a function of pulse frequency. These values were compared to a 1997 Journal of Chemical Society article by Rohman et al that utilized a multifrequency ultrasonic Interferometer at 2 MHz to measure the acoustic velocity of sodium nitrate as a function of molar concentration. The figures below show the results. There is agreement between the measured speed of sound with the USS and the least square fitted curves determined by the data collected by Rohman et al. The outlier points are those at the higher frequency limits of the technology, where energy loss is significant during pulse generation and propagation to make out an appropriate return echo.
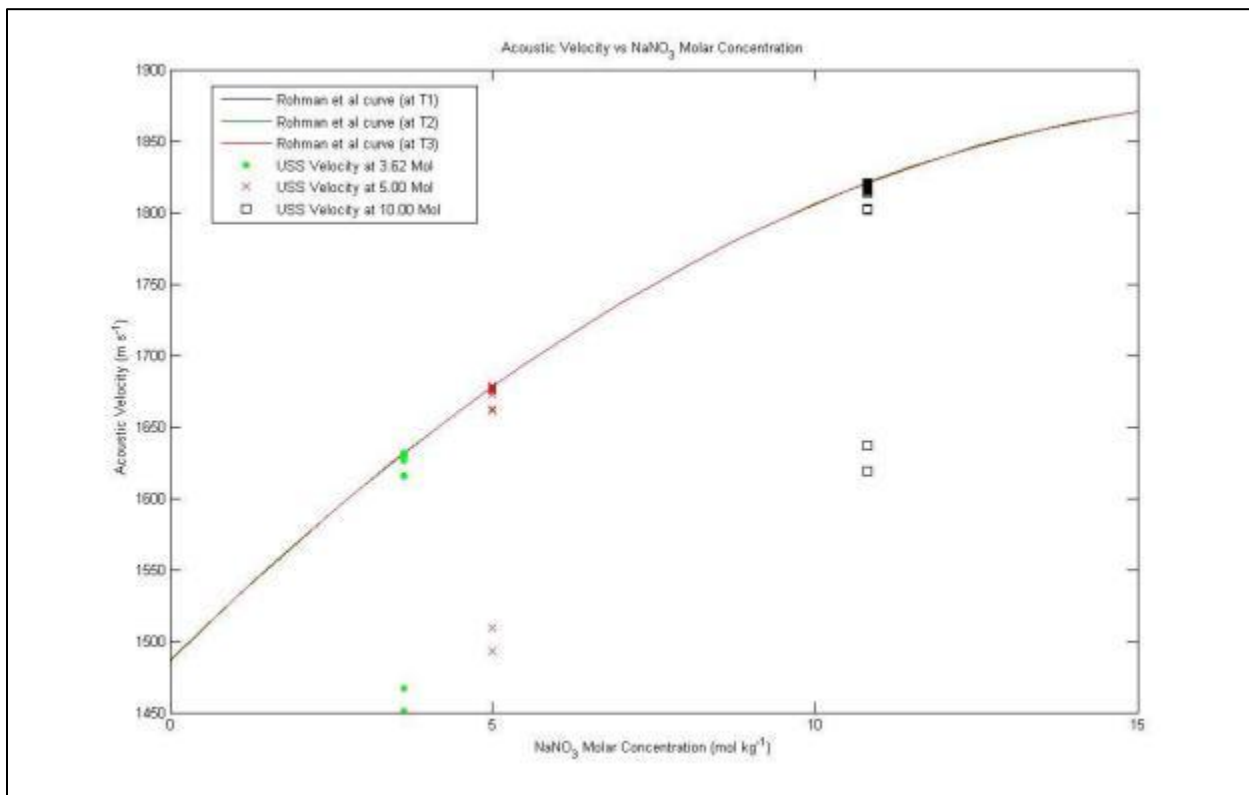
Figure 54. Speed of Sound in NaNO3 comparison between literature and USS measurement.

The individual average velocities per pulse frequency are provided in the Figure 55, Figure 56 and Figure 57 below. It can be seen that the values are within the bounds of the acoustic velocity estimation as performed by Rohman et al for frequencies up to approximately 25 MHz. Higher frequency values display a steep drop-off of the acoustic velocity, indicating that insufficient energy is available at that frequency to estimate the velocity with any accuracy. These measurements confirmed that the USS was accurately measuring the acoustic velocity at the reference temperature.
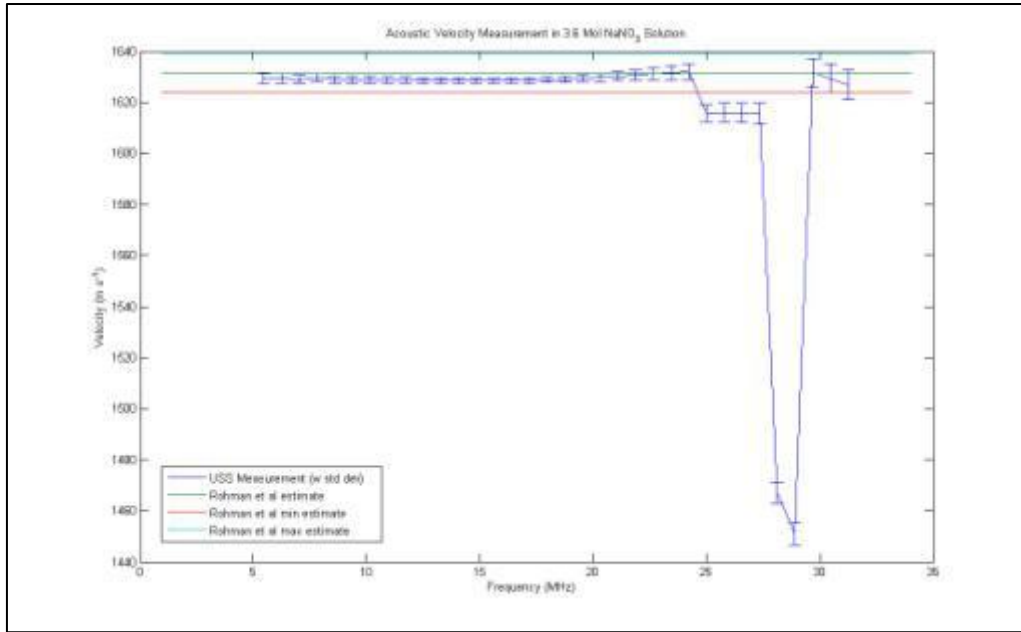
Figure 55. USS spectral response for speed of sound in 3.6 Mol solution.
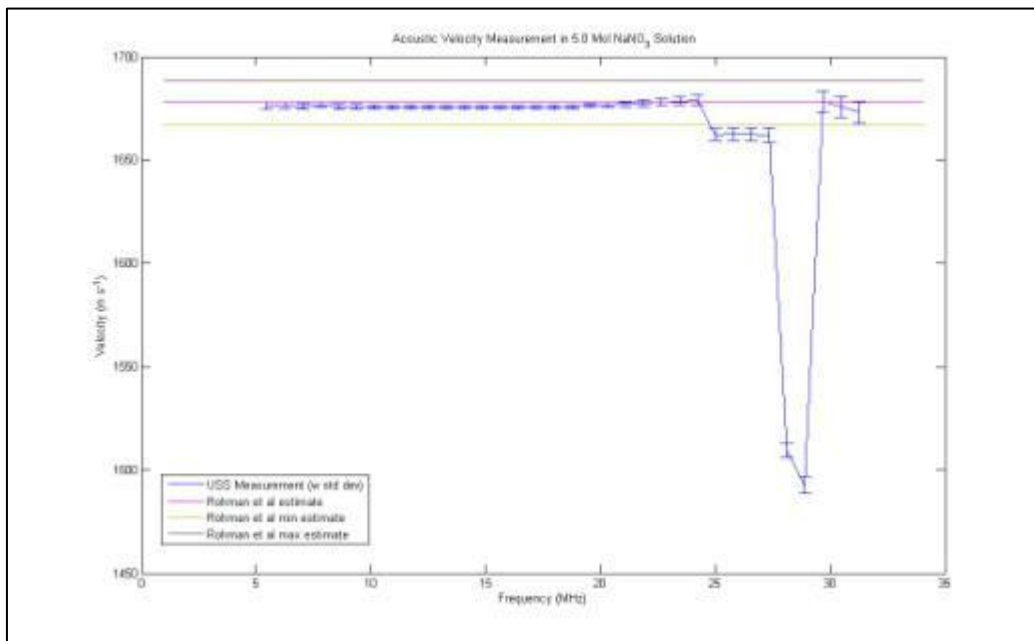
Figure 56. USS spectral response for speed of sound in 5.0 Mol solution.
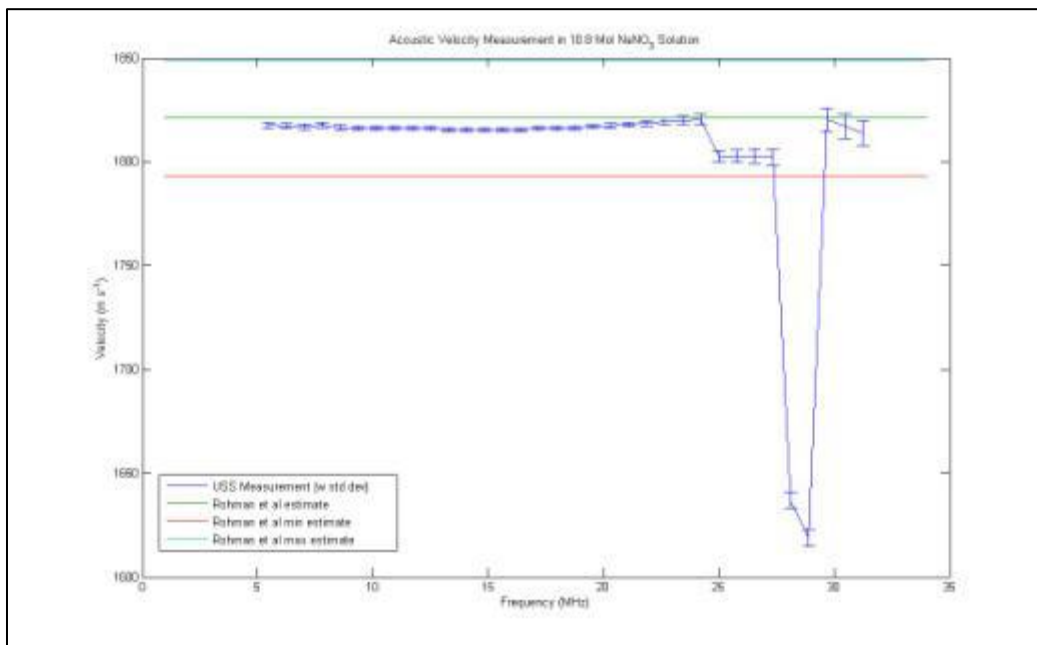
Figure 57. USS spectral response for speed of sound in 10.8 Mol solution.

Preliminary Tests

Several experiments were performed with suspensions of varying volume concentrations of AL(OH)$_3$. The results, provided in Table 6, show the effect of increasing solids loading on the attenuation and the ultrasonic group velocity. In particular, the solids loading between $1 - 10\%$ shows a linear behavior, with a dramatic increase in attenuation and ultrasonic group velocity, as that ultrasonic wave is scattered by the solid particles, and the energy is absorbed by oscillations of the solid particles and thermal gradients created at the particle surface.

Table 6. Preliminary Results for Various Test Runs

Mixture description	Temp (Celsius)	Density (g/cc)	Mean Attenuation at 10.2 MHz (db/cm)	Ultrasonic group velocity (m/s)
RO/DI water (standing)	21.1	0.9979	0.189	1481.95
RO/DI Water (mixing)	21.2	0.9979	0.192	1463.91
0.33M NaNO$_3$ + 5.55M H$_2$O	20.6	1.172	0.103	1631.16
0.50M NaNO$_3$ + 5.55M H$_2$O	20.3	1.226	0.073	1676.80
1.0M NaNO$_3$ + 5.55M H$_2$O	20.4	1.389	0.07	1818.29
T15W0f27B	21.4	---	0.745	1496.43
T15W0f55B	21.1	---	2.35	1473.8
T15W1B	20.6	1.0091	1.058	1473.187
T15W1f11B	21.3	---	1.985	1490.54
T15W2B	21.1	1.0295	2.032	1473.897

T15W2f30B	21.4	---	2.421	1480.64
T15W4B	21.2	1.0655	4.480	1473.397
T15W4f80B	19.6	---	6.369	1484.78
T15W8B	22.0	1.1181	10.553	1833.225
T15W11B	19.8	---	11.077	1829.88
T15W16B	21.4	1.2279	10.550	1840.933
T15W32B	22.2	1.4125	11.345	1840.893

It was expected that the velocity would continue to rise, as the bulk compressibility and density of the suspension continues to increase with increased solids loading. After a review of the data at the higher solids loading, it was determined that a change of the spacers was required, as the hardware was locking onto a different echo across the entire bandwidth of the pulses. This is why the resulting profile at higher solids loading shows a different profile than expected (Figure 58).
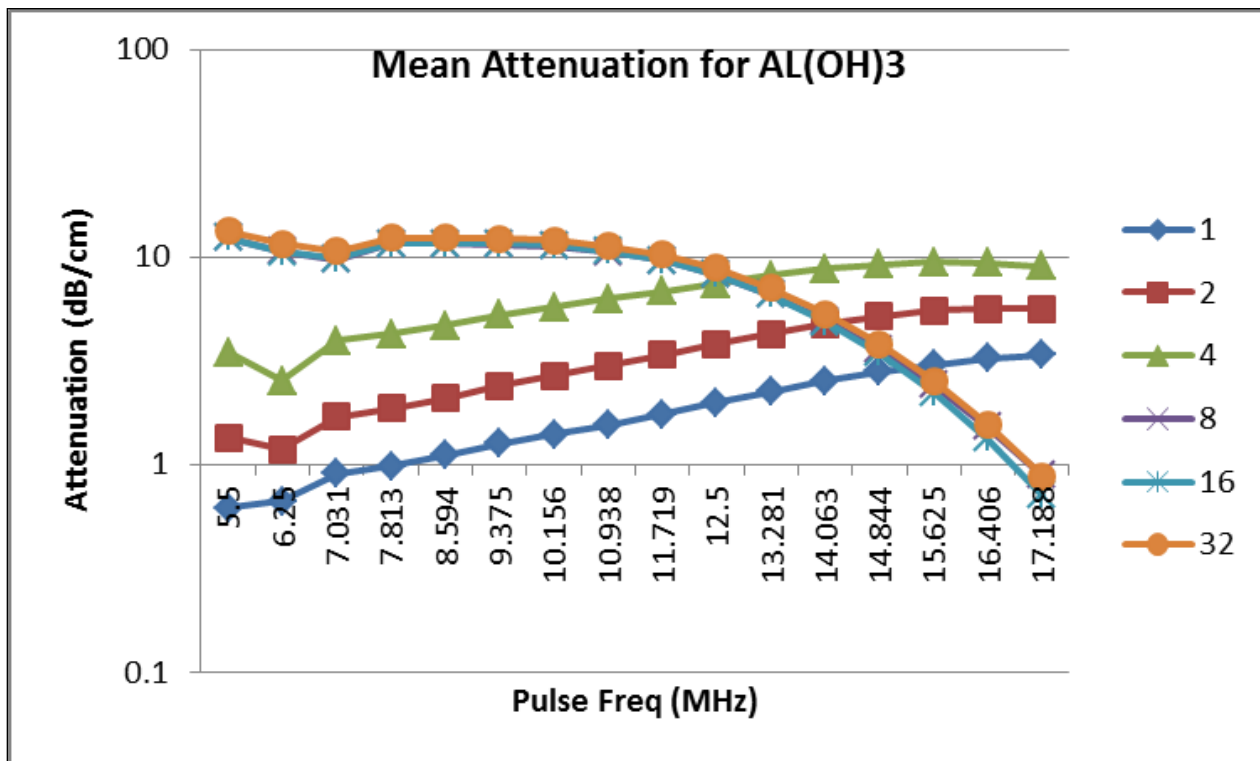
Figure 58. Attenuation versus pulse frequency for various AL(OH)$_3$ concentrations.

One interesting point is to select one pulse frequency in this linear range, and look at the profile as a function of bulk density (Figure 59). The profile is linear until a certain solids-loading is reached. At this point, the effects of multiple scattering and inter-particle interaction reach a maxima in terms of attenuating the pulse. In fact, the behavior leads to the conclusion that at higher solids loading (assuming constant path length), the system would continue to provide a near-constant attenuation value at the lower frequency ranges. This behavior would change when the particle size is similar or larger than the ultrasonic pulse wavelength, as would be the case

when the particle size is at the higher end of the AY-102 range (1000 um). This would lead to a very small echo.
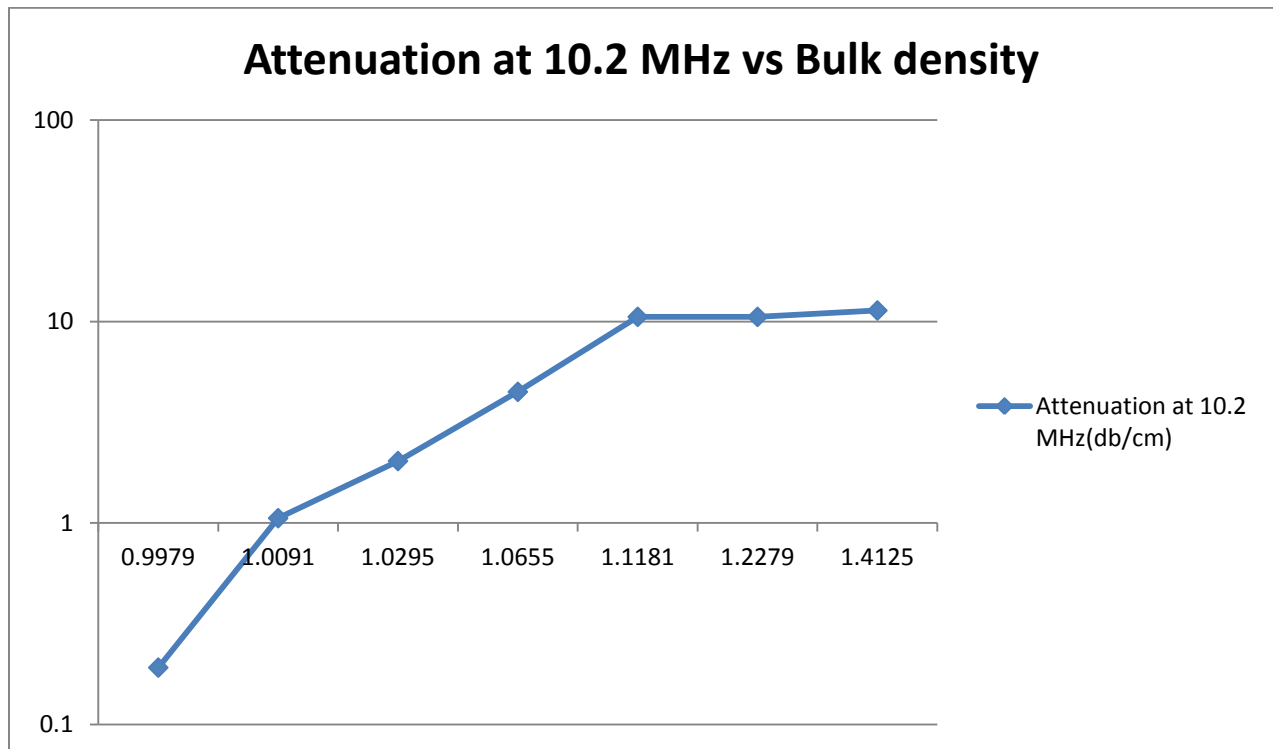
Figure 59. Attenuation profile at 10MHz pulse for varying bulk density

An investigation on the effects of ultrasonic group velocity on a solids-loaded suspension, versus a solution of similar density provides insight into the ultrasonic wave/particle interaction and effect on bulk modulus. As shown in the graph below (Figure 60), the velocity behaves in a non-linear with increased solids loading, while the change is linear with a pure liquid media. Both behaviors are in agreement with literature on the group velocity with density changes [3], although the literature suggests that the velocity will continue to rise with increasing solids loading. This discrepancy will continue to be evaluated with the testing remaining.
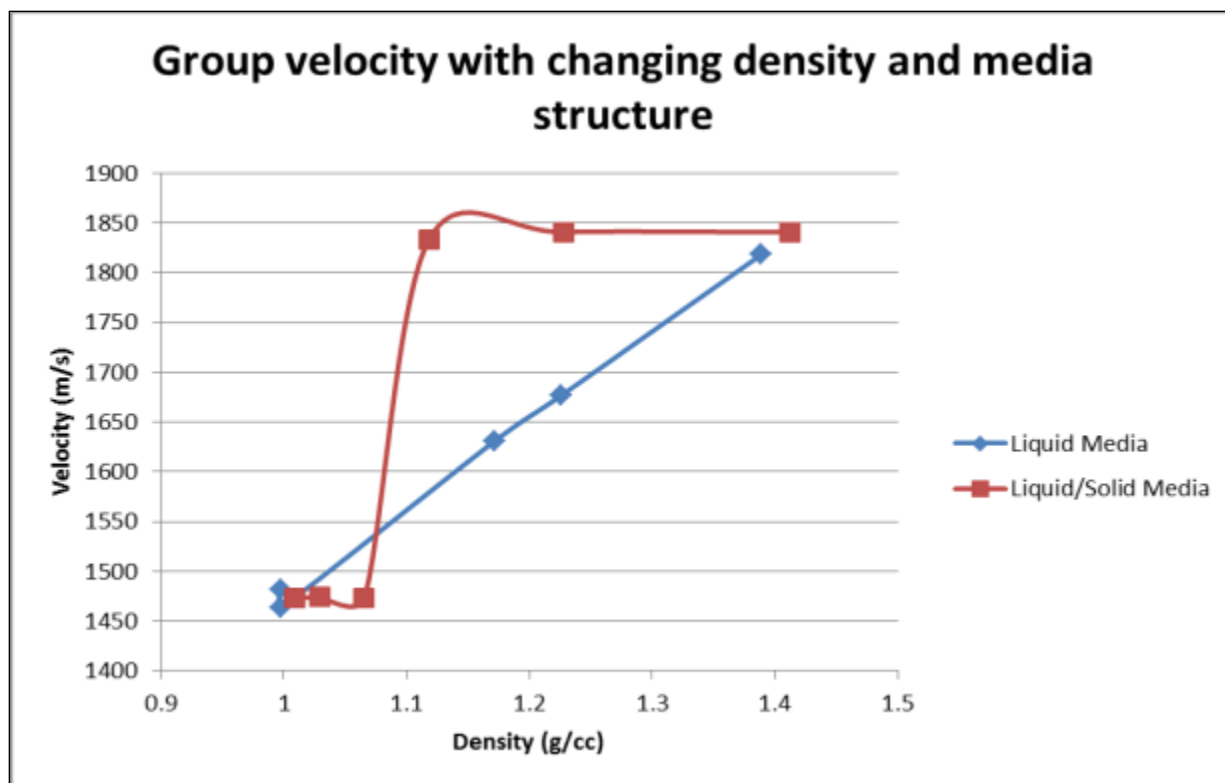
Figure 60. Relationship between liquid solution and solid/liquid suspension densities and velocity.

Bulk Density Measurement

Overall results show that most suspensions have matching density values to the Coriolis measurement near the resonant frequency of the transducer element (10 MHz). Outside of that frequency, there are large deviations from mean as the frequency spreads from a minimum. In addition, the summary statistics show increasing standard deviations from the minimum to the outer extremes of the spectral response (Figure 61) for most trials. Most mixture have two USS frequencies that match the Coriolis meter frequency. Mixtures and resulting Coriolis meter measurement and USS measurement (and frequency at which it occurred) are shown in Table 7 below. All the spectral responses and the summary statistics for the trials are located in appendices C and D, respectively.

Table 7. Density Results for Tested Mixtures

"AL(OH)3" refers to base mix, while "MIXTURE" refers to complex mix

Mixture Description	CM density (mean)	USS density #1 (g/cc)	USS #1 Freq (MHz)	USS density #2 (g/cc)	USS #2 Freq (MHz)
2% AL(OH)3 + RODI	1.0293	1.0333	25.5	1.0196	25.9
4% AL(OH)3 + RODI	1.0627	1.0622	10.3	1.0628	12.7
8% AL(OH)3 + RODI	1.1254	1.1264	13.7	1.1274	15.6
10% AL(OH)3 + RODI	1.1568	1.1554	13.7	1.1678	22.8
14% AL(OH)3 + RODI	1.2184	1.2141	13.3	1.2111	23
20% AL(OH)3 + RODI	1.3069	1.3024	22	1.3013	25.1
Base NaNO3 Solution	1.2952				
2% AL(OH)3 + NaNO3 Solution	1.3200				
4% AL(OH)3 + NaNO3 Solution	1.3447				
8% AL(OH)3 + NaNO3 Solution	1.3920				
10% AL(OH)3 + NaNO3 Solution	1.4167				
Base #2 NaNO3 Solution	1.1710				
2% AL(OH)3 + #2 NaNO3 Solution	1.1975				
4% AL(OH)3 + #2 NaNO3 Solution	1.2240				
8% AL(OH)3 + #2 NaNO3 Solution	1.2728				
10% AL(OH)3 + #2 NaNO3 Solution	1.2994				
RODI Base	0.9967	1.0109	7.8125	0.9849	15.0391
2% AL(OH)3 + RODI	1.0282	1.0331	10.7422	1.0314	16.6016
4% AL(OH)3 + RODI	1.0614	1.0625	11.5234	1.0683	17.5781
8% AL(OH)3 + RODI	1.1245	1.1270	9.375	1.126	16.6016
10% AL(OH)3 + RODI	1.1560	1.1556	9.1797	1.154	16.6016
14% AL(OH)3 + RODI	1.2142	1.2297	8.3984	1.2206	16.6016
20% AL(OH)3 + RODI	1.3096	1.3295	7.0313	1.2937	16.0156
Base #3 NaNO3 Solution	1.1723	1.1731	8.7719	1.1749	14.0351
2% AL(OH)3 + #3 NaNO3 Solution	1.1991	1.1975	6.0429	1.1994	14.2300
4% AL(OH)3 + #3 NaNO3 Solution	1.2183	1.2395	10.7213	1.2394	10.9162
8% AL(OH)3 + #3 NaNO3 Solution	1.2814	1.2829	10.3314	1.2804	15.2047
10% AL(OH)3 + #3 NaNO3 Solution	1.3125	1.3110	10.3314	1.3119	16.3743
RODI Base	0.9988	0.9951	9.5517	1.002	13.2554
2% MIXTURE + RODI	1.0564	1.0714	9.1618	1.0584	13.8402
4% MIXTURE + RODI	1.1191	1.1016	9.1618	1.1069	14.2300
8% MIXTURE + RODI	1.2482	1.2489	8.1871	1.2592	15.3996
10% MIXTURE + RODI	1.3257	1.3372	6.8226	1.3231	17.7388
Base #4 NaNO3 Solution	1.1649	1.1532	9.1618	1.1653	14.6199
2% MIXTURE + #4 NaNO3 Solution	1.2218	1.2346	9.1618	1.2219	14.6199
4% MIXTURE + #4 NaNO3 Solution	1.2819	1.275	9.1618	1.2901	14.8148
8% MIXTURE + #4 NaNO3 Solution	1.3244	1.3054	9.5517	1.312	14.6199
10% MIXTURE + #4 NaNO3 Solution	1.4653	1.4583	8.9669	1.4626	15.5945
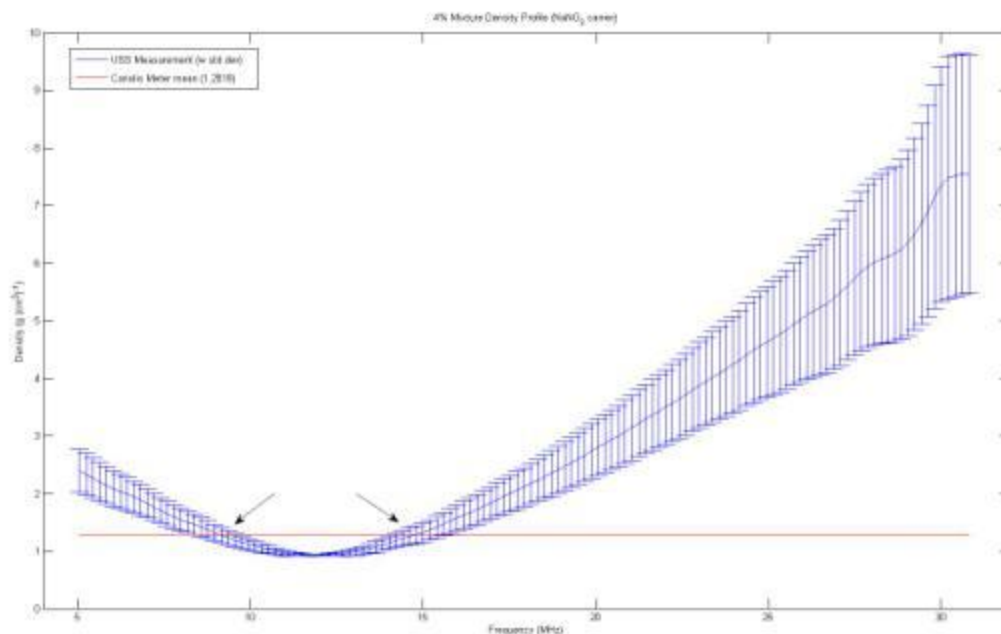
Figure 61. Spectral response for 4% solids mixture of NaNO$_3$/complex.

Normalized Density Profiles (All Suspensions)

In order to evaluate all the suspensions together, the data was normalized; normalized in this case means that the each frequency-dependent mean value of the USS spectral profile was divided by the reference Coriolis meter mean value. This would provide a matching value at 1.0. As the figure below shows, most mixtures show very similar response, with a minimum value occurring around the 10-15 MHz range. Most responses have two frequency values at which the density match occurs. Figure 62 shows the normalized profiles for the suspensions tested.
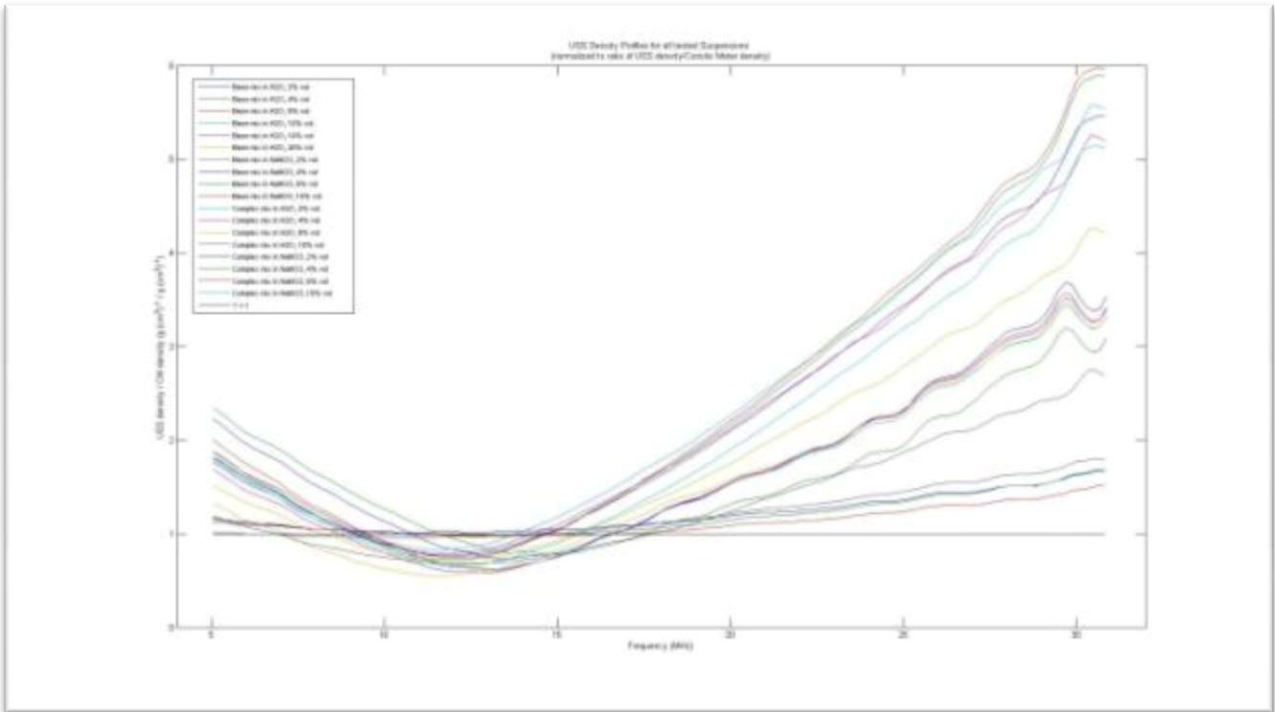
Figure 62. Normalized density profiles for all suspensions.

Density profile for Water-based Suspensions

The density profile was suspension with RO/DI water as the carrier fluid were collected up to 20% by volume for the base mix, and up to 10% for the complex mix. The RO/DI-based suspensions showed a broad range of matching frequencies for the density value. Results for RO/DI water based suspensions are shown in Figure 63 below.
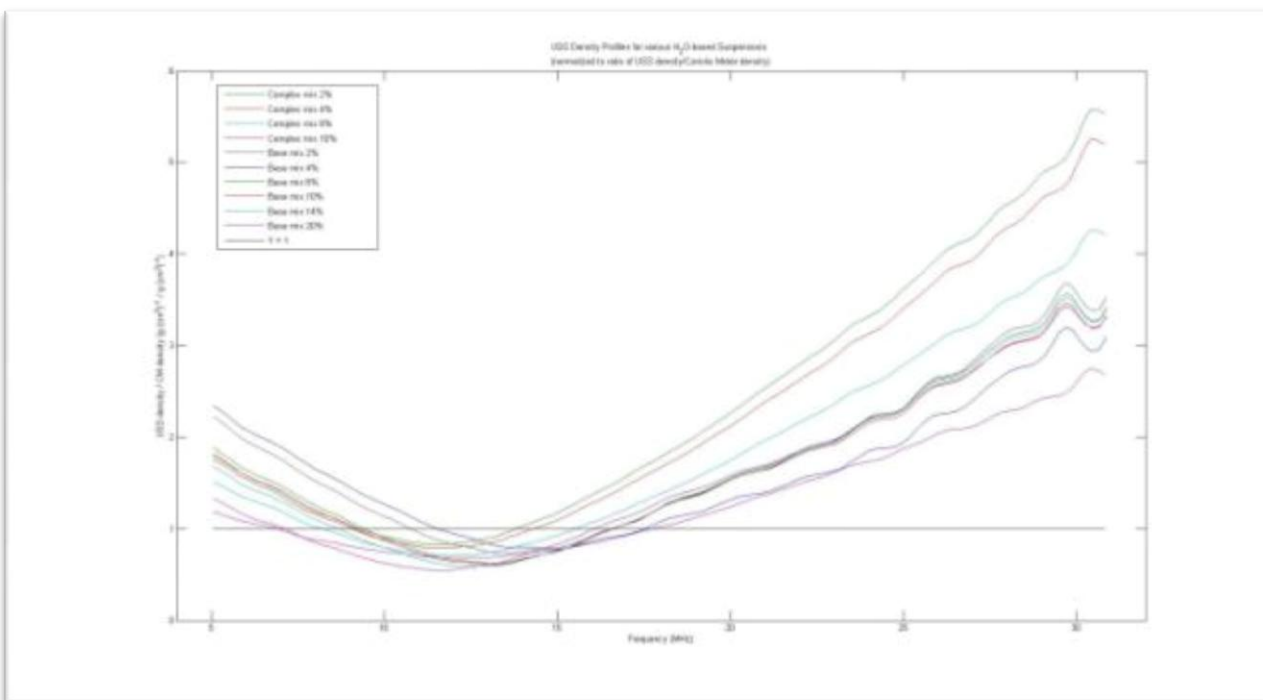
Figure 63. Density profile for RO/DI Water-based suspensions.

Density profile for NaNO₃-based suspensions

The density profiles for NaNO$_3$-based suspensions were collected up to 10% for both Base and Complex mix suspensions. The cross-over frequency occurs in a very narrow band for the complex suspensions, while a very flat response is observed for the Base material. During the testing, it was observed that the return echo was lost during the Base and Complex mix at 4% by volume, so there is some uncertainty in the measured values above that solid load volume. The results for NaNO$_3$-based suspensions is shown in Figure 64 below.
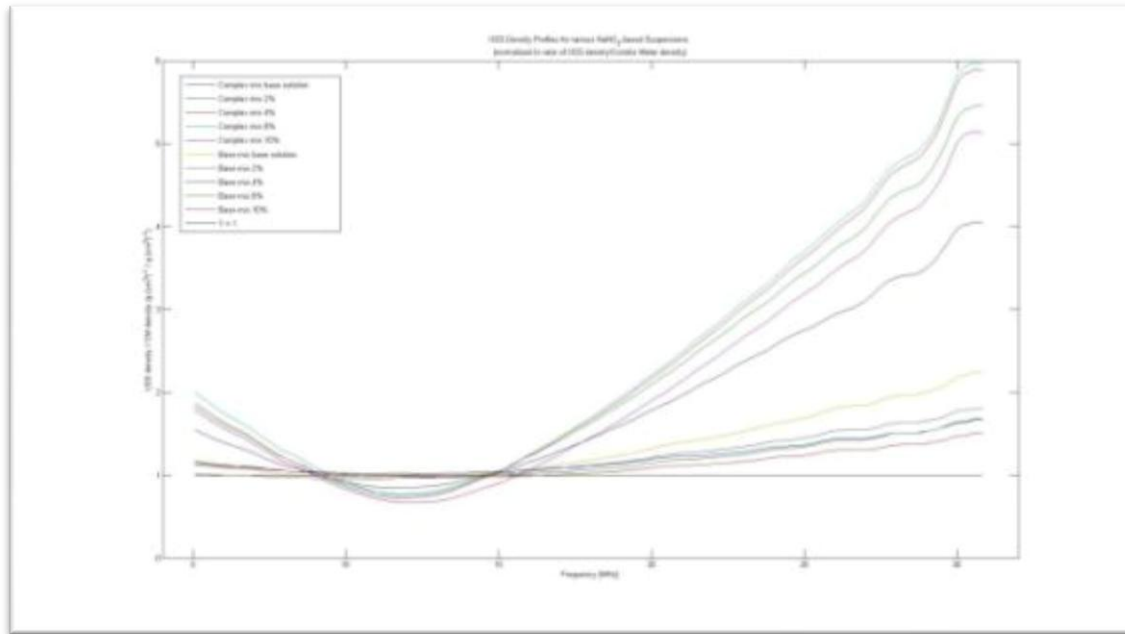
Figure 64. Density Profile for NaNO3-based suspensions.

Attenuation Data

An additional analysis performed on the data collected was the attenuation spectral profile for the various suspensions utilized. The attenuation spectral data was expected to show the relationship between the particle size distribution of the suspension and the resulting attenuation profile. Summary statistics are calculated for each frequency, and the results plotted as a function of carrier fluid. The spectral results are shown in Figure 65 and Figure 66.
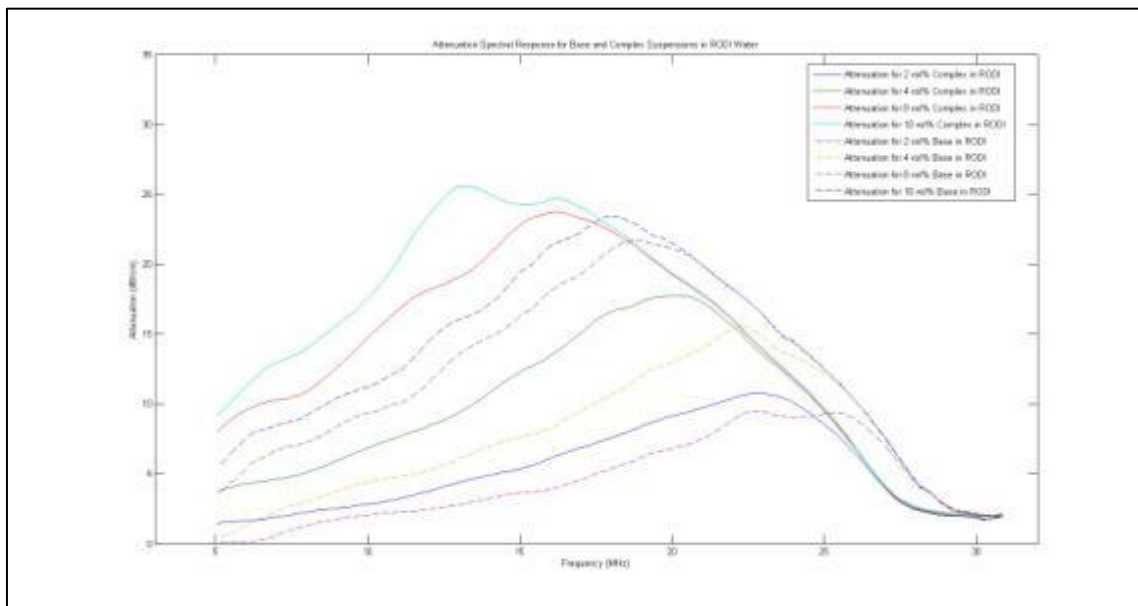
Figure 65. Attenuation data for Base mixture in RODI and NaNO₃.

The transition from RODI carrier fluid to $NaNO_3$-based solution shows a different spectral response, with larger attenuation at the lower frequency range. There is also significant attenuation occurring, even at the smallest solids load. This verified the observation during the trials that, although the system seemed to have better echo when the $NaNO_3$ solution did not have UDS, even a small amount of suspended solids was sufficient to cause a substantial amount of echo energy loss.
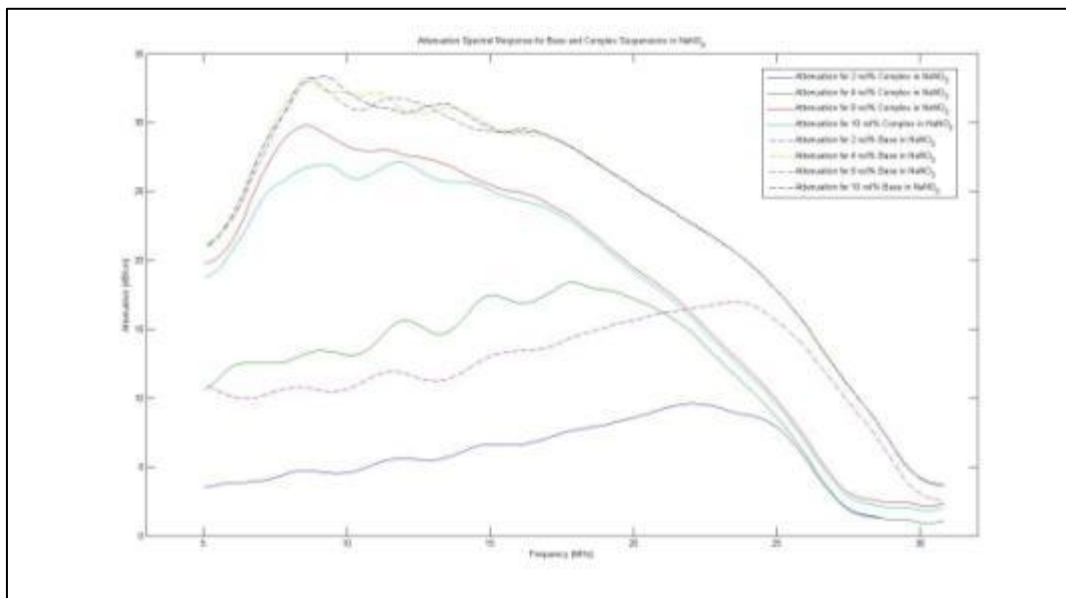
Figure 66. Attenuation data for complex mixtures in RODI and $NaNO_3$.

Error Detection/ Time-based trends

As several tests were performed on a single day, with the USS system left running throughout, and analysis was performed on test that occurred on the same day to see if there were any time-based trends of the data as testing progressed. As Figure 67 and Figure 68 below show, the data does not follow any particular trend; in fact, the data does not follow the expected increase in measured density as the solids load was increased throughout the day. In addition, data for each trial was graphed to detect any major variations in the trend that could indicate an issue with deviation, and/or spikes that could cause a problem for final mean value. One example of those graphs is shown in Figure 69. The trends show variations around a base value, with frequencies that were not near the minimum exhibiting larger variations. These results were verified with an estimation of the standard deviation for each trial, which show a small deviation near the minimum, and very large deviations at the extremes of the spectral response (located in Appendix D).
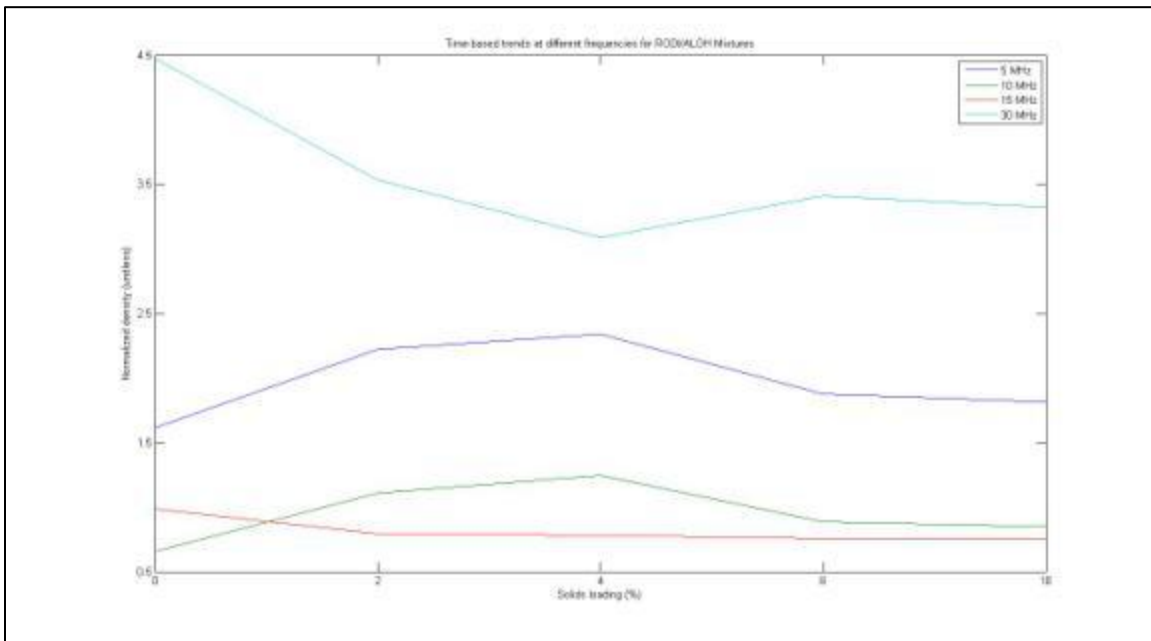
Figure 67. Time-based trend (by solids loading) of the data coollected during the RODI/ALOH mixture trials.
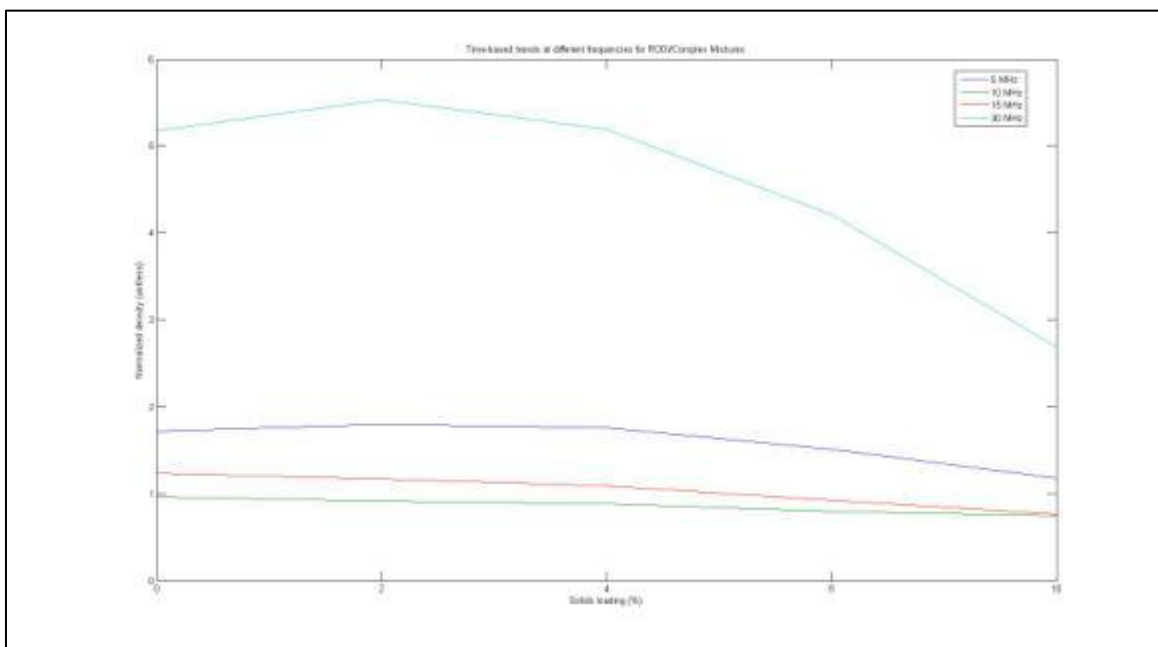
Figure 68. Time-based trend (by solids loading) of the data coollected during the RODI/Complex mixture trials.
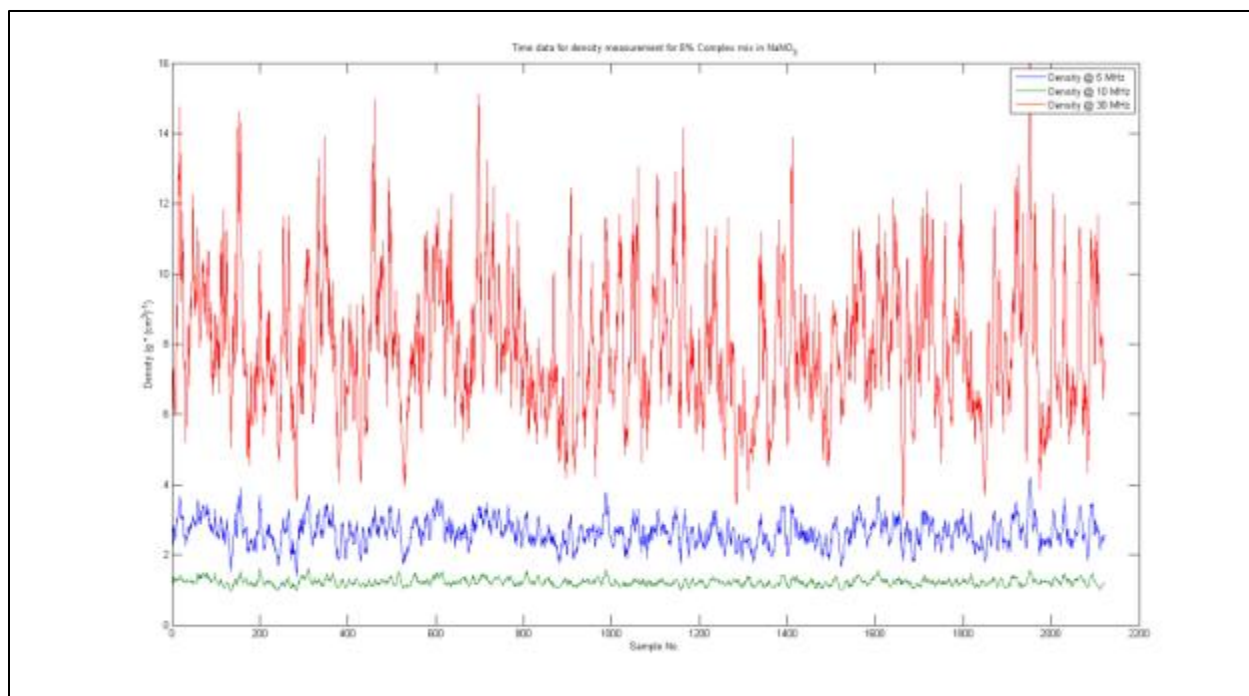
Figure 69. Trend of density measurement at different frequency values for a NaNO$_3$/Complex mixture at 8% solids load.

Configuration and Software Issues

The first phase of the USS system testing was completed in October of 2011. The system operation and tests dealt with several software/configuration issues that required the vendor to provide 4 different software versions to address system crashes. Also, the software in its original incarnation did not provide reflectance measurement, a component necessary to extract density measurements from the system. In this configuration, the software could only provide attenuation and velocity, and could calculate UDS concentration for single solid mixtures (solid density, and speed of sound for material required).

Initially, software installation encountered several issues when attempting it on the Windows® 7 operating system. After repeated attempts failed to provide communication between the controller and the software interface, a computer running Windows® XP was utilized, and installation was completed successfully. The software issues continued to hamper experimental runs, as the software would stop acquisition and continue to write reference values to data files. An additional software issue had to do with false triggers sent to the hardware controller from the software. This lead to large outlier measurements in the data; there was no discernable pattern to their location in the data file, and did not occur at the same time stamp. Additional issues included cabling issue with the second unit that allowed for large fluctuations in temperature measurement over several seconds. This issue occurred with the second unit tested, and continued throughout all the tests performed. The final issue related to hardware occurred at the completion of testing with the first unit. The system would not capture any return echoes, even when cleaned and submerged in water, with adjustments to the reflector plate. Density profile changes first transducer/last transducer

Due to a hardware issue, the USS was changed during testing. The resulting data from one system to another shows a noticeable difference in response (See Figure 70 below). A request for clarification on any hardware differences between systems was made to the vendor.
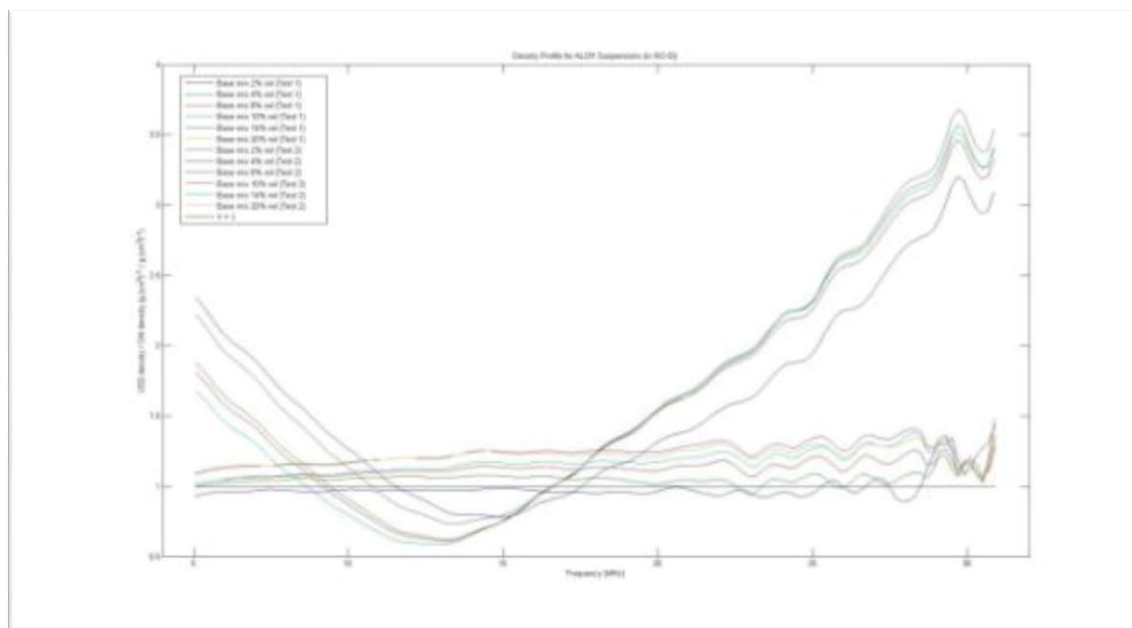
Figure 70. flat profiles were obtained utilizing the first USS.

Configuration and Software Issues

Based on the inconclusive results of testing, the vendor will re-analyze the data collected to determine what variations caused the two systems to provide difference spectral profiles. Also, additional bench-scale tests will be performed at ITS facilities in the coming months on a USS system with a larger transducer. These tests will mimic those performed at FIU in an attempt to address the inconsistent results from the different transducers. Also, these tests will provide Hanford with additional information to determine if further development and testing into the technology is warranted.

CONCLUSIONS

The USS system was capable of measuring the suspension density, although the measured frequency was not consistent throughout all testing. Several measurements were made around the resonant frequency of the system, but these frequencies still varied considerably. Also, the spectral response profile expected from the USS was not in agreement with the analysis results; the profile indicates that the system suffered from some hardware/software issue that caused the change in profile. Several attempts were made to reprocess data using a utility developed by the vendor, but the results show similar variability. Several discussions were held with the vendor to address this problem. The vendor points the issues at a poor reference file, which could account for the unusual profile, as well as the variation in density measurement frequency.

The attenuation data shows possible use for tracking mixing process as a function of particle size distribution, but a wider bandwidth is required from the system. This could prove useful in tank applications were agglomeration needs to be addressed prior to retrieval. The Woods equation relating density and ultrasonic group velocity requires the bulk modulus of media, something not easily determined for slurries with multiple solid concentrations. The advantage of the USS is that hardware configuration is such that the density of the mixture can be extracted from measurement of the reflection of the ultrasonic wave at the interface of the transducer and the media. This reflectance technique for density was utilized by PNNL for development of a pipeline density monitor [1]. Issues with temperature drift and reflectance limitations of the transducer caused issues in measurement accuracy.

A commercial Coriolis mass flow meter provides an absolute error less than $\pm 0.2\%$ versus a reflectance-based error of $\pm 2\%$. The major advantage of the USS is the simplicity of the deployment and sampling platform versus what would be required for an in-situ Coriolis-based probe. The needs for pumps, valves, flushing, and complexity of controls would be greater for the Coriolis-based system, versus the USS.

Future work could focus on improvements to the reflectance measurement through variations in reflectance scheme, improved temperature compensation for the transducer, and the utilization of alternative materials can improve the measurement error down to the range of a commercial Coriolis meter. Also, a change to the controller would be to deploy software directly on an onboard real-time OS platform, which will alleviate timing and communication faults caused by typical fairness-scheme operating systems. This configuration could be used to send data unto an existing Hanford telemetry system, without the need for a user interface.

REFERENCES

1. Bamberger, J.A., Greenwood, M.S., Development of a Density Sensor for In-Line Real-Time Process Control and Monitoring of Slurries during Radioactive Waste Retrieval and Transport Operations at DOE Sites. Richland, WA.: Pacific Northwest National Laboratory, 2001.

2. Bontha, J. R., et. al. Test Loop Demonstration and Evaluation of Slurry Transfer Line Critical Velocity Measurement Instruments. Richland, WA.: Pacific Northwest National Laboratory, 2010.

3. Harker, A. H., J.A. G. Temple. "Velocity and Attenuation of Ultrasound in Suspensions of Particles in Fluids." 21.1576-1588, 1988.

4. Lipták, Béla G. Instrument Engineers' Handbook, Fouth Edition, Volume One. Boca Raton: CRC Press, 2003.

5. Vanatta, M., "Waste Feed Delivery Small Scale Mixing Demonstration Simulant Selection Report for Phase 2 Testing", PL-SSMD-PR-0003, Rev 1, RPP-48358 Rev:0, Energy Solutions, Richland, WA, 2011.

6. Webster, J.G. The Measurement, Instrumentation, and Sensors Handbook. Boca Raton: CRC Press, 1999.

APPENDIX A

Search queries performed during literature and technology search

- ultrasonic waste slurry
- slurry velocity measurement
- slurry critical velocity
- in-situ viscosity
- in-situ density measurement
- in-situ PSD measurement
- ADCP Particle concentration
- acoustic backscattering PSD
- ERT linear probe
- linear probe tomography
- in-situ tomography
- in-situ characterization
- in-situ scattering
- in-situ spectroscopy
- in-situ thermal analysis
- in-situ thermodynamic
- in-situ particle characterization
- infrared spectroscopy in-situ
- Raman spectroscopy in-situ
- ultrasonic spectroscopy
- in situ ultrasonic
- UDV in situ
- in situ diffraction
- in situ particle size

APPENDIX B

Literature and technology search results

Technology Name	Description	Measurement Principle	Measures?	Sampling Rate (S/sec)	Measurement Range	Deployment platform	Pros	Cons	Vendor	Comments
Focused Beam Reflectance Measurement (FBRM)	The FBRM technique focuses an IR laser beam (wavelength?) to the outside surface of a sapphire window, which is in contact with the system to be measured. The laser optics are rotated at a controlled high-speed so the focused beam can scan across the system in a circular path. This focused beam reflects light when it traverses along the body of particles passing through the scanning circle. The reflection time, when used in conjunction with the scanning velocity, can be used to calculate a chord length for the particles. Several thousand of these measurements can be taken per second, with various analytical techniques used to correlate to PSD.	Optical	Chord Length Distribution (CLD)	>1000	0.8 - 1000 um	In-vessel probe (Hastelloy C-276, Sapphire, Kalrez)	1. Various techniques for CLD to PSD correlation. 2. Fine or course electronics modules for greater edge detection 3. available in-situ configuration 4. no on-board electronics 5. Previously deployed in rad environment (ORNL, France)	1. FBRM results typically broader than other PSD techniques; can oversize small particles, and undersize large ones. Due to laser beam broadening/spreading 2. sensitive to multi-scattering effects 3. Sensitive to location and orientation in vessel; highest count when dominant flow direction towards probe measurement window 4. substances with similar index of refraction provide meaningless results	Mettler-Toledo AutoChem	Deployed at Hanford & ORNL in line configuration (factsheet provided by MT representative (P. Scholl)
Optical Back-Reflectance Measurement (ORM) / Laser Time of Reflection (TOR) Analysis	The ORM technique focuses a rotating laser beam (wavelength?) to preset ranges outside of a window, which is in contact with the system to be measured. The laser setup is configured for a single scan mode, thereby reducing the multi-scattering effects of systems that are focused at the sensing window. An additional capability of selective multi-depth focus (3D SMF) allows for the focus to be adjusted by changing the laser pulse characteristics.	Optical	Chord Length Distribution (CLD)	>1000	< 0.5 - 4000 um	In-vessel probe (Hastelloy)	1. Capability to adjust focus location 2. single mode fiber reduces multi-scattering effects 3. available in-situ configuration 4. no on-board electronics 5. faster, farther data transmission capabilities	1. substances with similar index of refraction provide meaningless results 2. refractive particle could lead to a loss of measurement 3. little or no deployment information on technique 4. Sensitive to location and orientation in vessel; highest count when dominant flow direction towards probe measurement window	HEL Group, Inc.	Representative (B. Giordano) claims that system has improved accuracy in CLD/PSD over FBRM based on smaller, single-mode fiber filtering scattered light
Capacitance Profiling	Method measures capacitance between source electrode, and a vertical array of detector electrodes in an integrated PCB. The column can be deployed into a tank using metal flange/column assembly for structure. The tank contents are allowed to enter the inter-electrode spacing via a notch in the deployment column. Technology is measuring bulk permittivity of the contents	EM	Bulk Permittivity	~2	0 - 10 pF	In-vessel probe	1. In-situ configuration 2. Expandable to fit more electrodes 3. ECT techniques can be applied to this method (LBP) 4. Resolution function of AD conversion process	1. poor temperature response (due to scaling; poor material selection) 2. single excitation electrode limits capabilities 3. poor spatial resolution 4. single point measurement 5. conductivity of liquid must be evaluated 6. No available commercial vendor/unit	N/A (UMIST)	
Ultrasonic Doppler Velocimetry (UDV) / Acoustic Doppler Current Profiling (ADCP)	Ultrasonic bursts are transceived to determine the relative phase shift caused by suspended particles. This phase shift can be correlated to particle location. ADV typically used for measurement of mean velocities and turbulent intensities of sediment motion or fluid currents.	Ultrasound	Doppler shift	0.1 to 50	3 - 250 cm/s	in-vessel probe (lab scale)	1. deployed in-situ for sediment transport measurement 2. single transceiver required for system 3. can provide interface b/w mixing and stationary waste level	1. very limited SNR/resolution in high solids concentration 2. use of lower operating frequency to limit attenuation, would degrade resolution	SonTek/YSI	Prior use in determining sediment transport and turbulence in settled fluidized beds.
Electrical Capacitance Tomography (ECT)	Method measures capacitance between source electrode, and a circular array of detector electrodes. The source/detector configuration is changed for each array element to create spatial grid of measurement paths. These values, when processed utilizing a linear back-propagation algorithm, can be expanded to create a map of permittivity distribution of the working space bounded by the electrode array.	EM	Bulk Permittivity	up to 200 (frames)	None defined	in-line configuration (lab version)	1. Can monitor changes in relative permittivity with accuracy of 5% 2. Can determine solids distribution within measurement area	1. designed for in-line analysis 2. designed for lab use 3. Use linear back propagation algorithm to generate permittivity distribution map (approximation)	Tomoflow	
Energy Dispersive X-ray Diffraction (EDXRD)	Method solves the Bragg equation, while maintaining the Bragg angle as constant. This method detects the wavelength of the diffracted beams of the originally polychromatic beam. This method does not require a goniometer, as required for typical angle-dispersive diffraction techniques, thereby simplifying the deployment for XRD.	Optical/EM	chemical composition based on diffraction pattern	None defined	None defined	lab version	1. Allows for chemical composition and physical characterization	1. x-ray source and optics required near measurement area 2. no in-situ systems available	Xstream Systems	
Electrical Resistance Tomography (ERT)	Method measures voltage between pairs of electrodes that has been injected by a source electrode. The source/detector configuration is changed for the array elements to create a 2D estimate of measurement paths. These values, when processed utilizing a linear back-propagation algorithm, can be expanded to create a map of conductivity distribution of the working space next to the electrode array.	EM	conductivity (solids concentration)	None defined	None defined	in-situ probe	1. linear probe in field ready configuration (tested in 3.5M nitric acid reactor) 2. Correlation between conductivity measurement and solids concentration (Maxwell's Eq) 3. Can be used for phase detection	1. Use of modified sensitivity back propagation (MSBP) algorithm for map (approximation) 2. electrochemical double-layer effect 3. Susceptible to EM noise near electrodes	Industrial Tomography Systems plc	Tested for sludge settling at UMIST (T. York) in impedance mode in a trident configuration; successfully tracked sludge settling when compared to visual inspection
Lamb (Stoneley) Wave Viscosity Measurement	Method uses shear wave along interface between liquid and solid media and wave equation to determine viscosity of liquid media. Can be applied as a Lamb (at end of waveguide), or completely along boundary (Stoneley)	Ultrasound	Viscosity	None defined	< 7 mPa	lab version	1. capable of in-situ measurement 2. simple sensing electrode / electronics module 3. no field calibration necessary	1. Only available in lab scale configuration; no industrial deployments 2. Additional research efforts required to determine optimum deployment configuration and assess impact of multi-phase media 3. Limited viscosity range in current incarnation	N/A	
Laser Diffraction	Method uses photodetectors to measure diffraction patterns generated by particles interacting with a near IR laser light. Typically used in dilute applications, within air or clear fluids. Multiple scattering phenomenon has been used with techniques to correct dynamic range of instruments under high solids loading applications	Optical	Particle Size Distribution (PSD)	None defined	0.1 - 1000 um	in-line configuration / in-situ configuration	1. determined actual system PSD 2. in-situ deployment probe available 3. no field calibration necessary	1. requires dilute concentrations 2. probe not chemical/rad hardened 3. limited probe length	Malvern Instruments	Discussions with representative (M. Lighfoot) yielded that Parsum IPP 70 could NOT be used in chem hardened fluid due to window material
Raman Spectroscopy	Method uses the vibrational spectra given off by chemicals when interrogated by a laser in the visible/near-infrared region to determine their identity. Method requires reference Raman signatures in order to classify the resulting spectral response. Method has limitations when interrogating dark matter, as very little light is reflected.	Optical	Chemical composition/concentration	None defined	dependant on reference library number of signatures	in-situ probe (iTSR)	1. in-situ deployment probe available 2. provides composition and concentration measurements 3. testing resulted in over 90% accuracy in identification and concentration	1. requires reference signature library for identification 2. pronounced peak from a specific compound can obscure others 3. signal quality was an issue in in-tank configuration evaluated by Hanford (w/ CPT for deployment)	Kaiser Optical Systems Inc.	Tested at Hanford (iTSR) with Cone Penetrometer for deployment. Never tested in HLW tank.
Dynamic Light Scattering	Method consists of a monochromatic laser light that falls on a sample region, while the scattered light is detected at various solid angles. This data can be used to calculated the PSD using the mathematical model for light scattering phenomenon (Mie Theory)	Optical	Particle Size Distribution (PSD)	None defined	< 6.5 um (lab version)	lab version probe	1. direct PSD measurement 2. reliable measurements 3. no calibration required	1. low particle size applications 2. no in-situ systems available	Wyatt Technology/Microtrac	
Ultrasound Spectroscopy (USS)	Method measures the change in ultrasonic signal per unit distance at various interrogation frequencies. This causes an energy loss in the wave that is characteristics of the material properties.	Ultrasound	Density and Viscosity	slurry dependant	slurry dependant	lab version probe	1. direct bulk density and viscosity measurement 2. simple transmitter-receiver pair configuration 3. Data can be used for trending on mixing process homogeneity	1. no in-situ systems available 2. requires standards/calibration for results interpretation	Industrial Tomography Systems plc	
Vibration-based Density measurement	The vibration-based density measurement is a technique that utilizes the damping caused by the test material on a vibrating object(s) to determine the material properties. This method that has been utilized in industry for some time in several incarnations; these include tuning forks, twin-tube and Coriolis-force based meters.	vibration/resonant damping	Density and Viscosity	~50	Density: up to 3.00 g/cc (tuning fork; undefined for other types)	in-situ probe (tuning fork/Coriolis)	1. simplicity of measurement principle 2. compatible with chemically-agressive slurries 3. on-board temperature and viscosity compensation	1. on-board electronics 2. element fouling/plugging can lead to measurement errors 3. limited density range (tuning fork) 4. sensitive to bubbles and fast composition changes 5 sensitive to flow pattern changes/stray currents (due to jet flow)	Emerson Process (Rosemount), Endress-Hauser, Micromotion	

APPENDIX C

Summary spectral response (with error bars) for Base and Complex Trials

Complex solid mixture and NaNO$_3$ solution trial results

Trial Details

Suspension ID: T15SNBase4

Date: 10-27-2011

Solids (%): 0 – Base solution
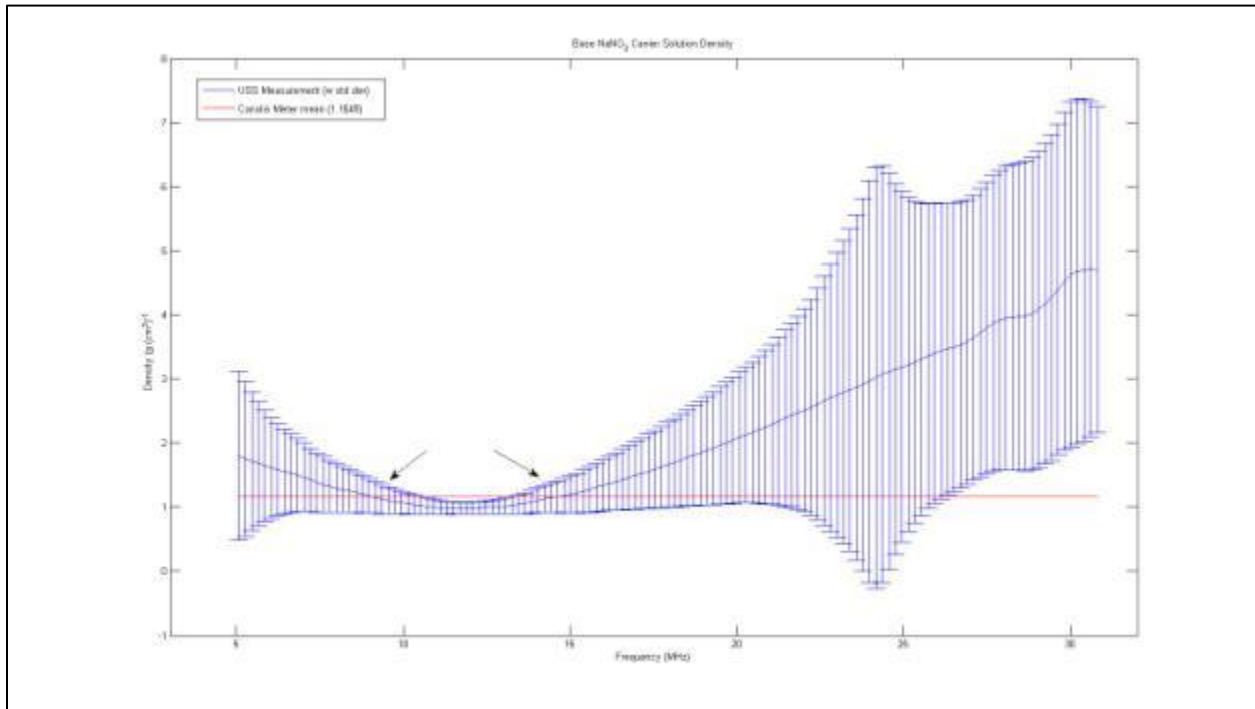
Result

Trial Details

Suspension ID: T15SN2CMPLXBase4

Date: 10-27-2011

Solids (%): 2

Result
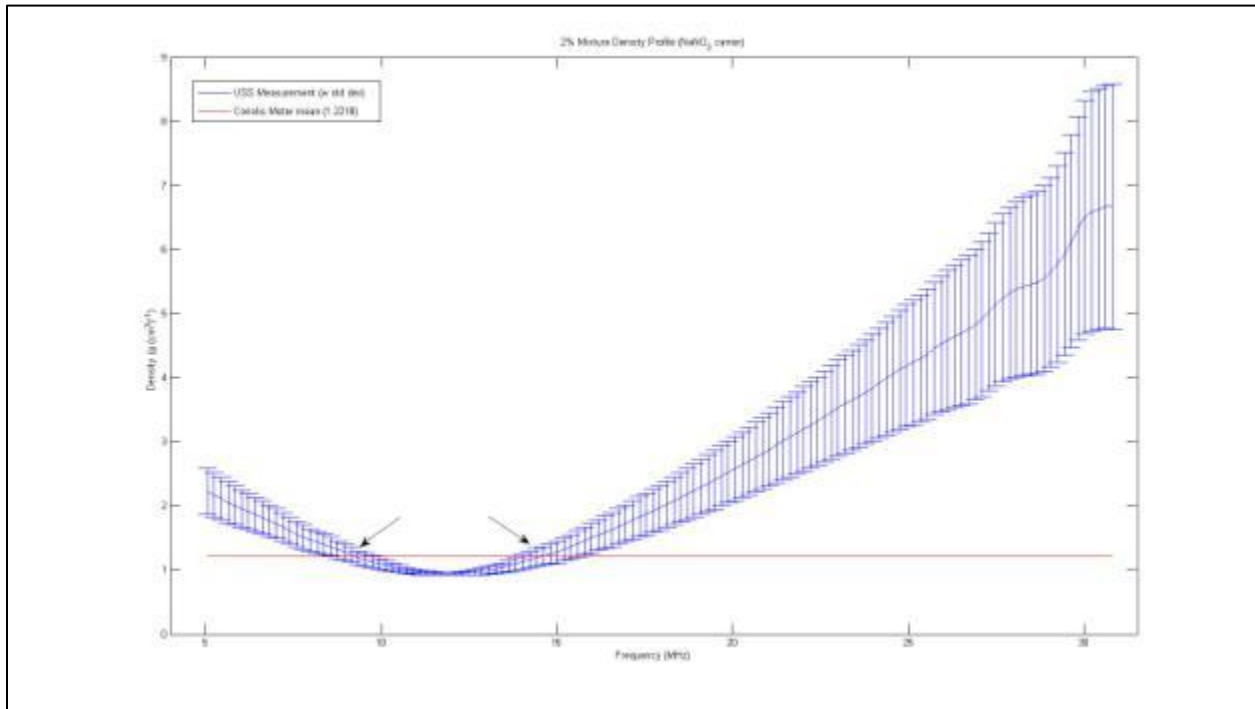
<u>Trial Details</u>

Suspension ID: T15SN4CMPLXBase4

Date: 10-27-2011

Solids (%): 4

<u>Result</u>
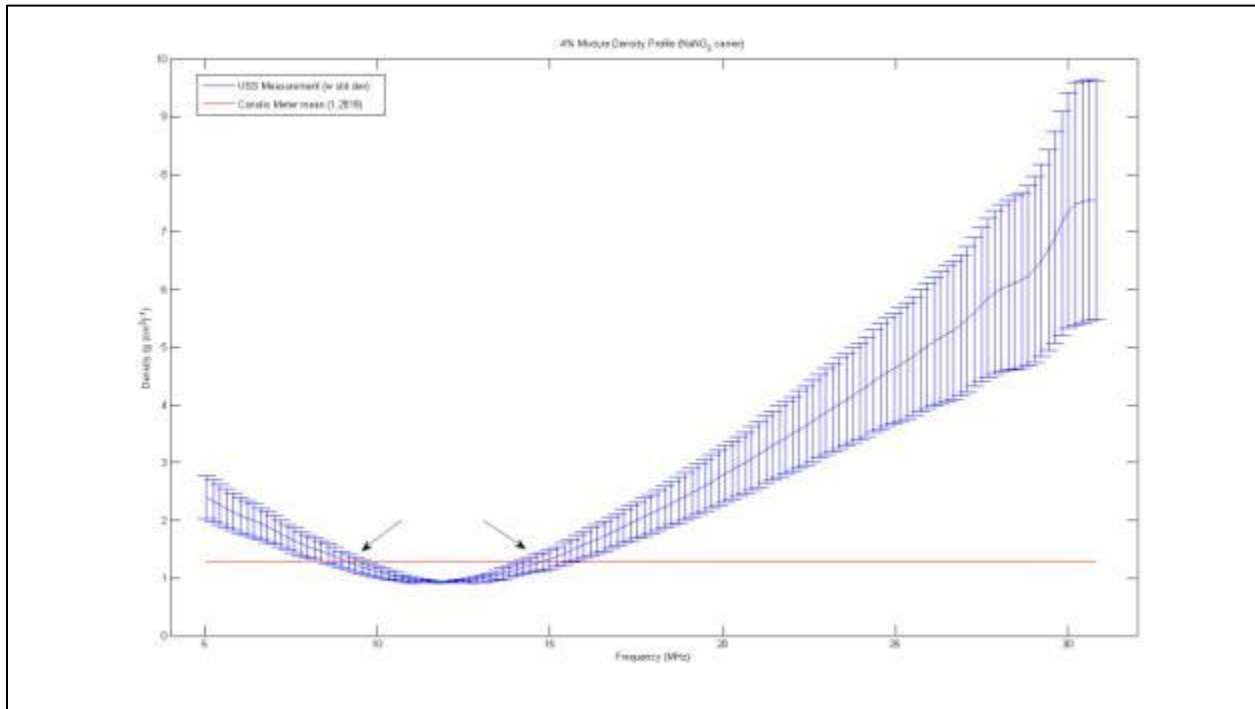
Trial Details

Suspension ID: T15SN8CMPLXBase4

Date: 10-27-2011

Solids (%): 8

Result
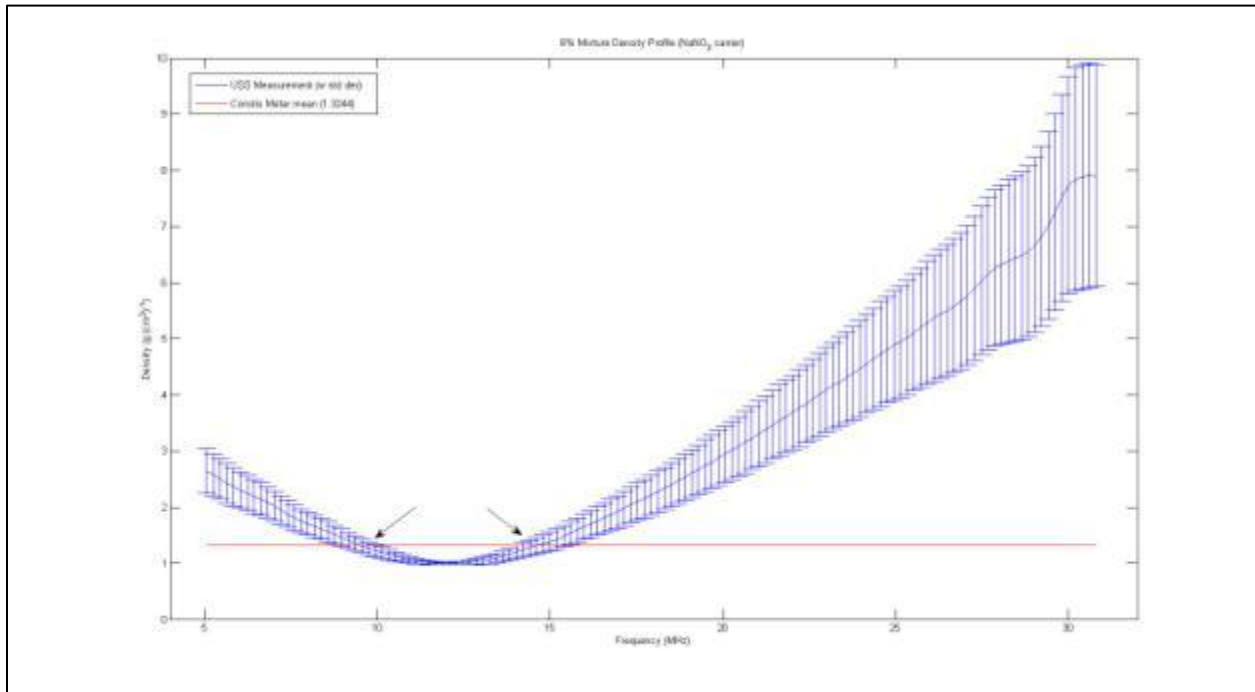
Trial Details

Suspension ID: T15SN10CMPLXBase4

Date: 10-27-2011

Solids (%): 10

Result
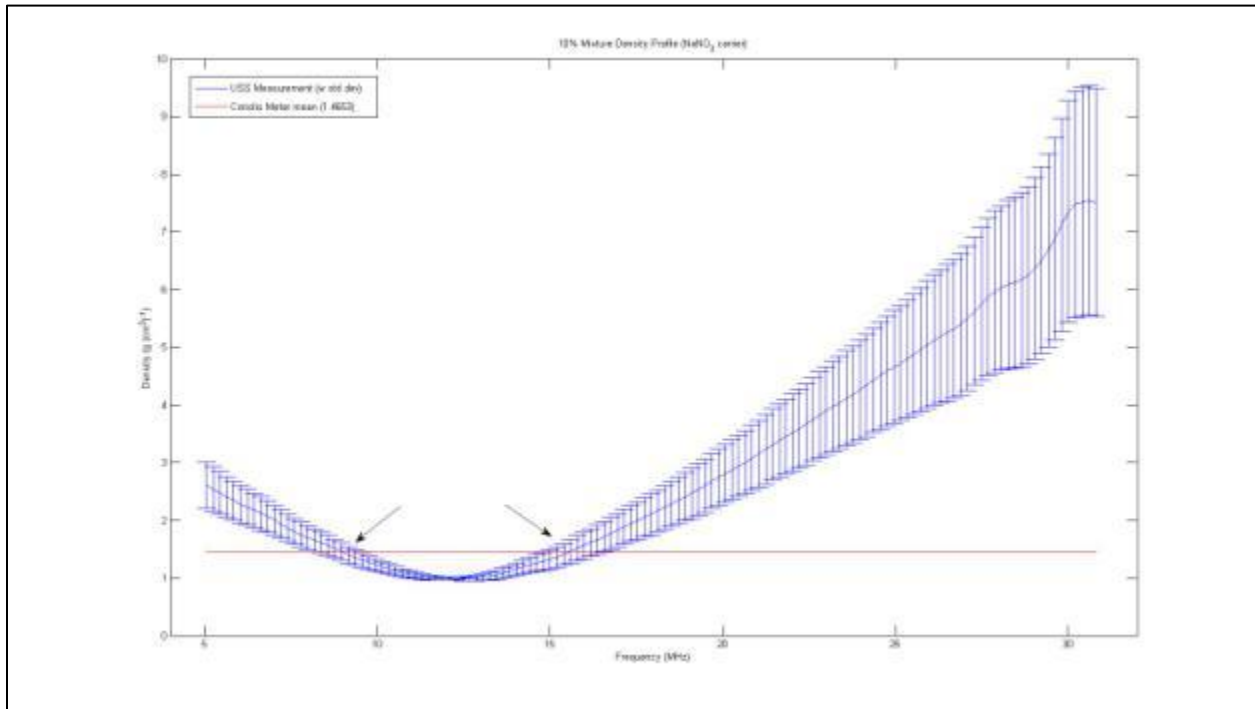
Complex solid mixture and RODI solution trial results

Trial Details

Suspension ID: T15WCMPLXBase

Date: 10-25-2011

Solids (%): 0 – Base solution
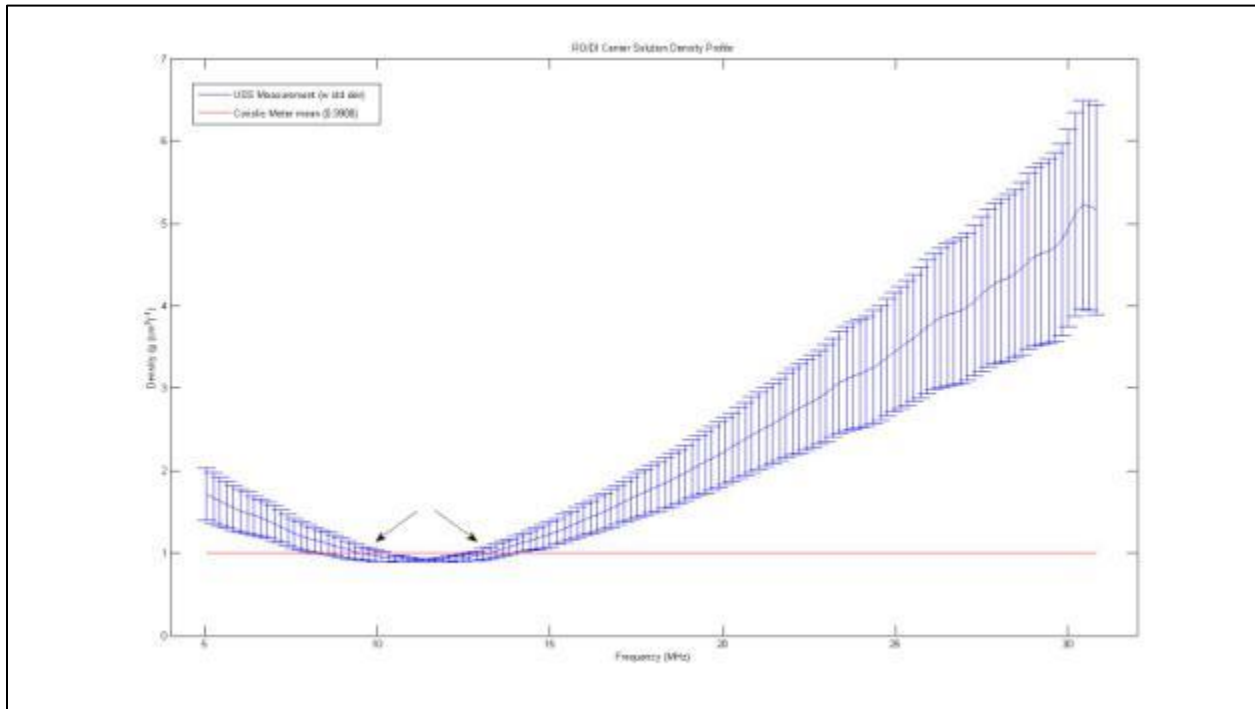
Result

Trial Details

Suspension ID: T15W2CMPLX

Date: 10-25-2011

Solids (%): 2

Result
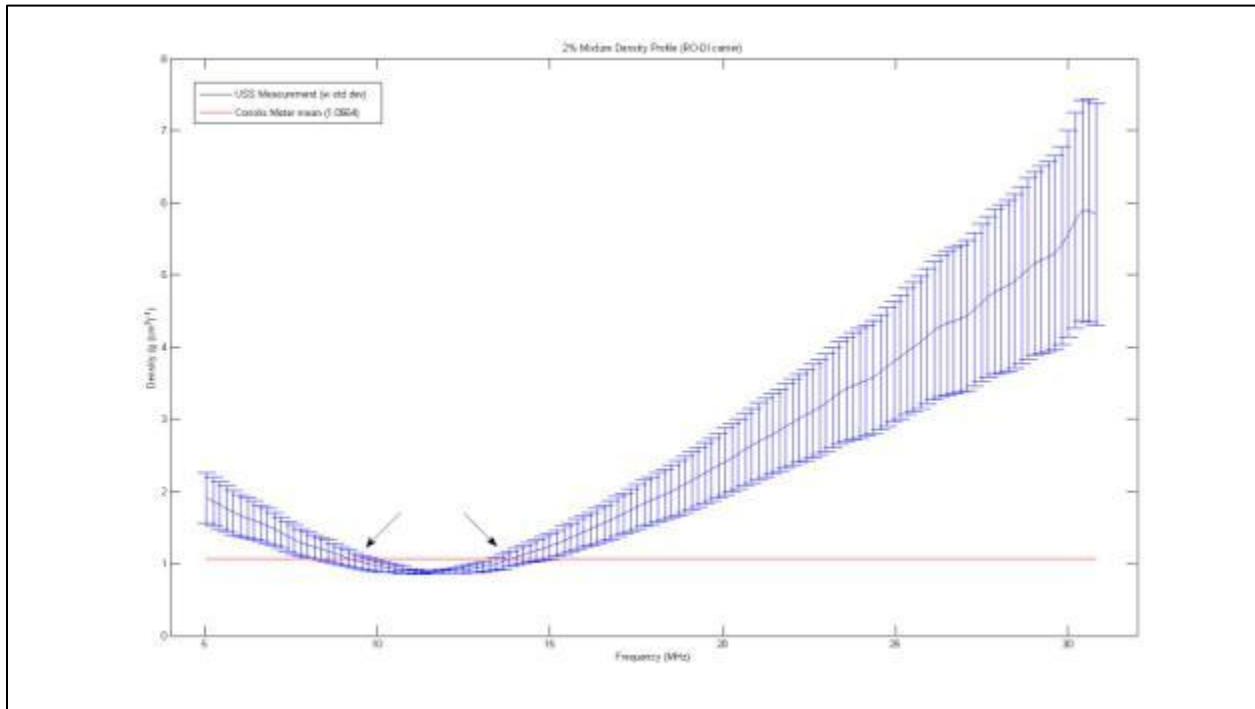
<u>Trial Details</u>

Suspension ID: T15W4CMPLX

Date: 10-25-2011

Solids (%): 4

<u>Result</u>
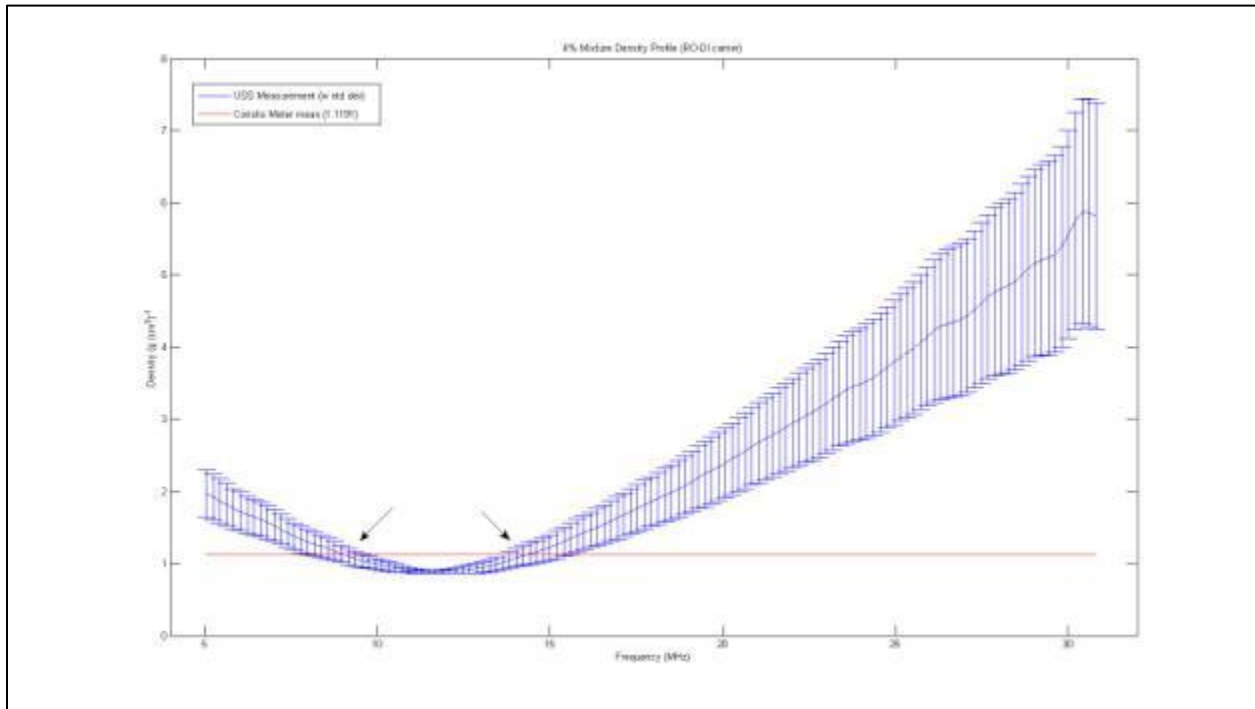
Trial Details

Suspension ID: T15W8CMPLX

Date: 10-25-2011

Solids (%): 8

Result
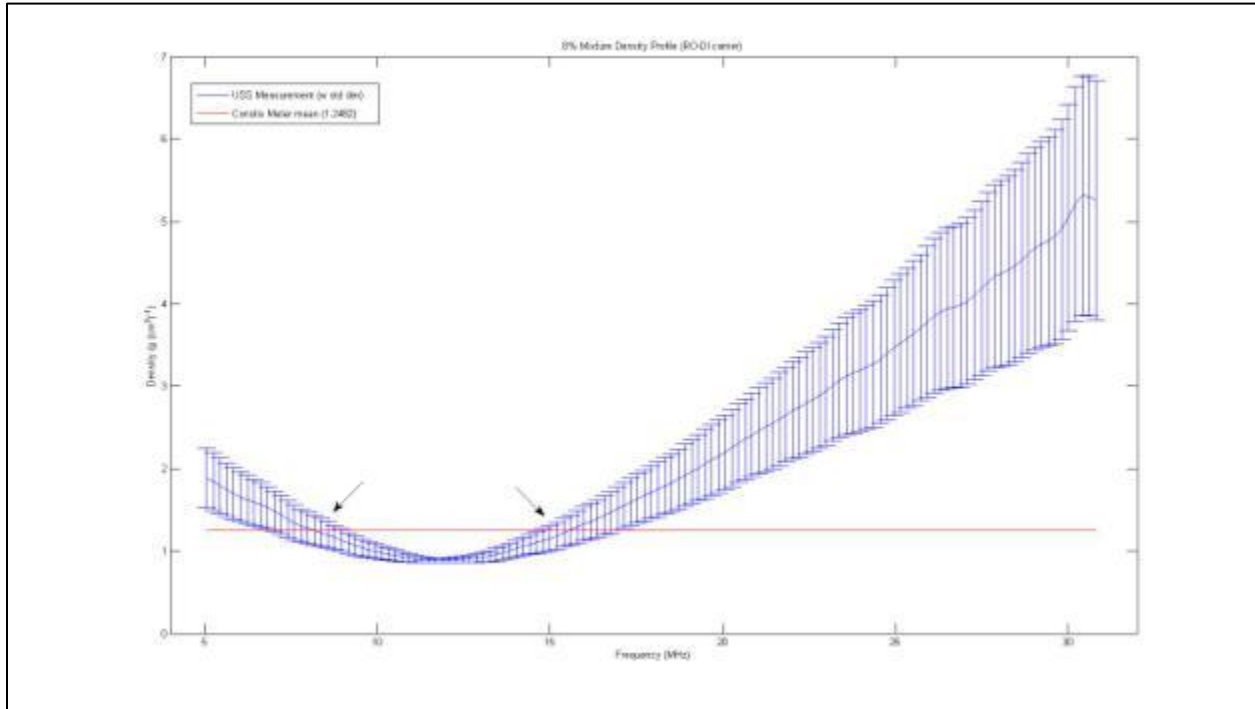
Trial Details

Suspension ID: T15W10CMPLX

Date: 10-25-2011

Solids (%): 10

Result
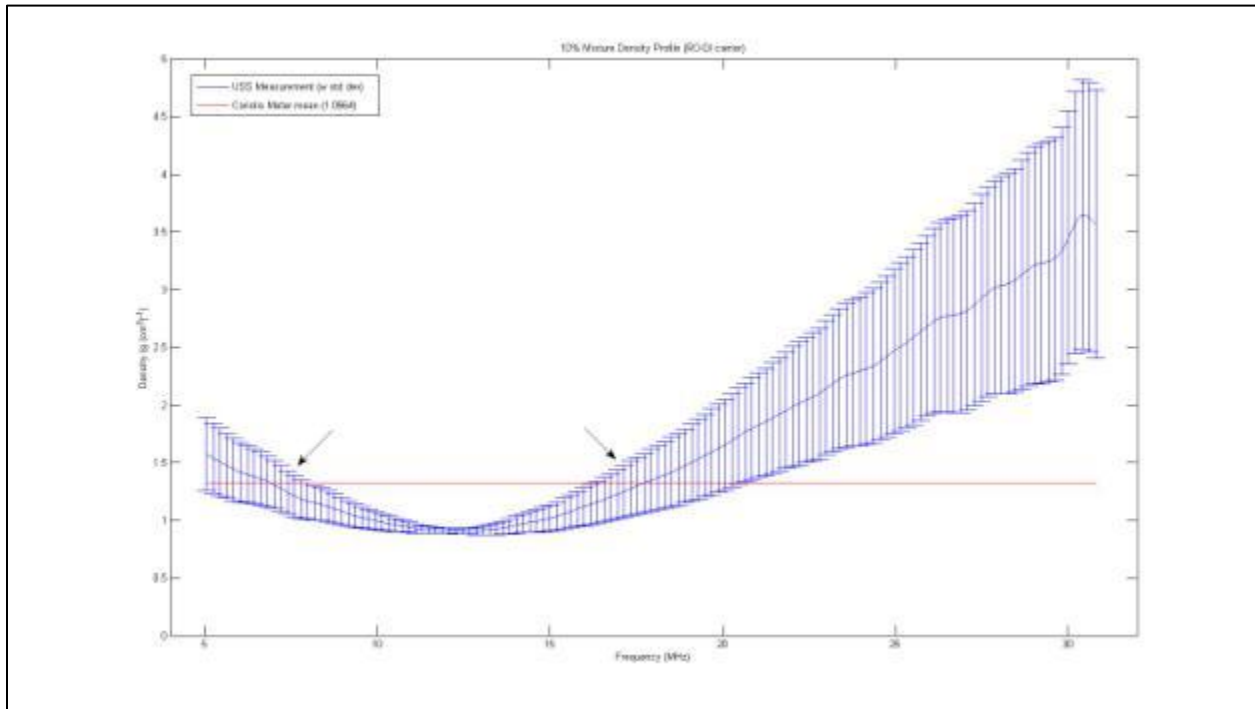
Base solid mixture and NaNO$_3$ solution trial results

Trial Details

Suspension ID: T15SNBase3

Date: 10-24-2011

Solids (%): 0 – Base solution
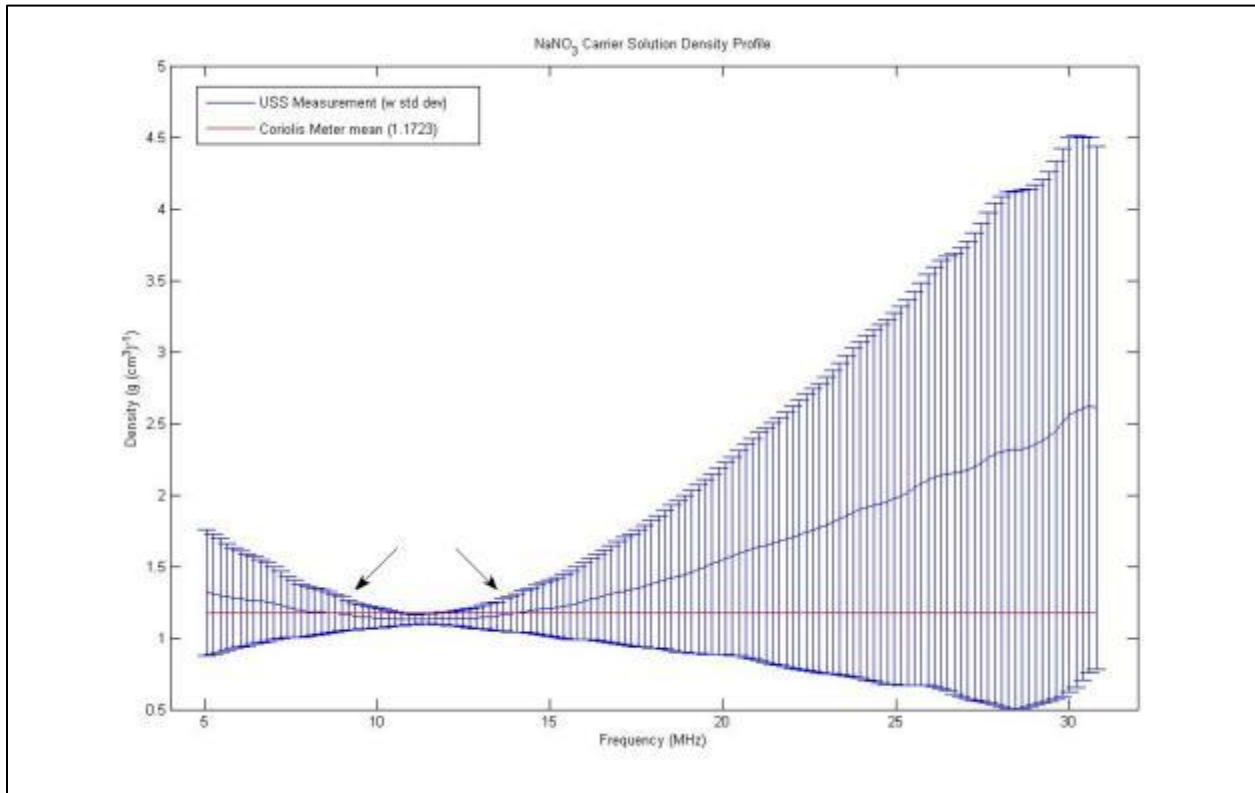
Result

Trial Details

Suspension ID: T15SN2B3

Date: 10-24-2011

Solids (%): 2

Result
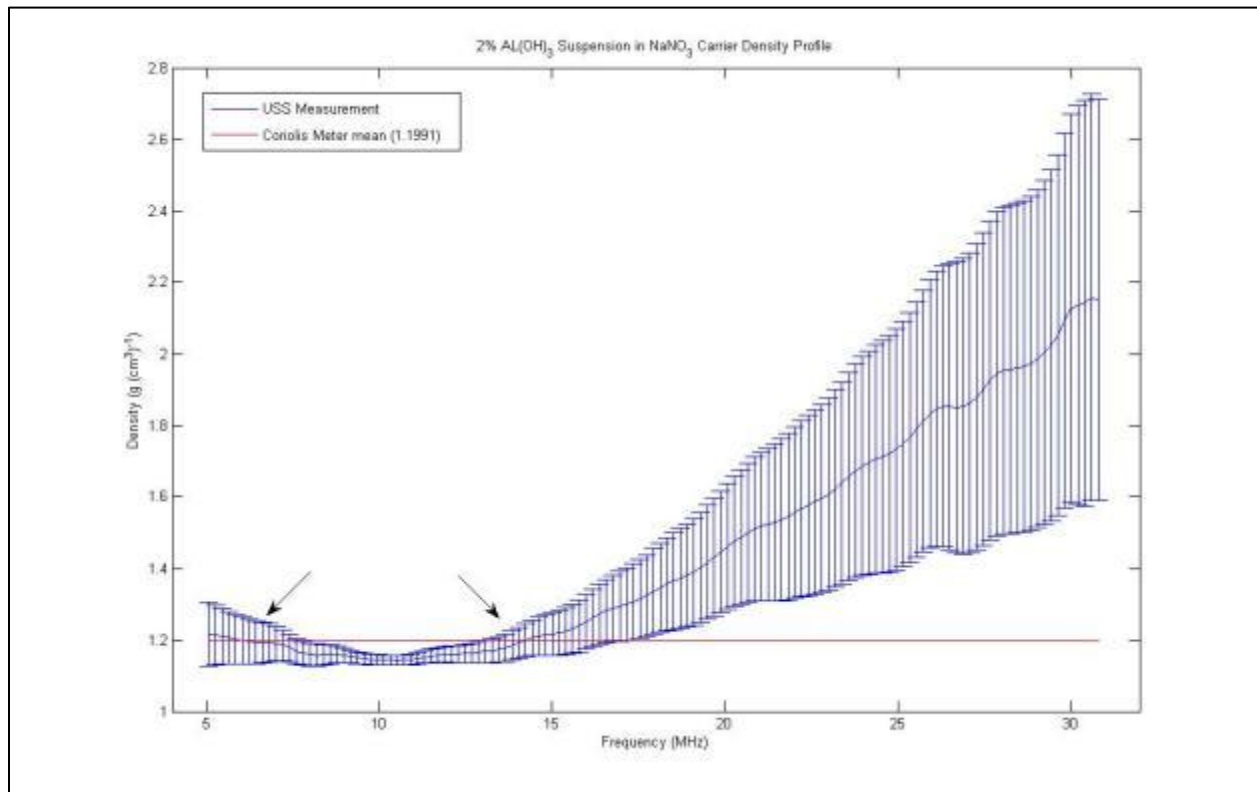
Trial Details

Suspension ID: T15SN4B3

Date: 10-24-2011

Solids (%): 4

Result
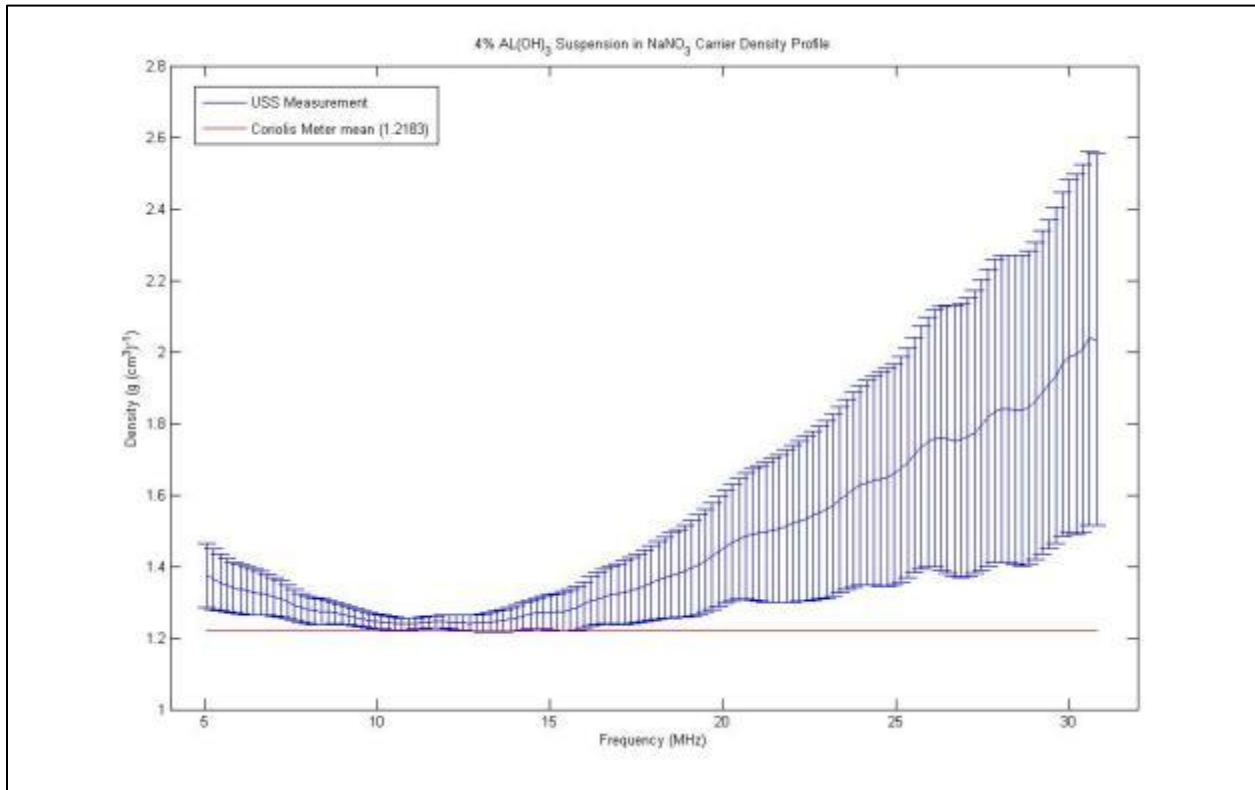
Trial Details

Suspension ID: T15SN8B3

Date: 10-24-2011

Solids (%): 8

Result

8% AL(OH)₃ Suspension in NaNO₃ Carrier Density Profile
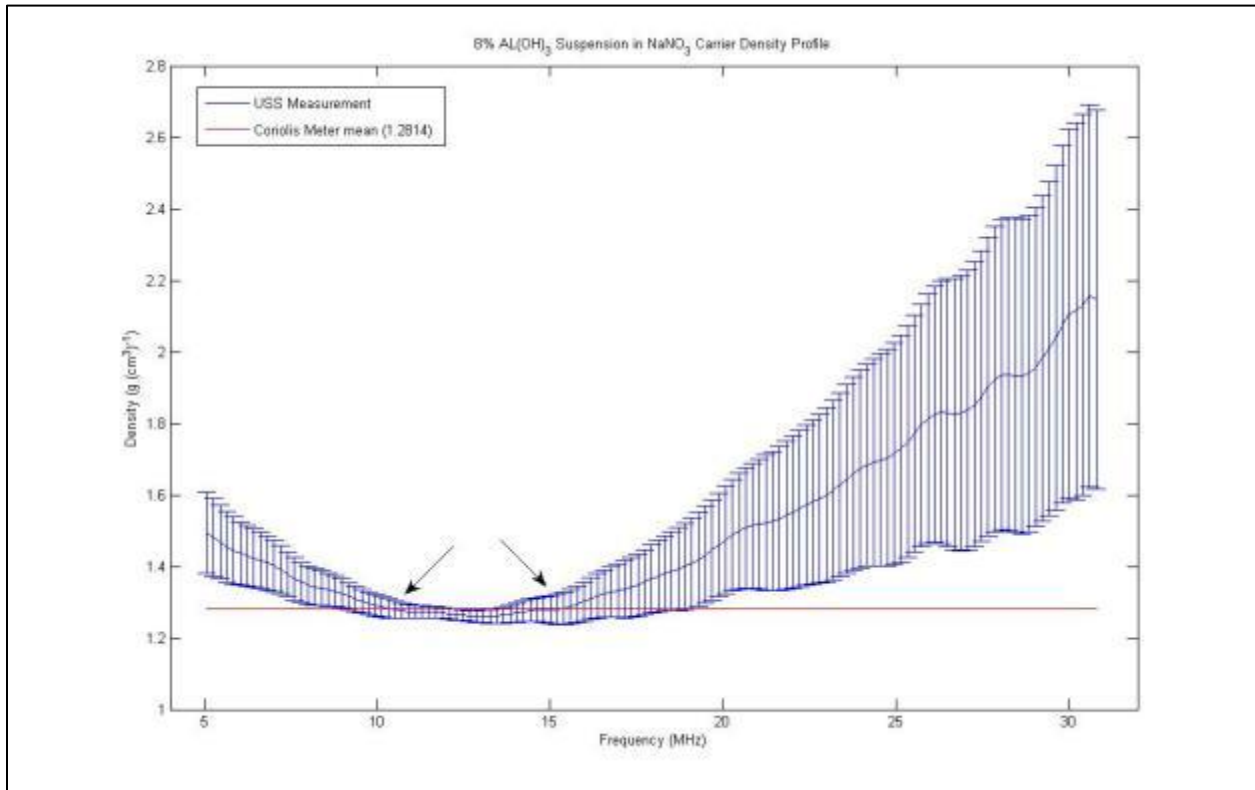
Trial Details

Suspension ID: T15SN10B3

Date: 10-24-2011

Solids (%): 10

Result

10% AL(OH)₃ Suspension in NaNO₃ Carrier Density Profile
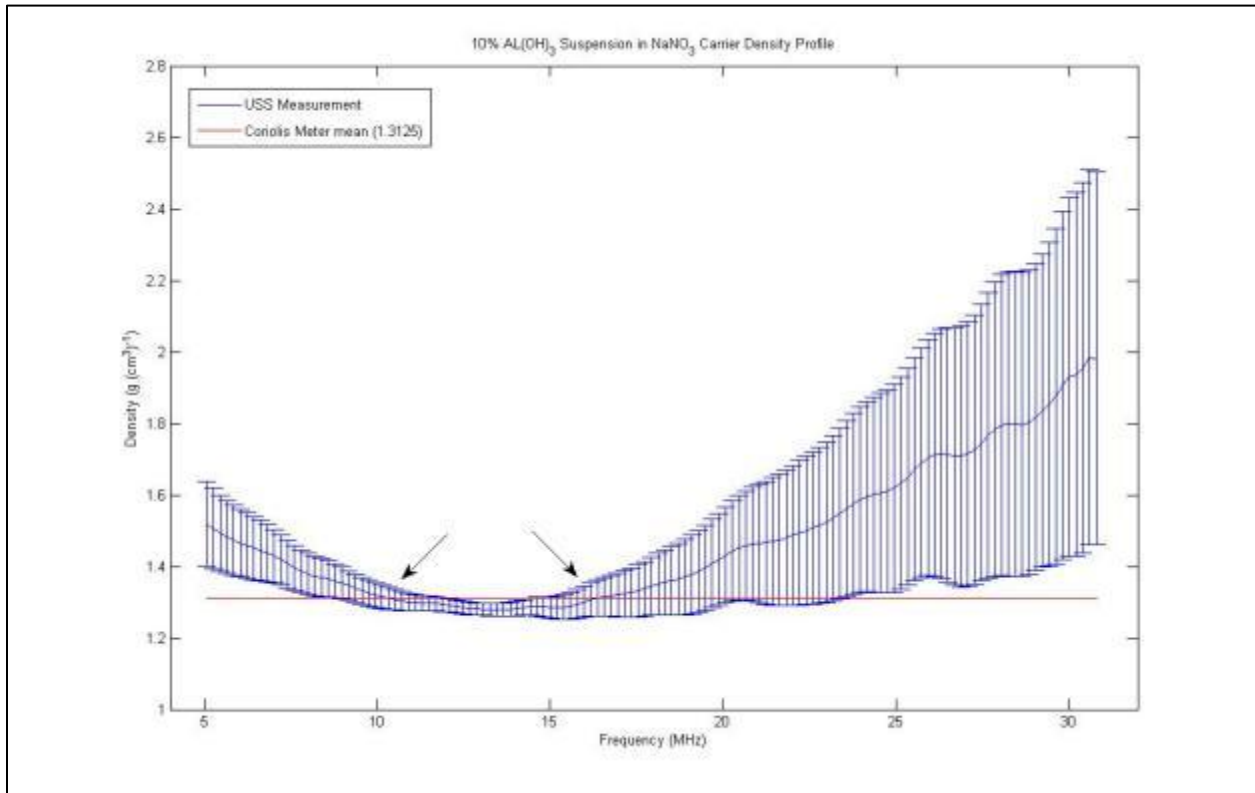
Base solid mixture and RODI solution trial results

Trial Details

Suspension ID: T15WBase

Date: 10-06-2011

Solids (%): 0 – Base solution

Result

ARC 2011 Year End Technical Report
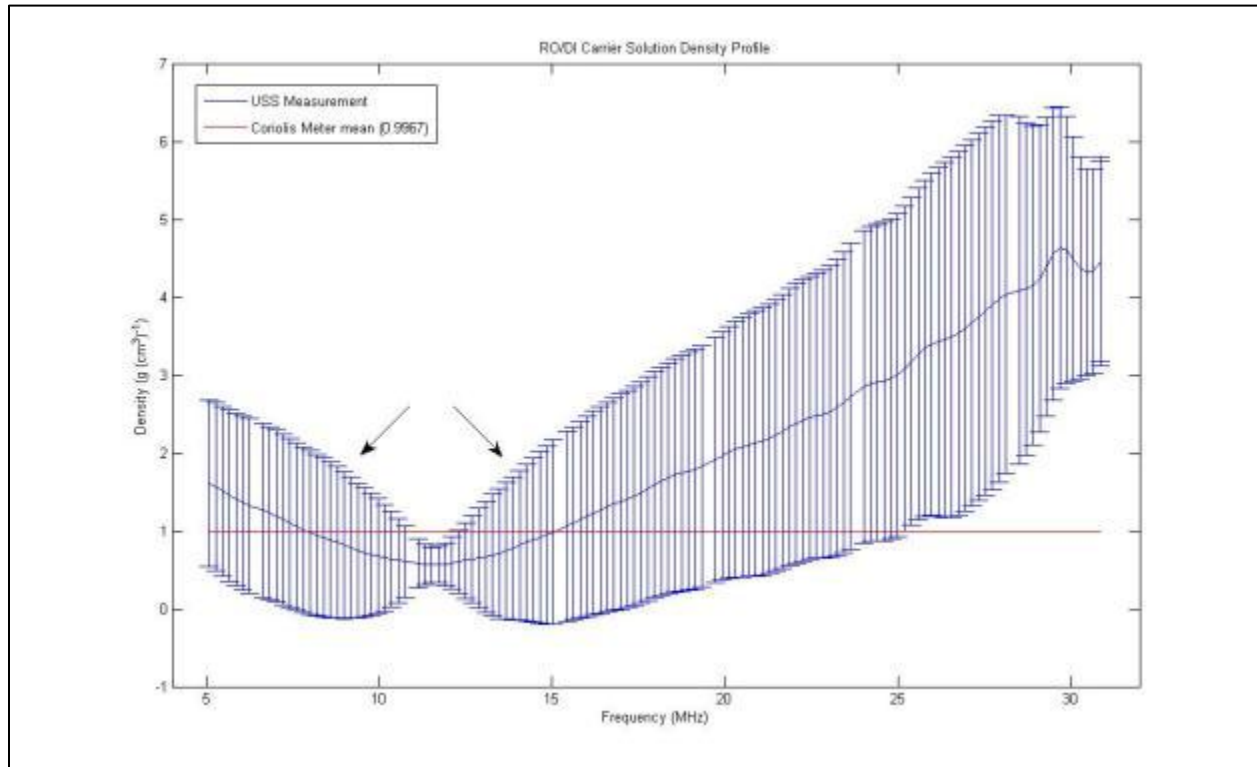
<u>Trial Details</u>

Suspension ID: T15W2T2

Date: 10-06-2011

Solids (%): 2

<u>Result</u>

2% AL(OH)₃ Density Profile (RO-DI carrier)
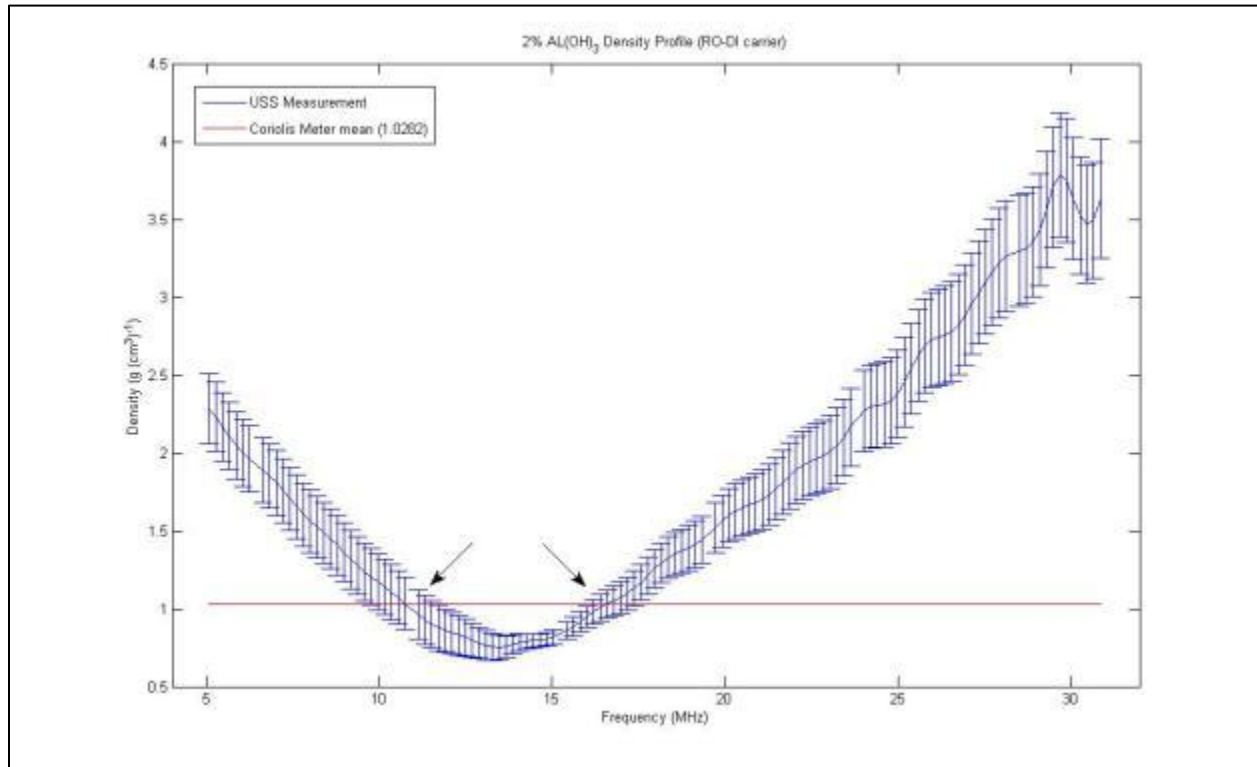
Trial Details

Suspension ID: T15W4T2

Date: 10-06-2011

Solids (%): 4

Result
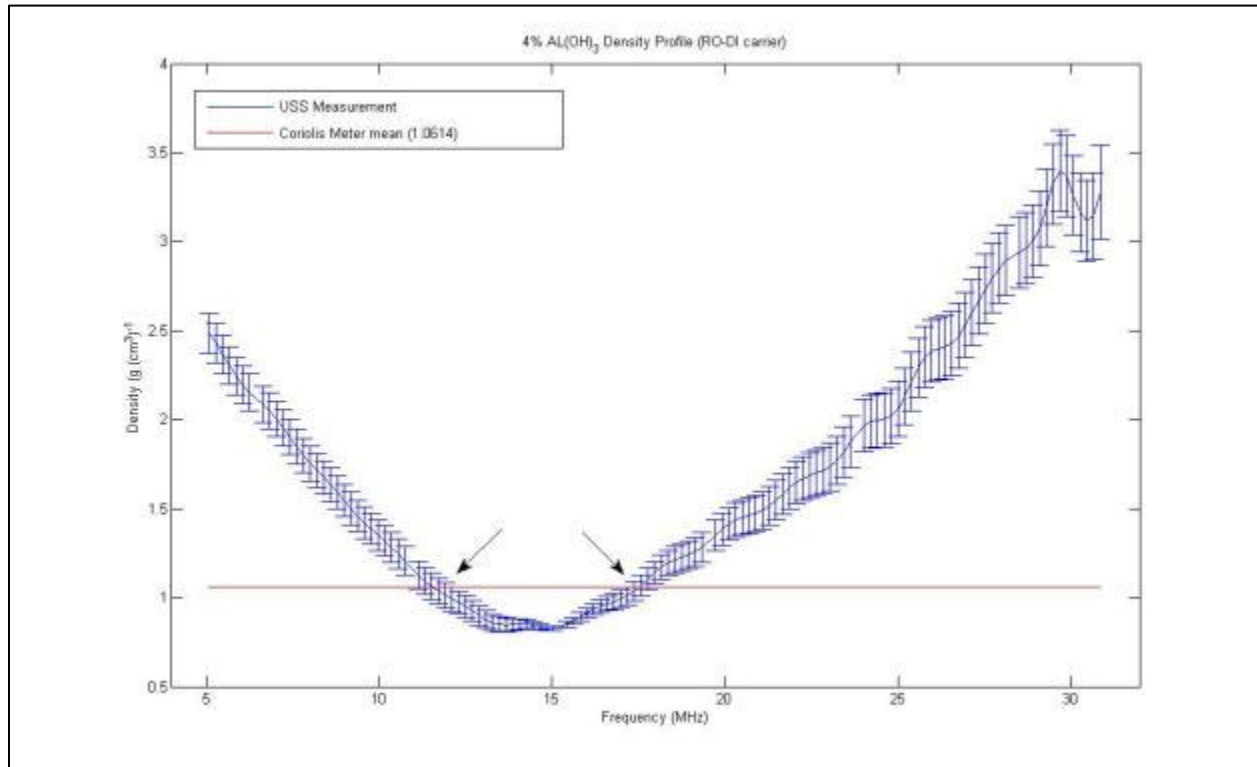
<u>Trial Details</u>

Suspension ID: T15W8T2

Date: 10-06-2011

Solids (%): 8

<u>Result</u>
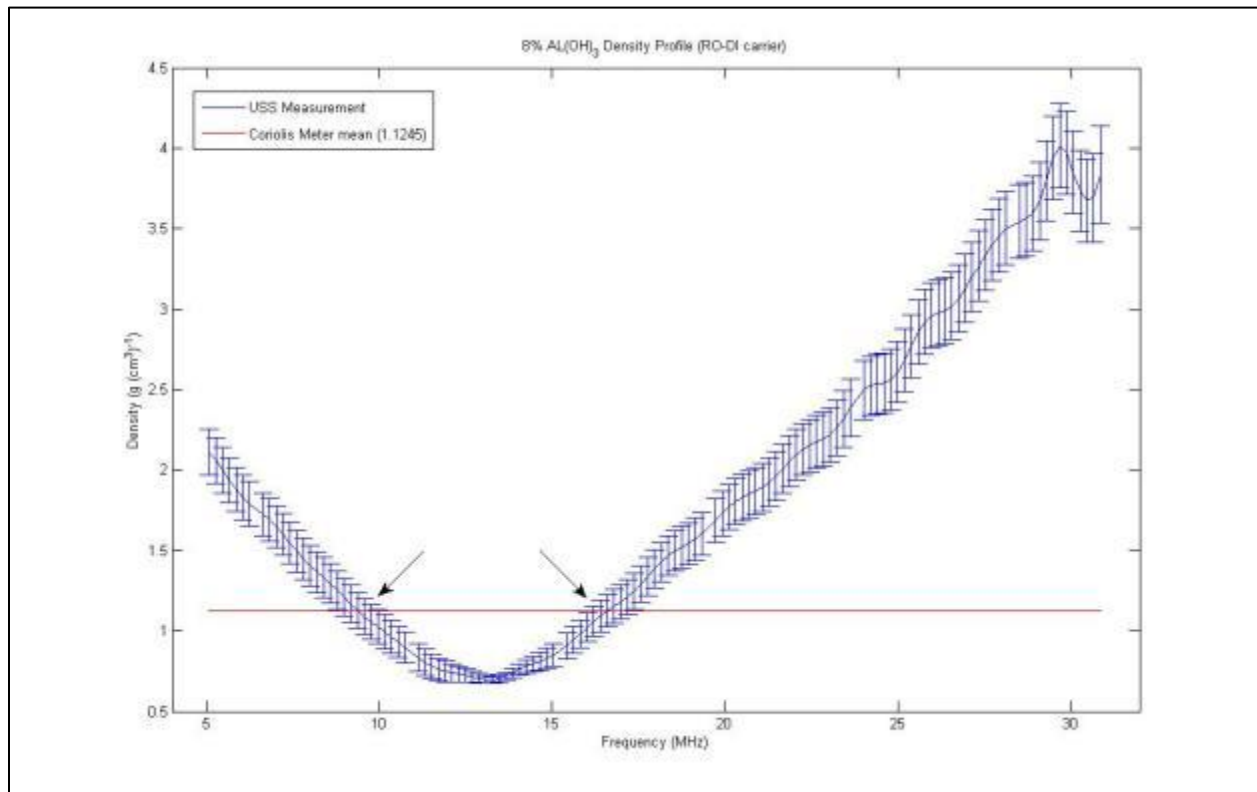
<u>Trial Details</u>

Suspension ID: T15W10T2

Date: 10-06-2011

Solids (%): 10

<u>Result</u>
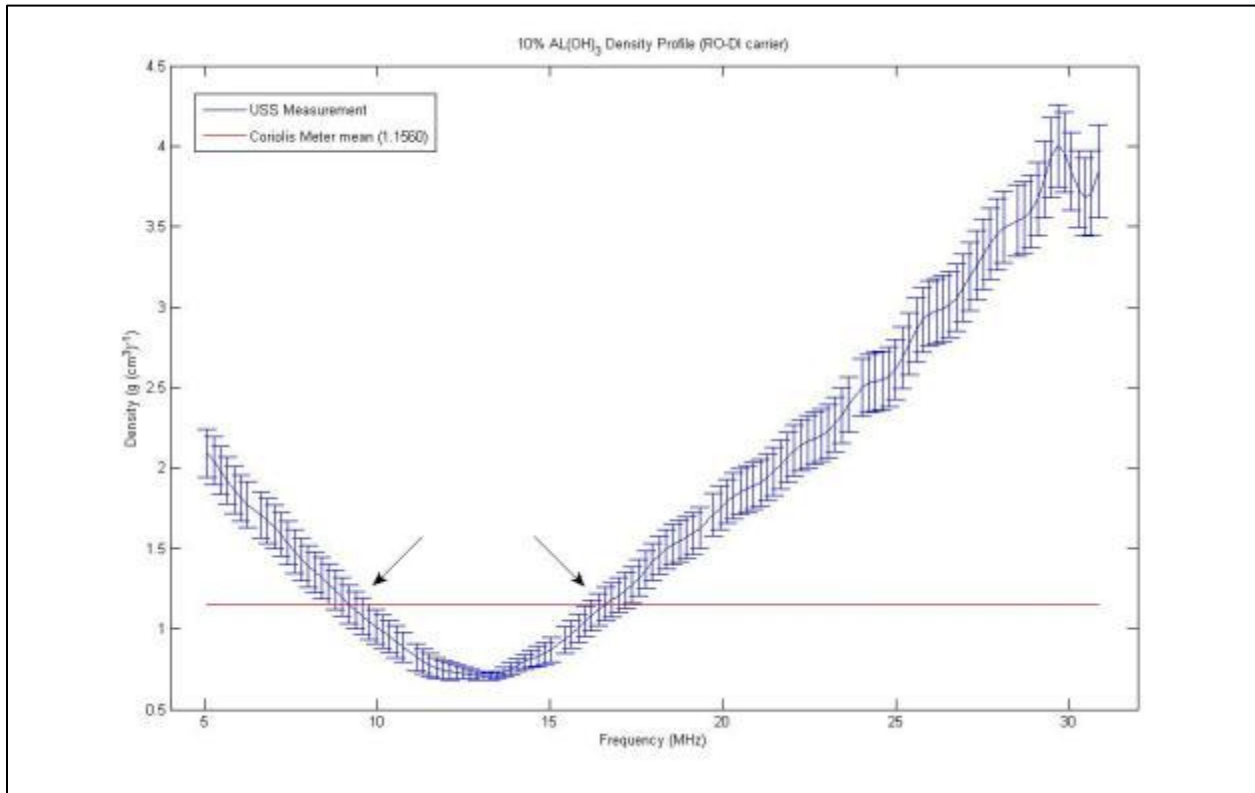
Trial Details

Suspension ID: T15W14T2

Date: 10-06-2011

Solids (%): 14

Result
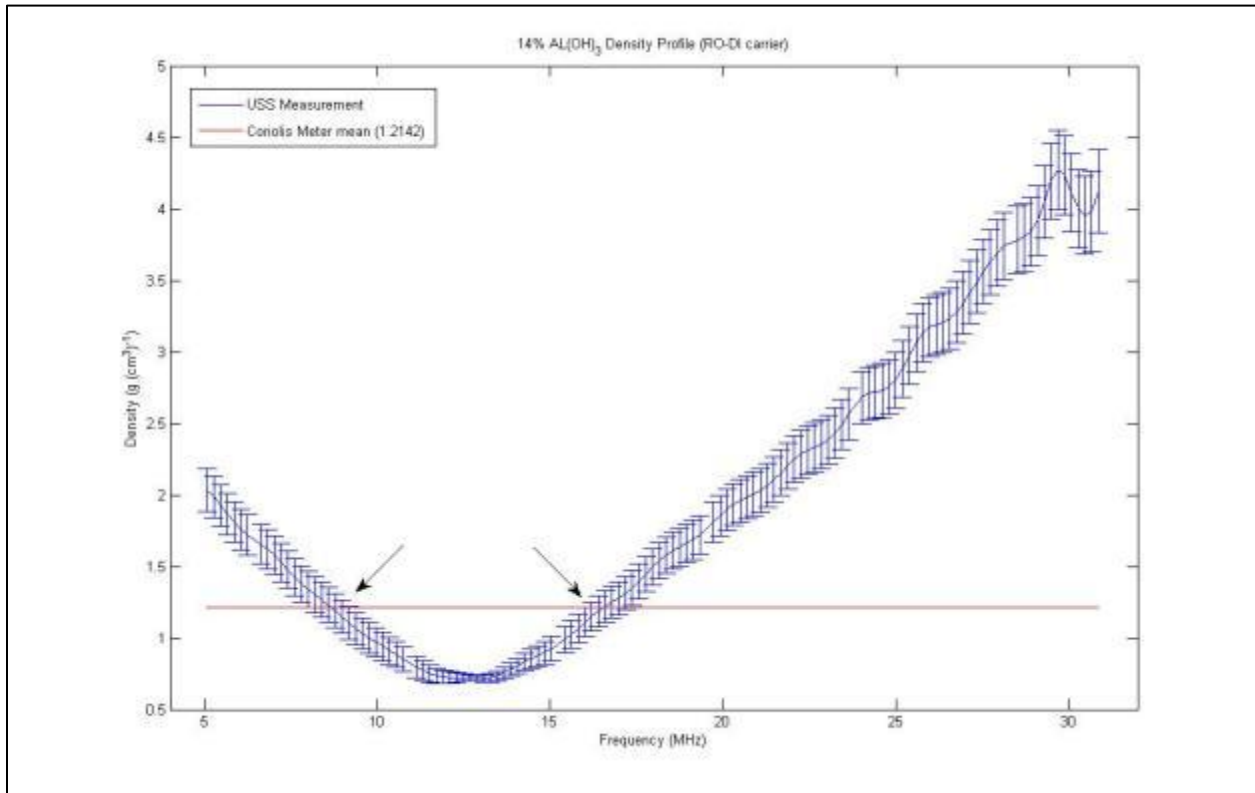
<u>Trial Details</u>

Suspension ID: T15W20T2

Date: 10-06-2011

Solids (%): 20

<u>Result</u>
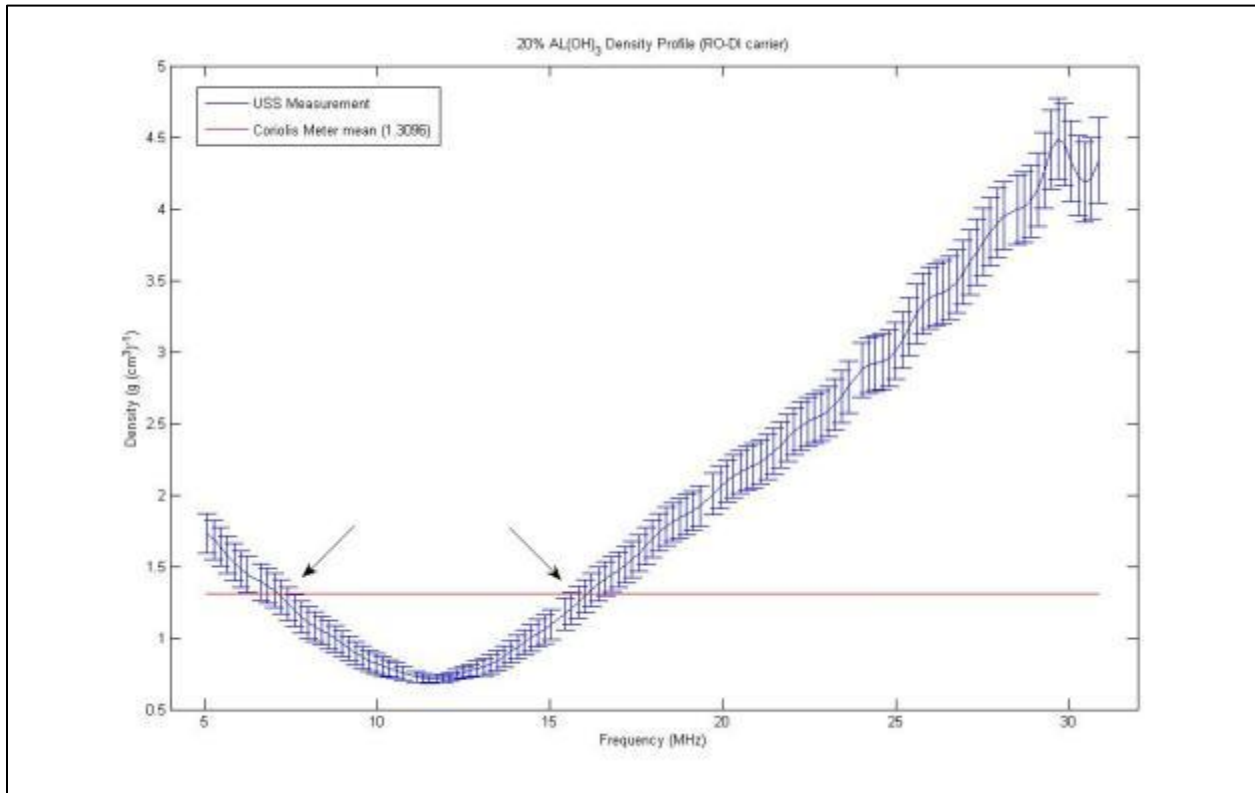
APPENDIX D

Summary spectral response spreadsheet for all trials

Suspension Description		
NaNO_3 Base Solution for Complex Mix	Freq [MHz]	
	Density [g/cc]	
	Density std dev	
2% Complex Mix + NaNO_3 Base Solution	Freq [MHz]	
	Density [g/cc]	
	Density std dev	
4% Complex Mix + NaNO_3 Base Solution	Freq [MHz]	
	Density [g/cc]	
	Density std dev	
8% Complex Mix + NaNO_3 Base Solution	Freq [MHz]	
	Density [g/cc]	
	Density std dev	
10% Complex Mix + NaNO_3 Base Solution	Freq [MHz]	
	Density [g/cc]	
	Density std dev	
RODI Base Solution	Freq [MHz]	
	Density [g/cc]	
	Density std dev	
2% Complex Mix + RODI Base Solution	Freq [MHz]	
	Density [g/cc]	
	Density std dev	
4% Complex Mix + RODI Base Solution	Freq [MHz]	
	Density [g/cc]	
	Density std dev	
8% Complex Mix + RODI Base Solution	Freq [MHz]	
	Density [g/cc]	
	Density std dev	
10% Complex Mix + RODI Base Solution	Freq [MHz]	
	Density [g/cc]	
	Density std dev	
NaNO_3 Base Solution for Base Mix	Freq [MHz]	
	Density [g/cc]	
	Density std dev	
2% Base Mix + NaNO_3 Solution	Freq [MHz]	
	Density [g/cc]	
	Density std dev	
4% Base Mix + NaNO_3 Solution	Freq [MHz]	
	Density [g/cc]	
	Density std dev	
8% Base Mix + NaNO_3 Solution	Freq [MHz]	
	Density [g/cc]	
	Density std dev	
10% Base Mix + NaNO_3 Solution	Freq [MHz]	
	Density [g/cc]	
	Density std dev	
RODI Base Solution	Freq [MHz]	
	Density [g/cc]	
	Density std dev	
2% Base Mix + RODI Base Solution	Freq [MHz]	
	Density [g/cc]	
	Density std dev	
4% Base Mix + RODI Base Solution	Freq [MHz]	
	Density [g/cc]	
	Density std dev	
8% Base Mix + RODI Base Solution	Freq [MHz]	
	Density [g/cc]	
	Density std dev	
10% Base Mix + RODI Base Solution	Freq [MHz]	
	Density [g/cc]	
	Density std dev	
NaNO_3 Base Solution for Base Mix #1	Density std dev	
NaNO_3 Base Solution for Base Mix #2	Freq [MHz]	
	Density std dev	
2% Base Mix + NaNO_3 Solution	Density std dev	
4% Base Mix + NaNO_3 Solution	Density std dev	
8% Base Mix + NaNO_3 Solution	Density std dev	
10% Base Mix + NaNO_3 Solution	Density std dev	
NaNO_3 Base Solution for Base Mix	Freq [MHz]	

ARC 2011 Year End Technical Report